Supporting Information

Carborane-thiol protected copper nanoclusters: Stimuli-responsive materials with tunable phosphorescence

Arijit Jana, Madhuri Jash, Wakeel Ahmed Dar, Jayoti Roy, Papri Chakraborty, Ganesan Paramasivam, Sergei Lebedkin, Kaplan Kirakci, Sujan Manna, Sudhadevi Antharjanam, Jan Machacek, Monika Kucerakova, Sundargopal Ghosh, Kamil Lang, Manfred M. Kappes*, Tomas Base* and Thalappil Pradeep*

Table of contents

1. Instrumentation

UV-vis spectroscopy

Solid-state absorption spectra of the NCs (as polycrystalline powders dispersed in perfluoroether oil between two quartz plates) were recorded using an Agilent Cary 5000 UV-Vis-NIR spectrophotometer equipped with a 6-inch integrating sphere. As a standard feature of such apparatus, a photodetector (photomultiplier) is placed directly into the sphere, inside a slit on its bottom. This configuration can be, however, problematic for highly luminescent samples, as is the case with the NCs studied in this work. Namely, UV photons absorbed by the NCs (white powders) are efficiently converted into the green or orange luminescence photons which would be detected by the same photomultiplier, resulting to incorrect absorbance values. In fact, even a 'negative absorbance' can be observed in the UV region, if a photomultiplier has a higher sensitivity to the green/ orange light than to the UV one. To minimize such interference of re-emitted light, the photomultiplier in the sphere was covered in our experiment with a short-pass dielectric filter (Edmund Optics) transmitting light within ca. 240-500 nm and blocking the NCs emission over ca. 510-700 nm. Accordingly, the solid-state absorption spectra were measured within a limited spectral range of 250-490 nm (Figure 4a-c). Absorption spectra in solution were recorded in standard cuvettes using a PerkinElmer Lambda 365 spectrometer in the wavelength range of 200-800 nm.

Mass spectrometry

Mass spectra of *ortho*-carborane 9-thiol, *meta*-carborane 9-thiol and *ortho*-carborane 12-iodo 9-thiol were recorded using an ion-trap Thermo Scientific LTQ XL mass spectrometer. Mass spectra of all these Cu_4 clusters were measured using Waters Synapt G2Si HDMS instrument. The instrument is equipped with electrospray ionization source, step wave ion transfer optics and a quadrupole mass filter. 1 mM formic acid and cesium acetate were used as a protonation source. Mass spectrum of the nanoclusters were recorded in positive ion-mode. An optimized condition of capillary voltage 3 kV, cone voltage 0 kV, spray current 110 nA, source temperature 50 °C and desolation temperature 90 °C with gas flow rate of 300 L/h were used for these measurements. Collision energy dependent fragmentation studies were performed upon selecting the particular ion inside the ion mobility cell of the same instrument.

Photoluminescence

Photoluminescence spectra were measured using Horiba Jobin Yvon Nanolog and Fluorolog-3 spectrometers. The latter instrument was equipped with an optical cryostat based on a closed-cycle helium cryocooler (Cryomex), operating within a temperature range of 5-300 K. Fast freezing of sample solutions and their cooling down was done by inserting a quartz tube with the probe into an optical Dewar filled with liquid nitrogen. All emission spectra were corrected for wavelength-dependent response of the spectrometer and detector (in relative photon flux units).

Lifetime and quantum yield

Luminescence lifetime measurements at ambient temperature were performed using a Fluorolog-3 spectrometer equipped with a cooled TBX-05-C photon detection module (Horiba JobinYvon). The excitation wavelength was 390 nm (SpectraLED-390, Horiba Scientific) and emission wavelength was selected at the maxima of the luminescence emission spectra. The decay curves were recorded in air atmosphere and were fitted to exponential functions by the iterative reconvolution procedure of the DAS6 software (v. 6.8, Horiba Jobin Yvon). The temperature-dependent PL decay in the cryostat was recorded by connecting a photomultiplier to a fast digital oscilloscope (via a 50, 500, 2.500 or 10.000 Ohm load depending on the decay time scale) and using a nsec-pulsed nitrogen laser for excitation at 337 nm. Absolute photoluminescence quantum yields of powder samples were measured at ambient temperature using a Quantaurus QY C11347-1 spectrometer (Hamamatsu).

Infrared spectroscopy

Perkin Elmer FT-IR spectrometer was used to measure the samples. Each pellet was prepared by mixing 2.0 mg NCs with 20 mg dry KBr.

Raman spectroscopy

Raman spectra were recorded using a CRM-Alpha 300S, WI Tec GmbH confocal Raman microscope, equipped with 532 nm frequency doubled Nd:YAG laser and 632 nm Helium Neon laser.

NMR spectroscopy

Proton decoupled ^{13}C and ^{11}B NMR spectra were recorded in its respective deuterated solvents, using a Bruker Avance 500 MHz (^{13}C-125 MHz and ^{11}B-160 MHz) spectrometer. All of the data are processed using Mest-Re Nova NMR software. NMR spectrum for Cu_4@oCBT and Cu_4@ICBT clusters were recorded using d_6-acetone solvent. All of the carborane ligands and Cu_4@mCBT NMR data were measured using $CDCl_3$ (99.99 % pure) solvent.

X-ray photoelectron spectroscopy

X-ray photoelectron spectroscopy were recorded using ESCA probe TPD equipped with polychromatic Mg Kα X ray source (hν = 1253.6 eV).

Powder XRD

Powder XRD measurements were performed using a D8 Advance, Bruker instruments using Cu Kα as a X-Ray source (hν = 8047.8 eV). Sample drop casted on a glass slide, like a thin film was used for all the PXRD measurements.

Thermogravimetric analysis

Thermogravimetric (TG) measurements of about 3.5 mg of cluster sample in an alumina crucible were performed using a NETZSCH STA 449 F3 Jupiter instruments equipped with Proteus-6.1.0 software. Both the measurements were performed under nitrogen atmosphere at flow rate of 20 ml/min in the temperature range of 30 to 700 °C with a heating rate of 10 °C/min.

Single-crystal XRD of Cu_4 clusters

Single crystal X-ray diffraction (SC-XRD) data collection of Cu_4 clusters was performed with Bruker D8 VENTURE single crystal X-ray diffractometer equipped with graphite monochromatic Mo (Kα) (λ = 0.71073 Å) radiation and PHOTON 100 CMOS detector. The data collection was performed at 296 K for Cu_4@oCBT and Cu_4@mCBT and at liquid nitrogen temperature of 200 K for the crystal of Cu_4@ICBT. The automatic cell determination routine, with 24 frames at two different orientations of the detector was employed to collect reflections for unit cell determination. Further, intensity dates for structure determination were collected through an optimized strategy which gave an average 4-fold redundancy. The program APEX3-SAINT (Bruker, 2016) was used for integrating the frames, followed by a multi-scan absorption correction using the program SADABS (Bruker, 2016). The structure was solved by SHELXT-2014 (Sheldrick, 2014) and refined by full-matrix least squares techniques using SHELXL-2018, (Sheldrick, 2018) software package. Hydrogens on all carbon and boron atoms were fixed at calculated positions and refined as riding model with C-H or B-H = 1.10 Å, Uiso(H) = 1.2Ueq (C or B).

For, Cu_4@oCBT crystal data was refined as a two component inversion twin with a BASF value of 0.188. The refinement was converged with an R1 value of 0.051. In this case an alert level B was observed in the IUCR check cif report which is primarily due to disorder in carborane moiety and also due to twinning of the crystal lattice.

In the case of Cu_4@mCBT, the higher angle reflections are very weak (θ >23.3°) due to poor resolution of the crystal which caused high Rint value of 0.18 (R1 = 0.098). Five B level alerts were observed in the IUCR check cif report which were explained through validating response form at the end of the corresponding cif file.

For Cu_4@ICBT, high resolution data is very weak and hence a resolution cut (~1.0 Å) was made during data integration. The data was refined as two component inversion twin with BASF value of 0.286. Due to very high thermal and rotational disorder of carborane moieties and also due to poor resolution data, DFIX restraint was applied to their bond distances (a target value of 1.72 Å) to maintain a sensible molecular geometry. Also SIMU restraint was applied to atoms in the carborane moieties with an effective standard deviation of 0.02 $Å^2$ to have the same Uij components. The components of the anisotropic displacement parameters in the direction of the bond are restrained to be equal for all non-hydrogen atoms using DELU restraint. The solvent

electron density could not be modelled satisfactorily due to difficulty in locating their position in this low resolution data and hence squeezed using PLATON (version 10719) and the squeeze results are appended in the corresponding cif file. Several attempts were made to collect SC-XRD data at room temperature as well as at low temperatures. This is the best data we could obtain after repeated attempts. Although, it is a low resolution data, the structure is presented here to describe its formation with the support of other experimental findings. A cif check report was made using the service of IUCR in which A and B level alerts were explained at the end of the corresponding cif file as validation response form.

SC-XRD of I_9 ligand

Crystals suitable for single crystal X-ray diffraction were obtained by slow sublimation of I_9 in a sealed ampoule over a few weeks. Single crystal was measured at 95 K on a Supernova four-circles diffractometer equipped with a CCD Atlas S2 detector, using the mirrors-collimated Cu-Kα radiation (λ = 1.54184 Å) from a micro-focus tube and a Cryostream 800 + chiller. The CrysAlis program suite was used for the unit cell determination and data reduction.[1] The crystal structure was solved by charge-flipping using program SUPERFLIP[2] and refined by full-matrix least-squares on F2 using the Jana2020 program package, not yet published successor of Jana2006.[3]

Hydrogen atoms bonded to C and B atoms were discernible in difference Fourier maps and were kept in ideal positions with C–H distance = 0.96 Å and B–H distance = 1 Å. For all hydrogen atoms, Uiso(H) was set to 1.2Ueq(C/B) of the parent atom. Precise position of the hydrogen atom attached to sulfur in the structure of I_9 was not observed in the difference Fourier map, probably due to multiple possible positions. All non-hydrogen atoms were refined using harmonic refinement. The structure shows two independent molecules per unit cell with a disorder manifested by mixed sulfur and iodine occupancies. Mixed site S/I occupancies 0.768:0.232 for one molecule and 0.933:0.067 for the other molecules per unit cell solved the problems of some atoms showing negative thermal parameters.

In the structure, the residual electron density occurs close to the atoms B_5 and B_{11}. These maxima probably correspond to an iodine atom with an occupation of 0.02 and point to possible additional disorder of both molecules. However, boron or carbon atoms with 2% occupation is not possible to observe in the electron density map. Apparently, reliable description of the disorder in is far beyond resolution of our data, although there is no doubt it exists. For these reasons, we did not introduce disorder to the final structure model.

Optical imaging

Optical microscopic images of the crystal were collected in different magnification using LEICA optical microscope equipped with LAS V4.8 software.

SEM imaging

The SEM measurements were performed using FEI quanta environmental scanning electron microscope (ESEM) at high vacuum mode at operating voltage 30 kV. EDAX spectra and elemental imaging were recorded using the same instruments.

TEM imaging

Dimension of the nanoclusters were recorded using Transmission electron microscopy, which was recorded using a JEOL 3010 high resolution transmission electron microscope operated at 200 kV. A Gatan multistage CCD camera was used to record the image.

2. Computational calculations

The structural, electronic and optical absorption properties of the Cu_4 nanoclusters protected with a monolayer of *ortho*-carborane 9-thiol (O_9), *meta*-carborane 9-thiol (M_9) and *ortho*-carborane 12-iodo 9-thiol (I_9) ligands were computationally studied using density functional theory (DFT) as implemented in grid spaced projector augmented wave (GPAW) software package.[4,5] The effective valence electrons of all the atoms in the considered cluster are described by the PAW set-ups such as Cu ($3d^{10}$ $4s^1$), S ($3s^2 3p^4$), C ($2s^2 2p^2$), B ($2s^2 2p^1$) and H ($1s^1$). For geometry optimizations, the cluster boundary condition was set by taking the structure in a cubic box and a grid spacing of 0.2 Å was considered for the greater accuracy of real space for electron density inside the cubic box. Further, the convergence criterion to minimize the forces between the atoms in the cluster was to be 0.05 eV/Å, without imposing any symmetry constraints. The PBE (Perdew-Burke-Ernzerhof) exchange-correlation functional was utilized in the calculations as it describes the metal interactions in the cluster.[6,7] The atomic coordinates taken from the crystal structure of Cu_4 cluster were used as a starting point for the geometry optimization. The optimized Cu_4 structures were utilized to calculate the absorption spectra using Gaussion09. Further, the Cu_4 structures were once optimized to investigate the geometrical changes in gas and solvent phases. Solvent effects were modelled by the Polarisable Continuum Model (PCM) with solvent excluding surface, using parameters of dichloromethane for Cu_4@mCBT, and acetone for Cu_4@oCBT and Cu_4@ICBT.[8-10] The IR spectra were calculated for the optimized structures in gas phases from their frequency calculations. All the structures were visualized using visual molecular dynamics (VMD) software.

The excited state emission characteristics were studied using the Gaussian 16 quantum chemistry package[11] within the frame of the Density Functional Theory (DFT) and the Time Dependent DFT (TD-DFT). The hybrid exchange–correlation functional PBE0 by Adamo[12] was used (PBE1PBE in the notation of the Gaussian input) and Los Alamos National Laboratory double-zeta basis LANL2DZ with scalar-relativistic effective core potentials on heavier elements (sulphur and iodine).[13]

Table S1. Crystal data and structure refinement for I_9 ligand

Identification code	I_9 ligand	
Empirical formula	$C_2 B_{10} H_{10} I S$	
Formula weight	301.16	
Temperature	95 K	
Wavelength	1.54184 Å	
Crystal system	monoclinic	
Space group	P 21/n	
Unit cell dimensions	a = 14.1490 (6) Å	α = 90°
	b = 7.7293 (3) Å	β = 91.659°
	c = 20.6546 (9) Å	γ = 90°
Volume	2257.88 (16) $Å^3$	
Z	4	
Density (calculated)	1.772 gm/cm^3	
Absorption coefficient	23.481 mm^{-1}	
F(000)	1128	
Crystal size	0.072 x 0.032 x 0.02 mm^3	
Theta range for data collection	2.13 to 37.14°.	
Index ranges	-16<=h<=17, -9<=k<=8, -20<=l<=25	
Reflections collected	13000	
Independent reflections	4635 [R(reflection) = 0.0388]	
Completeness to theta = 37.31°	97.9 %	
Absorption correction	Empirical Gaussian integration	
Max. and min. transmission	0.625 and 0.467	
Refinement method	Full-matrix least-squares on F^2	
Data / restraints / parameters	4538 / 0 / 259	
Goodness-of-fit on F^2	1.569	
Final R indices [I>2sigma(I)]	R1 = 0.0388, wR2 = 0.0453	
R indices (all data)	R1 = 0.0564, wR2 = 0.0485	
Absolute structure parameter	0.16 (4)	
Extinction coefficient	n/a	

Table S2. Crystal data and structure refinement for [Cu_4@oCBT].

Identification code	Cu_4@oCBT	
Empirical formula	$C_8H_{44}B_{40}Cu_4S_4$	
Formula weight	955.23	
Temperature	296(2) K	
Wavelength	0.71073 Å	
Crystal system	Trigonal	
Space group	$P3_121$	
Unit cell dimensions	a = 11.4344(6) Å	α = 90°
	b = 11.4344(6) Å	β = 90°
	c = 29.4398(16) Å	γ = 120°
Volume	3333.4(4) $Å^3$	
Z	3	
Density (calculated)	1.428 Mg/m^3	
Absorption coefficient	2.091 mm^{-1}	
F(000)	1416	
Crystal size	0.200 x 0.150 x 0.150 mm^3	
Theta range for data collection	2.922 to 26.057°.	
Index ranges	-14<=h<=13, -14<=k<=14, -36<=l<=36	
Reflections collected	64165	
Independent reflections	4384 [R(int) = 0.0563]	
Completeness to theta = 25.242°	99.6 %	
Absorption correction	Semi-empirical from equivalents	
Max. and min. transmission	0.7453 and 0.6112	
Refinement method	Full-matrix least-squares on F^2	
Data / restraints / parameters	4384 / 0 / 255	
Goodness-of-fit on F^2	1.121	
Final R indices [I>2sigma(I)]	R1 = 0.0513, wR2 = 0.1266	
R indices (all data)	R1 = 0.0570, wR2 = 0.1305	
Absolute structure parameter	0.19(4)	
Extinction coefficient	n/a	
Largest diff. peak and hole	1.205 and -0.613 e.$Å^{-3}$	

Table S3. Atomic coordinates (x 10^4) and equivalent isotropic displacement parameters ($Å^2$x 10^3) for Cu_4@oCBT. U(eq) is defined as one third of the trace of the orthogonalized U^{ij} tensor.

	x	y	z	U(eq)
Cu(1)	0	5122(1)	6667	52(1)
Cu(2)	-61(1)	3393(1)	6038(1)	48(1)
Cu(3)	0	1672(1)	6667	49(1)
C(1)	5803(10)	4668(11)	6190(4)	80(3)
B(10)	5052(13)	3112(16)	5973(6)	89(4)
C(3)	1629(11)	8624(10)	5026(3)	73(3)
C(4)	876(14)	8774(13)	5462(4)	90(4)
B(1)	2607(9)	3069(9)	6067(3)	40(2)
B(2)	3475(10)	4706(10)	6300(3)	50(2)
B(3)	3353(11)	3349(12)	6610(3)	57(2)
B(4)	3485(11)	2215(11)	6228(4)	60(3)
B(5)	3661(12)	2883(12)	5667(4)	62(3)
B(6)	3662(11)	4444(12)	5715(3)	58(3)
B(7)	5193(13)	4455(16)	5670(5)	84(4)
B(8)	5082(12)	5572(12)	6048(5)	68(3)
B(9)	4887(12)	4888(13)	6585(5)	72(3)
C(2)	4867(12)	3354(13)	6528(5)	92(4)
B(11)	-65(10)	6043(10)	5665(3)	46(2)
B(12)	-576(13)	7240(13)	5558(5)	75(4)
B(13)	-643(13)	6166(14)	5115(4)	72(3)
B(14)	779(13)	5943(12)	5176(4)	62(3)
B(15)	1746(11)	6913(10)	5646(3)	53(2)
B(16)	899(12)	7710(11)	5891(4)	62(3)
B(17)	2310(13)	8637(13)	5534(4)	72(3)
B(18)	2160(13)	7535(12)	5102(3)	65(3)
B(19)	803(15)	7101(15)	4774(4)	80(4)
B(20)	-58(16)	7853(15)	5001(5)	87(4)
S(1)	-1112(2)	4535(2)	6036(1)	52(1)
S(2)	725(2)	2030(2)	5972(1)	49(1)

Table S4. Crystal data and structure refinement for [Cu_4@mCBT].

Identification code	Cu_4@mCBT	
Empirical formula	$C_8H_{44}B_{40}Cu_4S_4$	
Formula weight	955.23	
Temperature	296(2) K	
Wavelength	0.71073 Å	
Crystal system	Monoclinic	
Space group	$P2_1/c$	
Unit cell dimensions	a = 11.3989(7) Å	α = 90°
	b = 11.9482(7) Å	β = 91.213(2)°
	c = 32.3144(19) Å	γ = 90°
Volume	4400.1(5) $Å^3$	
Z	4	
Density (calculated)	1.442 Mg/m^3	
Absorption coefficient	2.112 mm^{-1}	
F(000)	1888	
Crystal size	0.200 x 0.200 x 0.150 mm^3	
Theta range for data collection	3.044 to 23.439°.	
Index ranges	-12<=h<=12, -13<=k<=13, -36<=l<=36	
Reflections collected	54022	
Independent reflections	6415 [R(int) = 0.1819]	
Completeness to theta = 23.439°	99.2 %	
Absorption correction	Semi-empirical from equivalents	
Max. and min. transmission	0.7456 and 0.5645	
Refinement method	Full-matrix least-squares on F^2	
Data / restraints / parameters	6415 / 298 / 505	
Goodness-of-fit on F^2	1.116	
Final R indices [I>2sigma(I)]	R1 = 0.0986, wR2 = 0.1819	
R indices (all data)	R1 = 0.1808, wR2 = 0.2141	
Extinction coefficient	n/a	
Largest diff. peak and hole	0.484 and -0.429 $e.Å^{-3}$	

Table S5. Atomic coordinates (x 10^4) and equivalent isotropic displacement parameters ($Å^2$x 10^3) for Cu_4@mCBT. U(eq) is defined as one third of the trace of the orthogonalized U^{ij} tensor.

	x	y	z	U(eq)
Cu(1)	7455(2)	5278(1)	6964(1)	92(1)
Cu(2)	5347(1)	4301(1)	6816(1)	75(1)
Cu(3)	6138(2)	3468(1)	6103(1)	75(1)
Cu(4)	8236(1)	4472(1)	6211(1)	76(1)
B(7)	8429(14)	850(14)	7774(6)	82(4)
C(2)	8369(14)	1984(13)	8096(5)	102(4)
B(14)	6656(18)	9473(15)	5913(7)	110(5)
C(4)	6700(18)	8215(14)	5648(6)	130(5)
C(6)	7110(30)	2216(19)	4596(7)	183(8)
B(21)	7530(20)	3420(20)	4342(7)	152(7)
C(7)	2472(18)	1206(16)	6679(6)	137(6)
B(35)	1466(16)	902(16)	6330(7)	103(5)
B(1)	7058(15)	2683(15)	8023(5)	84(4)
B(2)	8360(13)	3199(14)	7808(5)	75(3)
B(3)	9108(13)	2043(12)	7662(6)	75(4)
B(4)	7148(14)	869(14)	7476(5)	76(3)
B(5)	7154(15)	1258(14)	7976(6)	82(4)
B(6)	8383(14)	2796(13)	7290(5)	73(3)
C(1)	8424(13)	1325(11)	7271(5)	87(3)
B(8)	6300(15)	1960(13)	7631(5)	79(3)
B(9)	7035(13)	3213(12)	7511(5)	64(3)
B(10)	7093(14)	2048(13)	7173(5)	72(3)
B(11)	6674(15)	7103(14)	5992(6)	96(4)
B(12)	8000(19)	7507(17)	5788(7)	115(5)
B(13)	7960(20)	8964(19)	5743(9)	145(6)
B(17)	6610(20)	9113(18)	6421(7)	127(5)
B(15)	5908(16)	8331(14)	6061(7)	101(5)
B(16)	8743(17)	8365(16)	6155(9)	133(6)
C(3)	7846(17)	9476(13)	6219(7)	144(6)
B(18)	6582(15)	7679(17)	6472(7)	102(4)
B(19)	7913(12)	7203(12)	6306(6)	74(3)

B(20)	7860(20)	8449(16)	6585(8)	123(5)
C(5)	8639(18)	3890(30)	4622(7)	188(8)
B(22)	8978(18)	3120(30)	5049(7)	167(8)
B(23)	8000(20)	2020(20)	5034(6)	141(6)
B(24)	6380(20)	3341(19)	4636(6)	115(5)
B(25)	8540(30)	2480(40)	4588(8)	214(10)
B(26)	8100(20)	4340(20)	5117(7)	133(6)
B(27)	7238(17)	4371(18)	4682(5)	97(4)
B(28)	6609(19)	2493(18)	5073(7)	113(5)
B(29)	7784(13)	3082(12)	5372(5)	63(3)
B(30)	6684(16)	3900(16)	5109(5)	91(4)
B(31)	2390(18)	2643(16)	5868(6)	106(5)
B(32)	3506(18)	1738(16)	5958(7)	112(5)
B(33)	2923(18)	647(15)	6233(9)	131(6)
C(8)	2005(18)	1287(15)	5865(6)	130(5)
B(34)	1203(17)	2132(17)	6120(10)	130(6)
B(36)	1929(15)	3192(16)	6299(8)	120(5)
B(37)	3749(17)	1685(17)	6485(8)	126(6)
B(38)	3415(12)	2972(12)	6263(5)	61(3)
B(39)	2750(20)	2580(20)	6709(6)	132(6)
B(40)	1330(20)	2090(20)	6574(10)	154(7)
S(1)	6254(4)	4557(3)	7402(1)	87(1)
S(2)	4434(3)	4195(3)	6223(1)	76(1)
S(3)	7865(3)	2849(3)	5941(1)	70(1)
S(4)	8729(3)	5962(3)	6549(2)	98(1)

Table S6. Crystal data and structure refinement for [Cu_4@ICBT].

Identification code	Cu_4@ICBT	
Empirical formula	$C_8H_{41}B_{40}Cu_4I_3S_4$	
Formula weight	1332.91	
Temperature	200(2) K	
Wavelength	0.71073 Å	
Crystal system	Tetragonal	
Space group	$P4_32_12$	
Unit cell dimensions	a = 12.716(3) Å	α = 90.00(3)°
	b = 12.716(3) Å	β = 90.00(3)°
	c = 39.812(8) Å	γ = 90.00(3)°
Volume	6438(3) $Å^3$	
Z	4	
Density (calculated)	1.375 Mg/m^3	
Absorption coefficient	2.884 mm^{-1}	
F(000)	2512	
Crystal size	0.200 x 0.150 x 0.120 mm^3	
Theta range for data collection	3.018 to 19.992°.	
Index ranges	-12<=h<=12, -12<=k<=12, -38<=l<=38	
Reflections collected	33001	
Independent reflections	2991 [R(int) = 0.0566]	
Completeness to theta = 19.992°	99.3 %	
Absorption correction	Semi-empirical from equivalents	
Max. and min. transmission	0.5610 and 0.3783	
Refinement method	Full-matrix least-squares on F^2	
Data / restraints / parameters	2991 / 578 / 273	
Goodness-of-fit on F^2	1.082	
Final R indices [I>2sigma(I)]	R1 = 0.1061, wR2 = 0.2772	
R indices (all data)	R1 = 0.1123, wR2 = 0.2841	
Absolute structure parameter	0.29(16)	
Extinction coefficient	n/a	
Largest diff. peak and hole	1.252 and -0.727 e.$Å^{-3}$	

Table S7. Atomic coordinates (x 10^4) and equivalent isotropic displacement parameters ($Å^2$x 10^3) for Cu_4@ICBT. U(eq) is defined as one third of the trace of the orthogonalized U^{ij} tensor.

	x	y	z	U(eq)
Cu(1)	1638(4)	8362(4)	7500	114(3)
Cu(2)	1800(5)	6377(4)	7173(1)	111(2)
Cu(3)	3742(4)	6258(4)	7500	106(2)
I(1)	3120(2)	8882(2)	6837(1)	101(1)
I(2)	849(6)	4473(5)	7562(2)	141(3)
S(1)	515(9)	7496(11)	7194(2)	115(3)
S(2)	3225(10)	5565(9)	7028(2)	108(3)
B(1)	-590(20)	8660(30)	6617(7)	120(6)
B(2)	480(20)	9460(30)	6707(7)	121(6)
C(1)	-630(20)	8470(20)	6193(6)	124(6)
C(2)	390(20)	9130(20)	6030(7)	125(6)
B(3)	1530(20)	8580(30)	6153(7)	115(6)
B(4)	1160(20)	7570(20)	6420(6)	111(6)
B(5)	-160(20)	7490(30)	6442(7)	118(6)
B(6)	460(20)	7780(20)	6062(7)	119(6)
B(7)	-270(20)	9680(20)	6354(7)	125(6)
B(8)	1100(20)	9760(20)	6329(7)	122(6)
B(9)	1550(20)	8760(30)	6576(7)	115(6)
B(10)	520(20)	8100(30)	6763(6)	114(6)
B(13)	3170(30)	4120(20)	7168(9)	158(7)
B(14)	3370(40)	3670(30)	7569(9)	163(7)
B(11)	2340(30)	3240(30)	6965(9)	165(7)
B(12)	3670(30)	3180(30)	6895(9)	170(8)
C(3)	4170(30)	2180(30)	7134(9)	177(8)
C(4)	3160(30)	1630(20)	7351(9)	177(8)
B(15)	2010(30)	2250(30)	7252(10)	171(8)
B(16)	2950(40)	2040(30)	6947(9)	174(8)
B(17)	4320(30)	3450(30)	7267(10)	169(8)
B(18)	3990(30)	2470(30)	7553(9)	174(8)
B(19)	2660(30)	2530(30)	7623(9)	173(8)
B(20)	2150(30)	3540(30)	7386(9)	165(7)

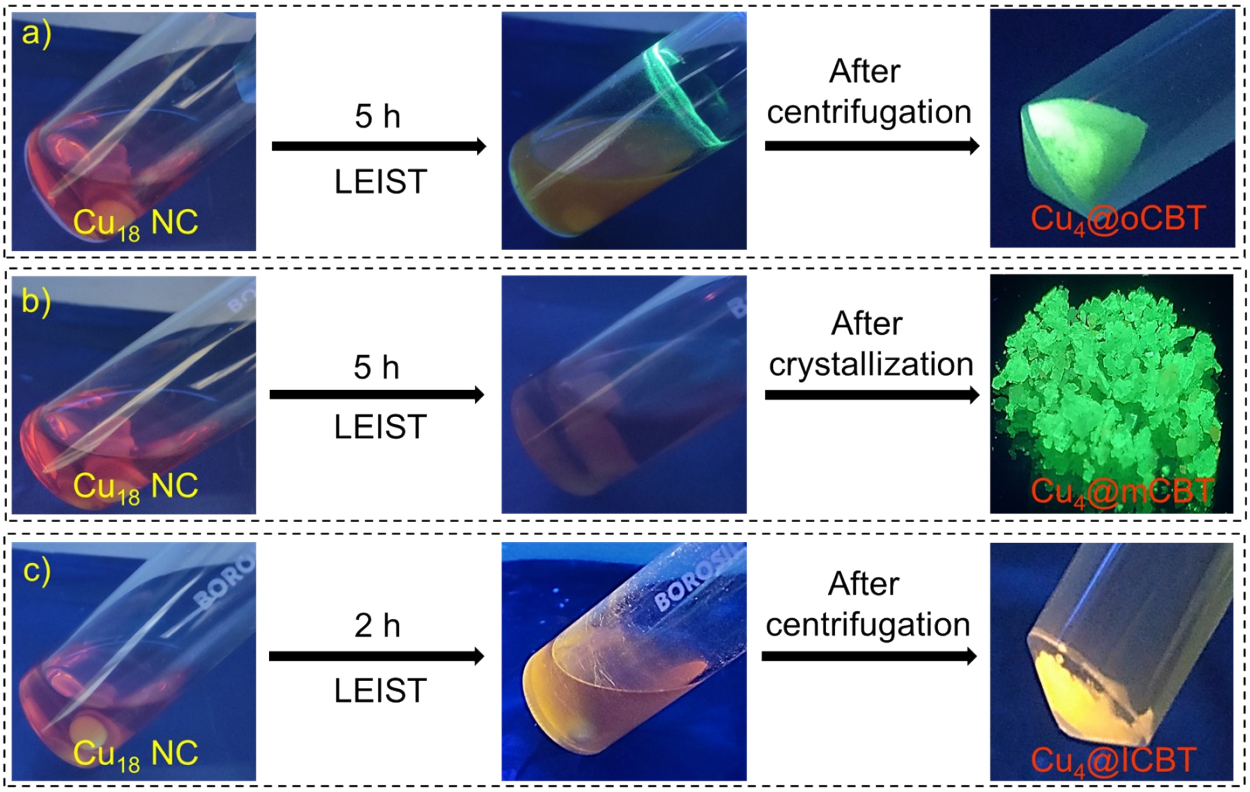

Fig. S1 Photographic images of the different steps of synthesis and purification of a) Cu_4@oCBT, b) Cu_4@mCBT and c) Cu_4@ICBT, starting from Cu_{18}. All of the images were taken under 365 nm UV light.

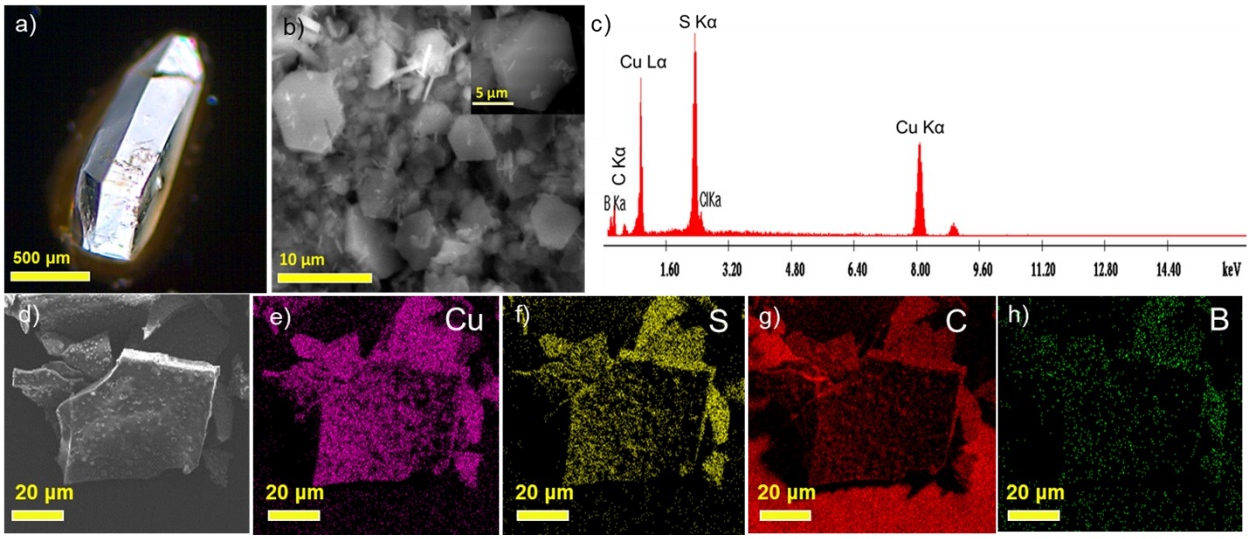

Fig. S2 a) Optical microscopic image of Cu_4@oCBT single crystals, b) Large area SEM images of crystals (inset shows magnified image of a single crystal), c) The EDS spectrum of the Cu_4@oCBT crystals, d-h) the elemental mapping of respective elements present in crystal.

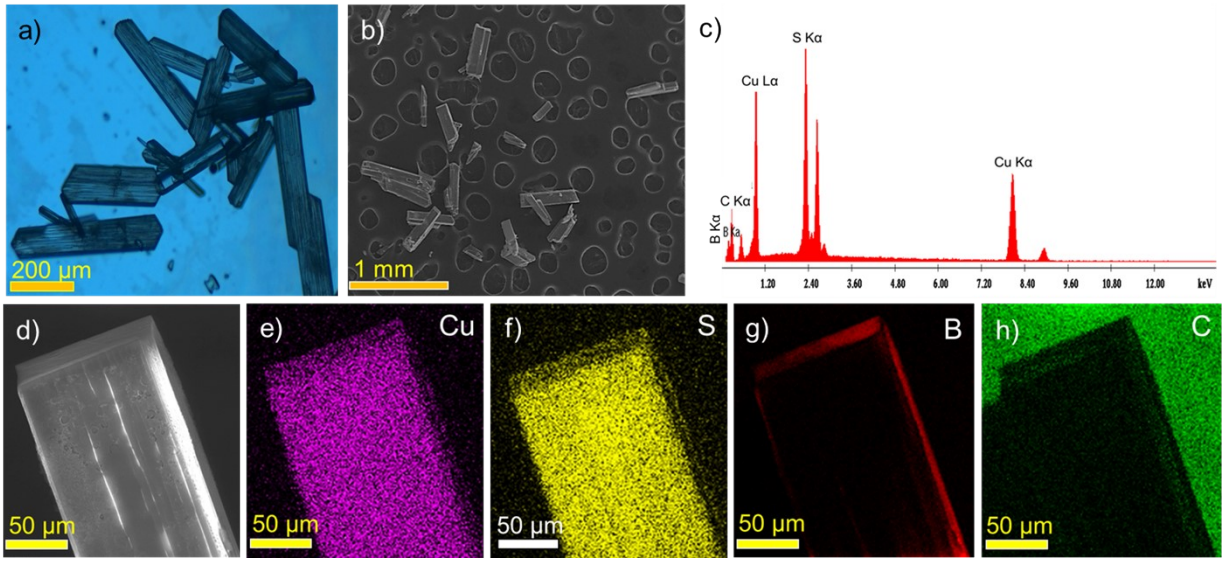

Fig. S3 a) Optical microscopic image of cuboid crystals of Cu_4@mCBT. b) Large area SEM image of same crystals. c) The EDS spectrum of the crystals have respective elements. d-h) Elemental mapping of the crystal with corresponding elements.

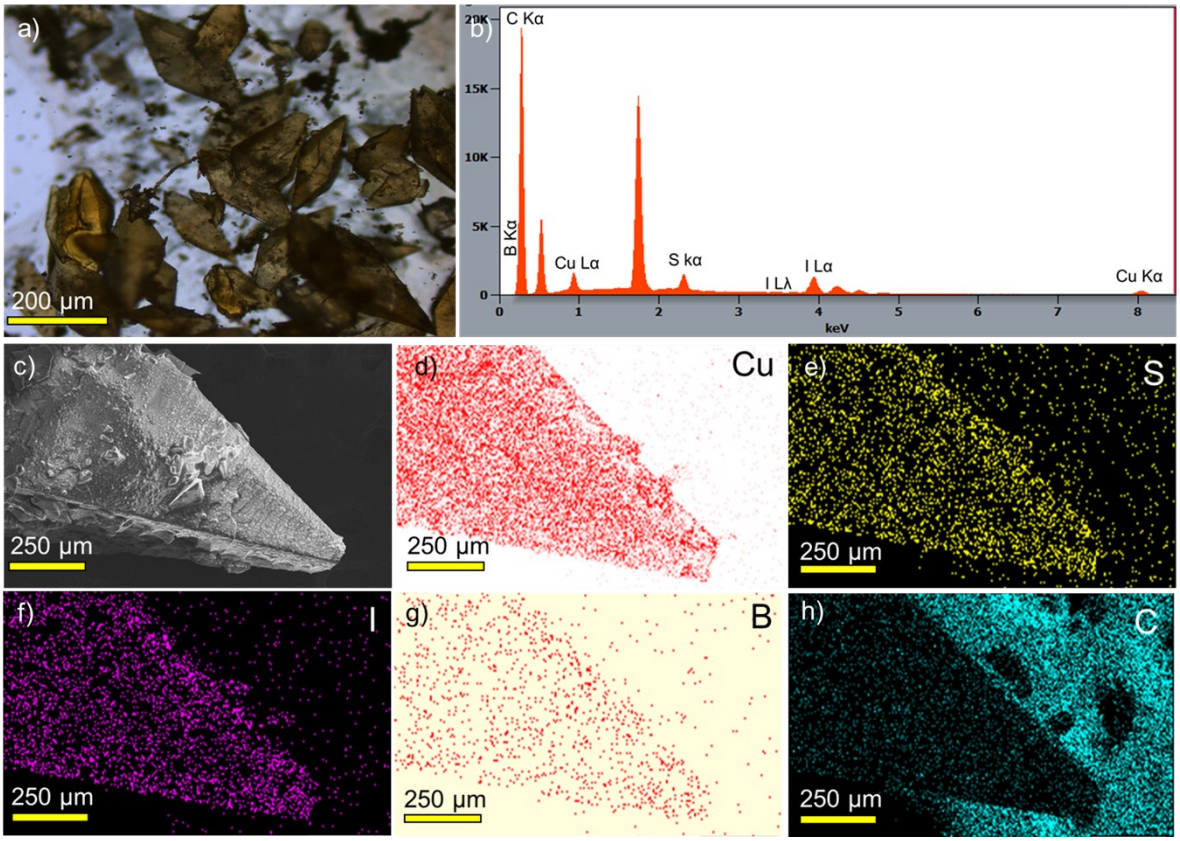

Fig. S4 a) Optical microscopic image of rhombus crystals of Cu_4@ICBT. b) Large area SEM images for the same crystals. c) The EDS spectrum for the Cu_4@mCBT crystal. d-h) Elemental mapping of the crystal with corresponding its assigned elements.

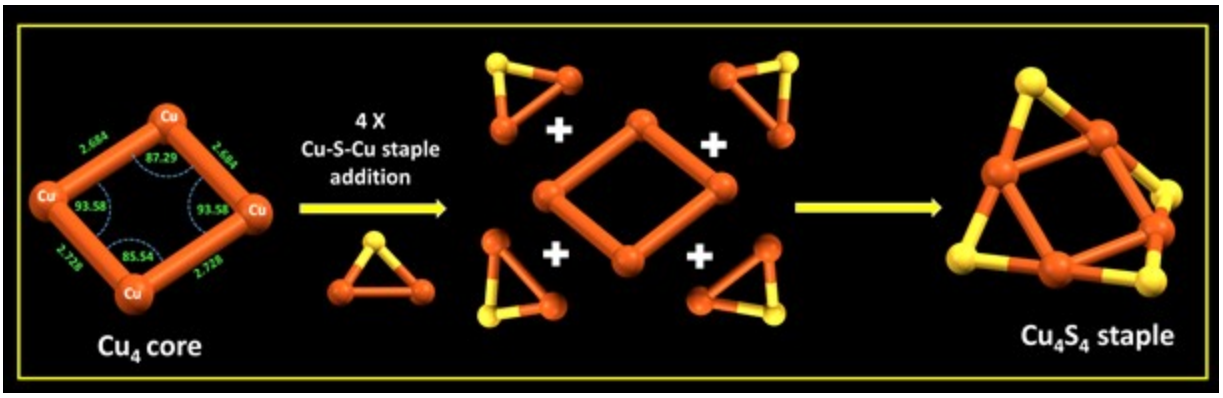

Fig. S5 Structural anatomy of Cu_4S_4 kernel having a square planner Cu_4 with four 'V-shaped' Cu-S-Cu motifs.

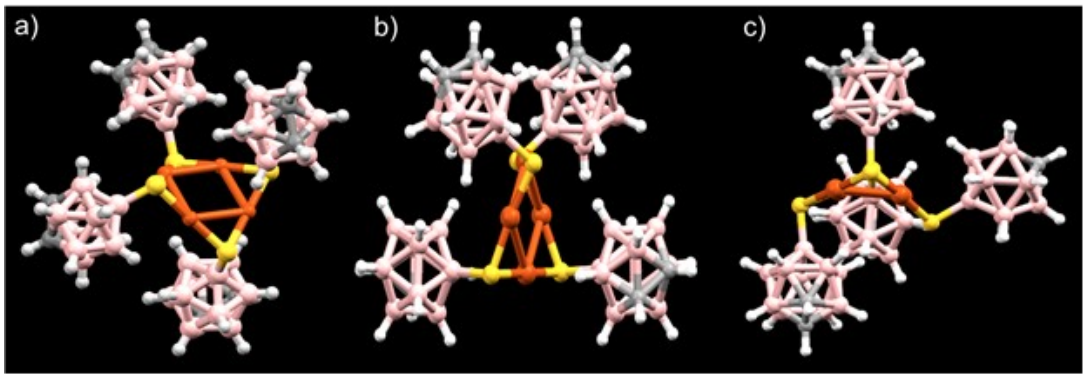

Fig. S6 a-c) Structures of Cu_4@oCBT in three different orientations showed anti orientation of *ortho*-carborane ligands present in the opposite corner of the cluster.

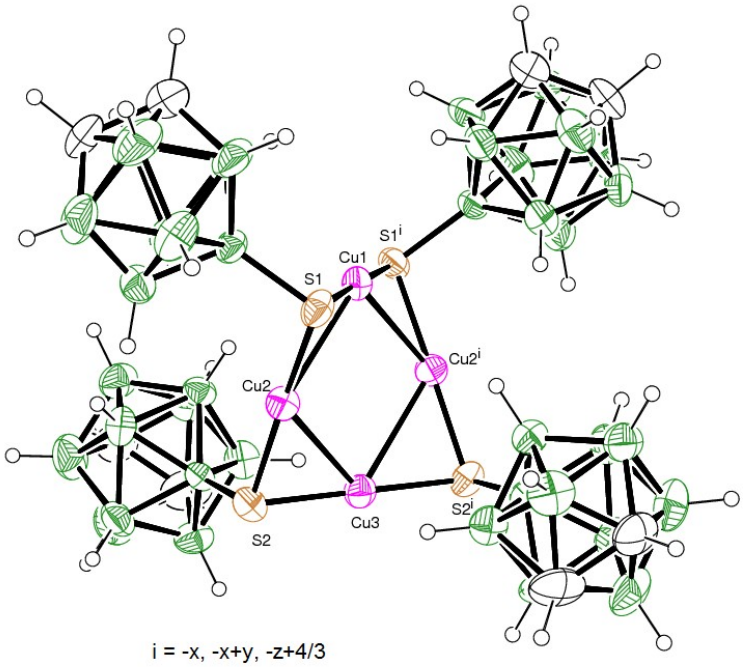

Fig. S7 ORTEP structure of Cu_4@oCBT having 50% thermal ellipsoid probability.

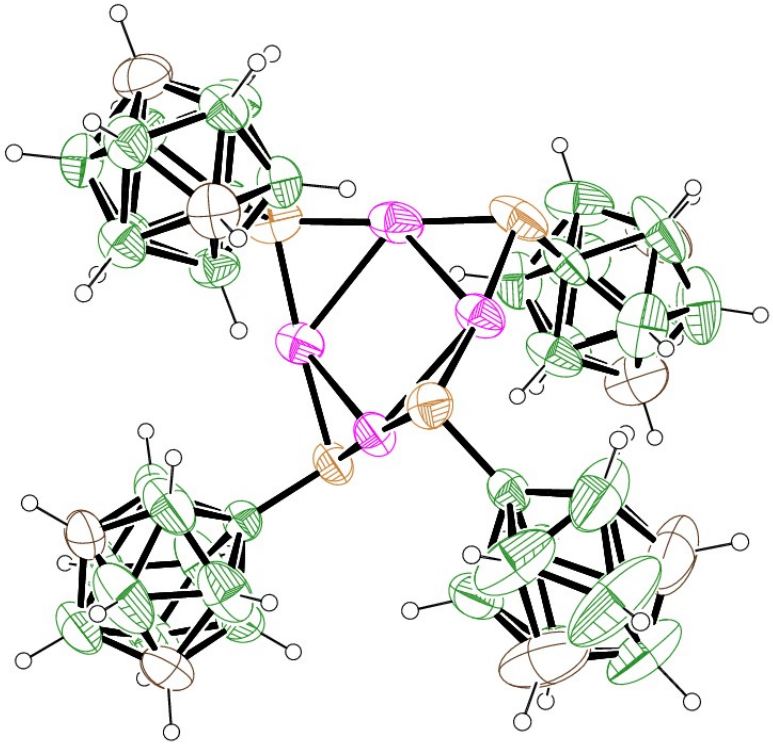

Fig. S8 ORTEP structure of Cu_4@mCBT having 50% thermal ellipsoid probability.

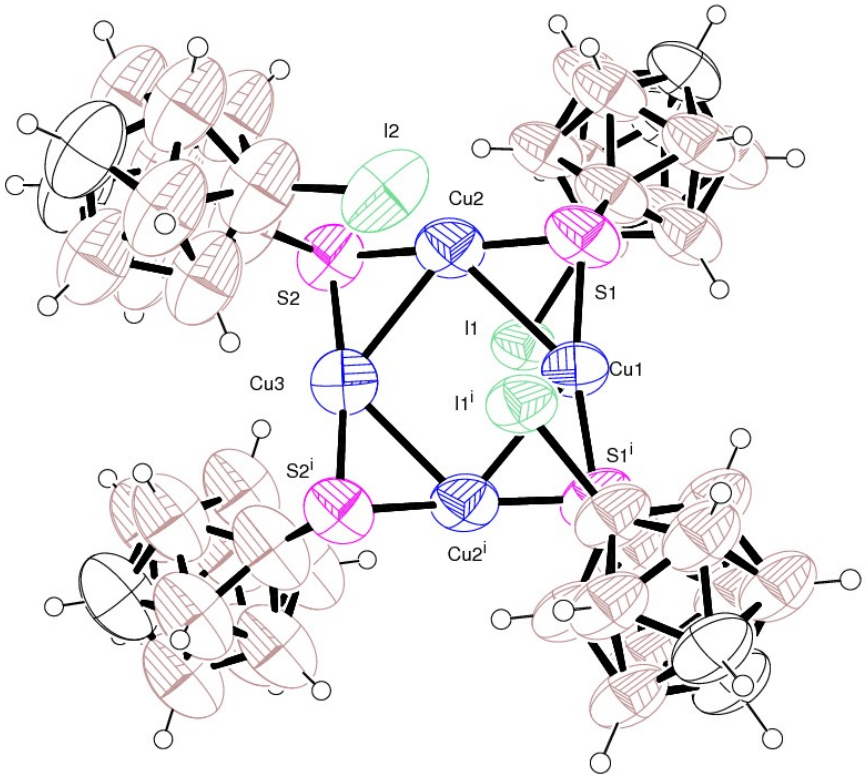

Fig. S9 ORTEP image of Cu_4@ICBT having 50 % thermal ellipsoid probability.

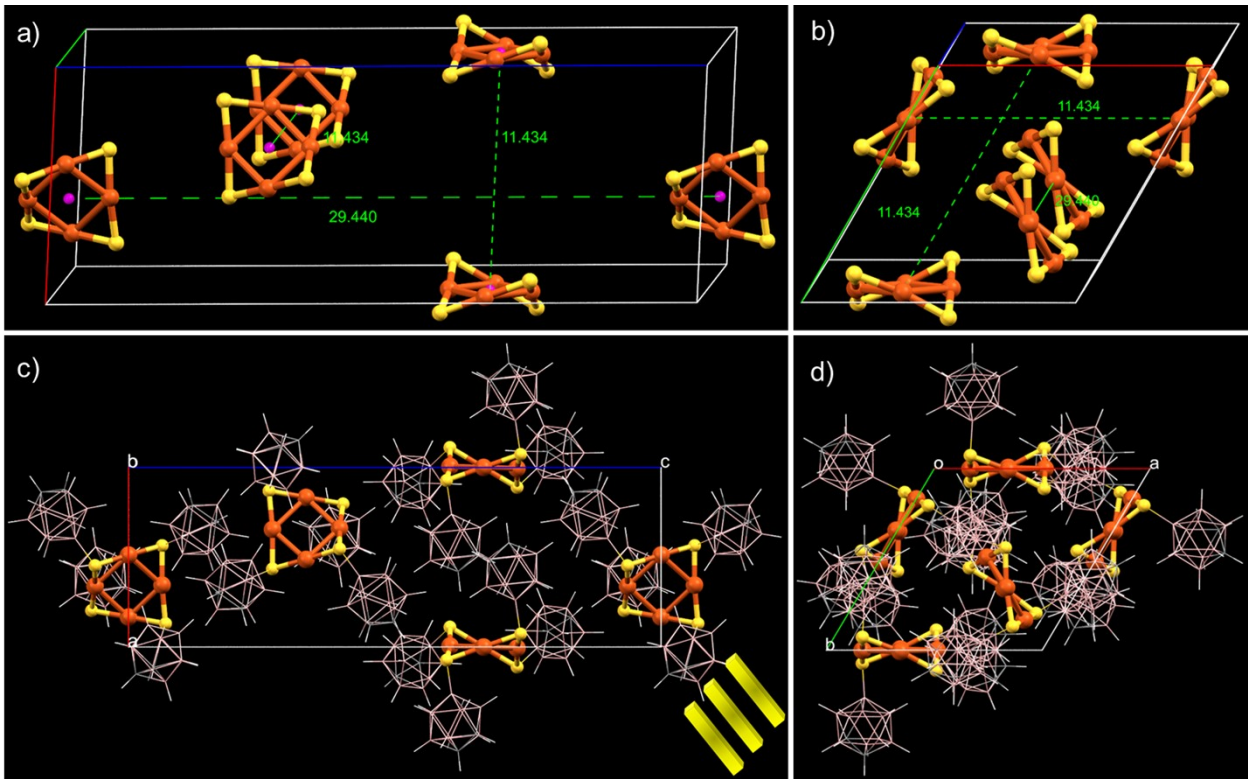

Fig. S10 Unit cell packing of Cu_4S_4 unit of Cu_4@oCBT viewed from a) b and b) c crystallographic axis. The distances between opposite Cu_4S_4 centroids are marked here. Unit cell molecular packing along c) b and d) c crystallographic axis.

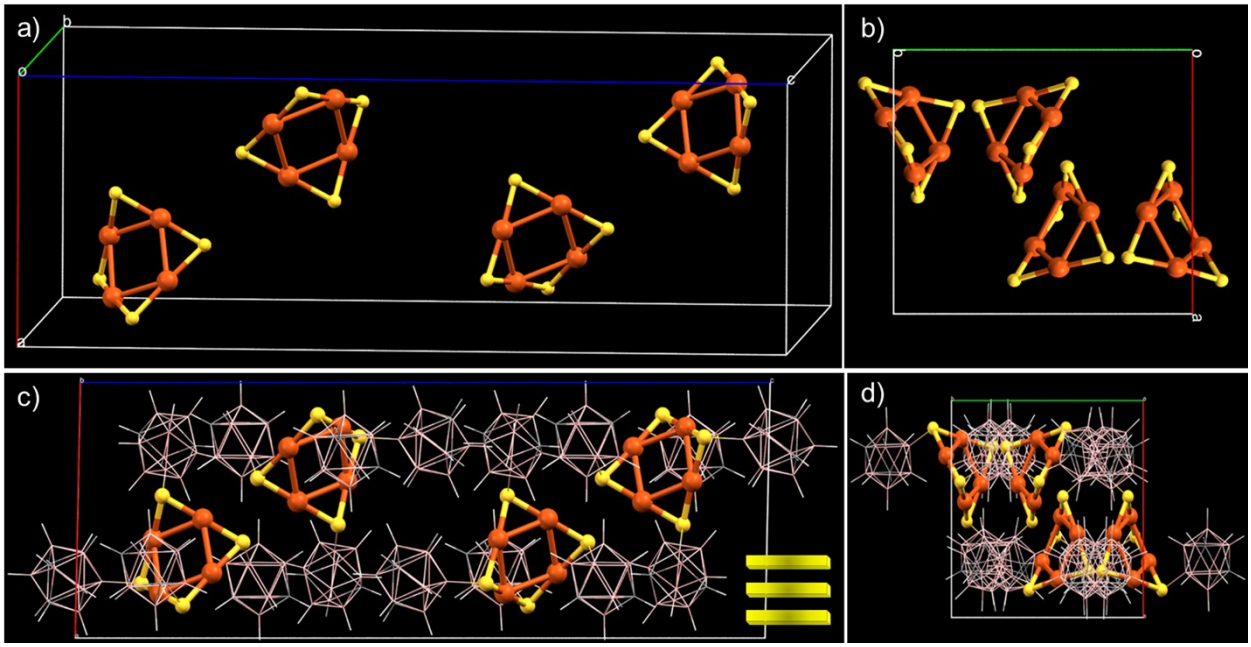

Fig. S11 Unit cell packing of Cu_4S_4 unit of Cu_4@mCBT viewed from a) b and b) c crystallographic axis. Unit cell molecular packing viewed from c) b and d) c crystallographic axis.

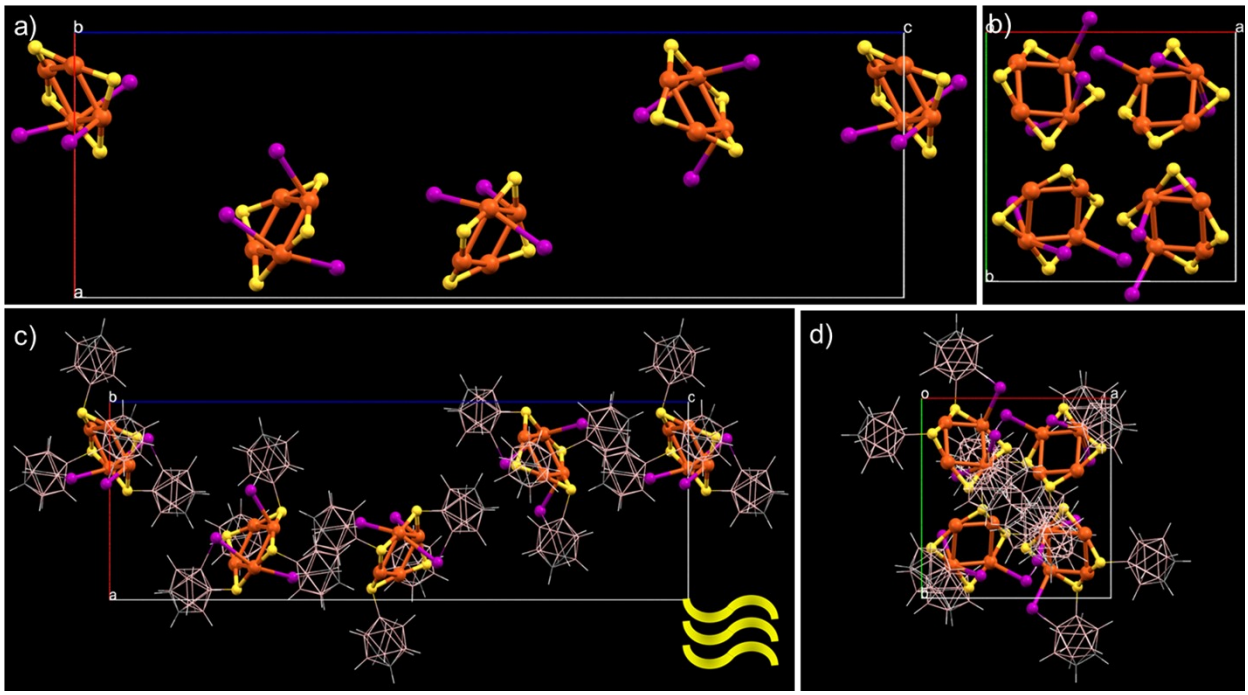

Fig. S12 Unit cell packing of Cu_4S_4 unit of Cu_4@ICBT viewed from a) b and b) c crystallographic axis. Unit cell molecular packing viewed from c) b and d) c crystallographic axis.

Table S8. Comparative interatomic bond distances and bond angles of the respective Cu_4 clusters.

Sl. No	Contents	Cu_4@oCBT	Cu_4@mCBT	Cu_4@ICBT
1.	Cu-Cu bond distance	2.68 Å, 2.68 Å, 2.73 Å, 2.73 Å	2.68 Å , 2.71 Å, 2.78 Å, 2.70 Å	2.85 Å, 2.85 Å, 2.80 Å, 2.80 Å
2.	Cu-Cu-Cu bond angle	87.29°, 93.58°, 93.58°, 85.54°	89.75°, 89.91°, 88.17°, 92.11°	84.18°, 94.66°, 96.99°, 84.18°
3.	Cu-S-Cu bond angle	76.58°, 76.58°, 78.13°, 78.13°	76.48°, 76.62°, 80.20°, 77.29°	80.22°, 80.22°, 81.93°, 81.93°
4.	Opposite S-S distance	5.54 Å, 5.54 Å	5.42 Å, 5.49 Å	5.94 Å, 5.94 Å
5.	CB B-S distance	1.88 Å, 1.88 Å, 1.89 Å, 1.89 Å	1.86 Å, 1.91 Å, 1.87 Å, 1.87 Å	1.88 Å, 1.88 Å, 1.92 Å, 1.92 Å
6.	CB-CB centroid distance	7.37 Å, 8.22 Å, 7.37 Å, 9.23 Å	7.54 Å, 7.91 Å , 7.46 Å, 9.24 Å	9.37 Å, 9.06 Å, 7.56 Å, 9.06 Å
7.	Opposite CB-CB centroid distance	9.73 Å , 9.73 Å	9.3 Å , 9.64 Å	10.59 Å, 10.59 Å

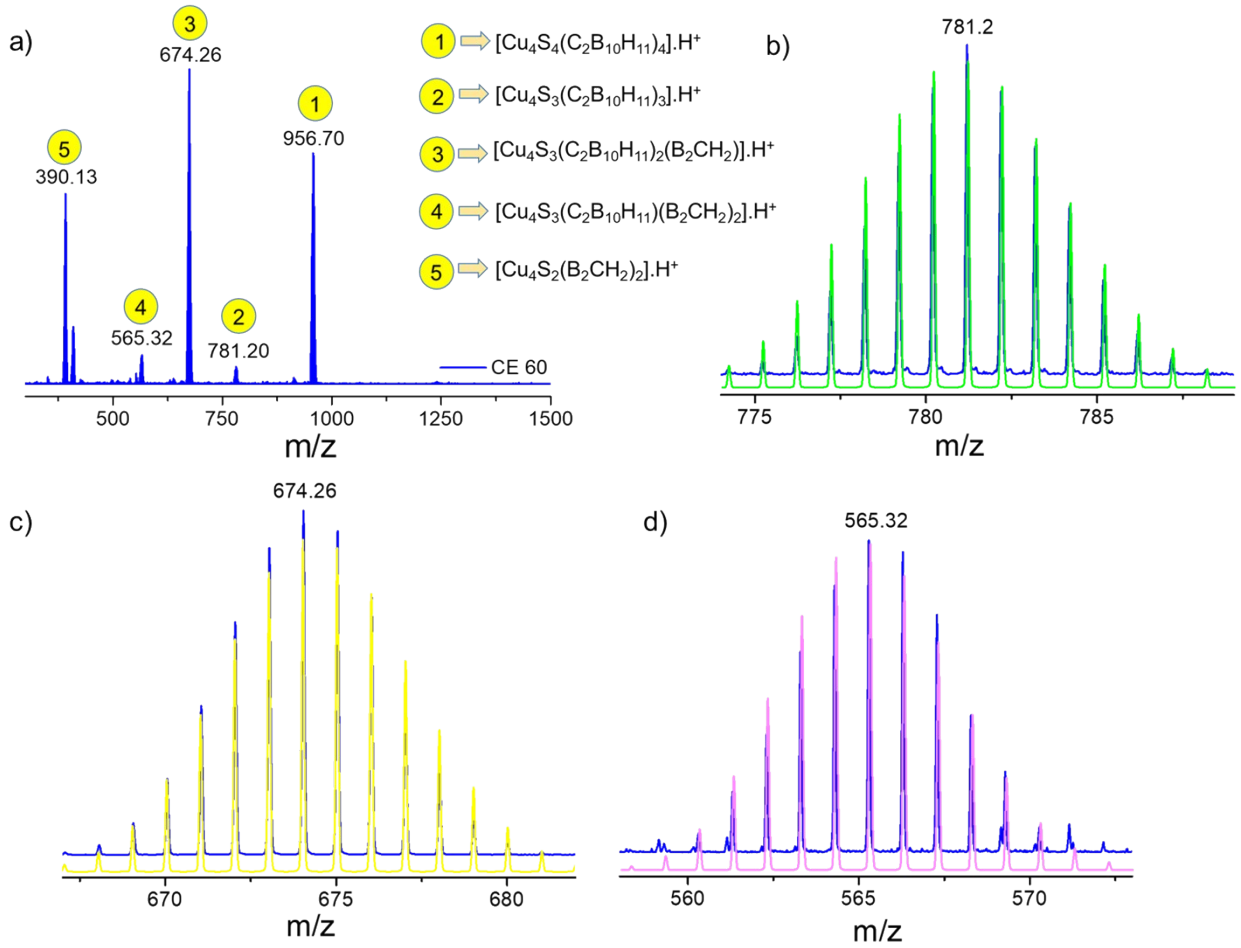

Fig. S13 a) The MS/MS fragmentation pattern of Cu_4@oCBT at CE 60. Experimental isotopic distribution patterns of the fragments were matches with theoretical distribution of b) 781.20, c) 674.26 and d) 565.32 peaks, respectively.

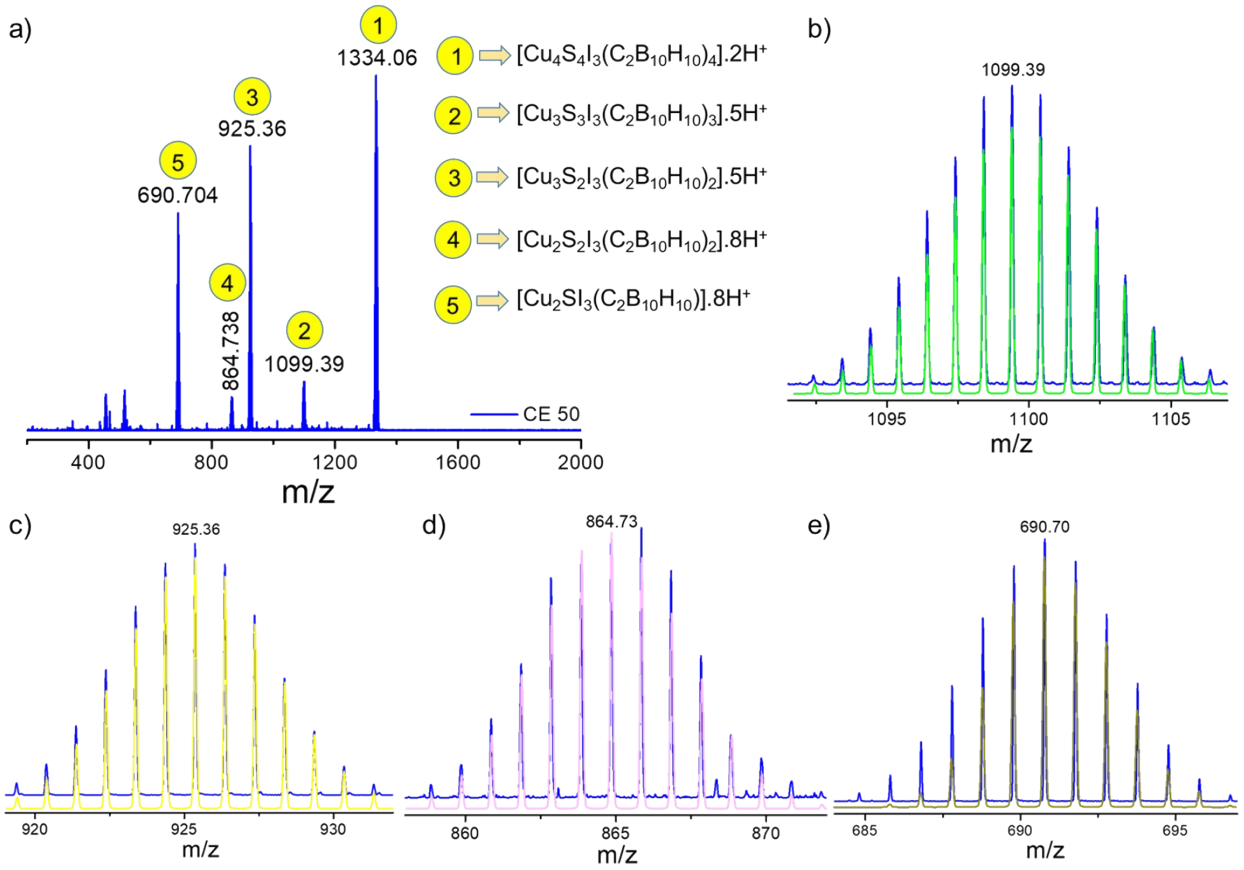

Fig. S14 a) The MS/MS fragmentation pattern of Cu_4@ICBT at CE 50. Experimental isotopic distribution patterns of the fragments were matches well with theoretical distribution of b) 1099.39, c) 925.36, d) 864.73 and e) 690.70 peaks, respectively.

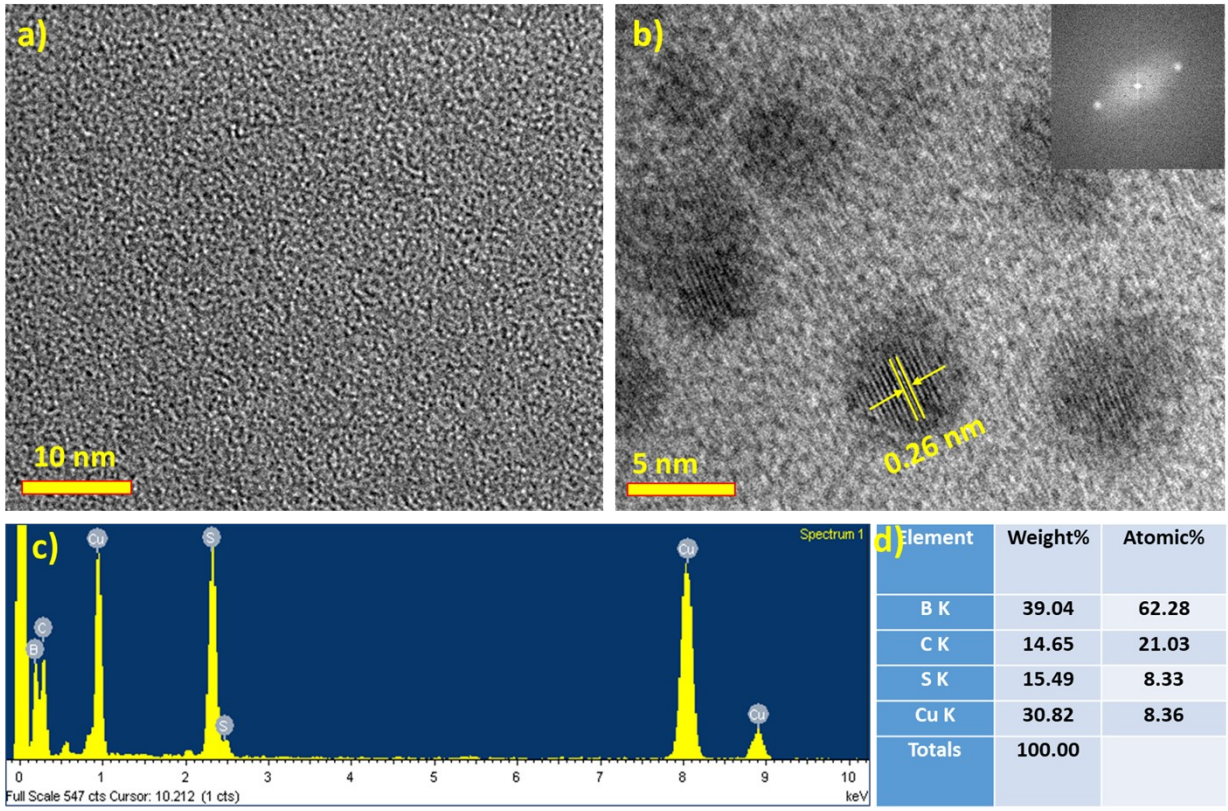

Element	Weight%	Atomic%
B K	39.04	62.28
C K	14.65	21.03
S K	15.49	8.33
Cu K	30.82	8.36
Totals	100.00	

Fig. S15 a) Large area TEM micrograph of Cu_4@oCBT after 2 min beam exposure, b) HRTEM image after 15 min beam exposure shows the formation of lattice with pacing of 0.26 nm (inset shows the diffraction spots), c) EDS spectral profile of the cluster, d) elemental assignments of the cluster.

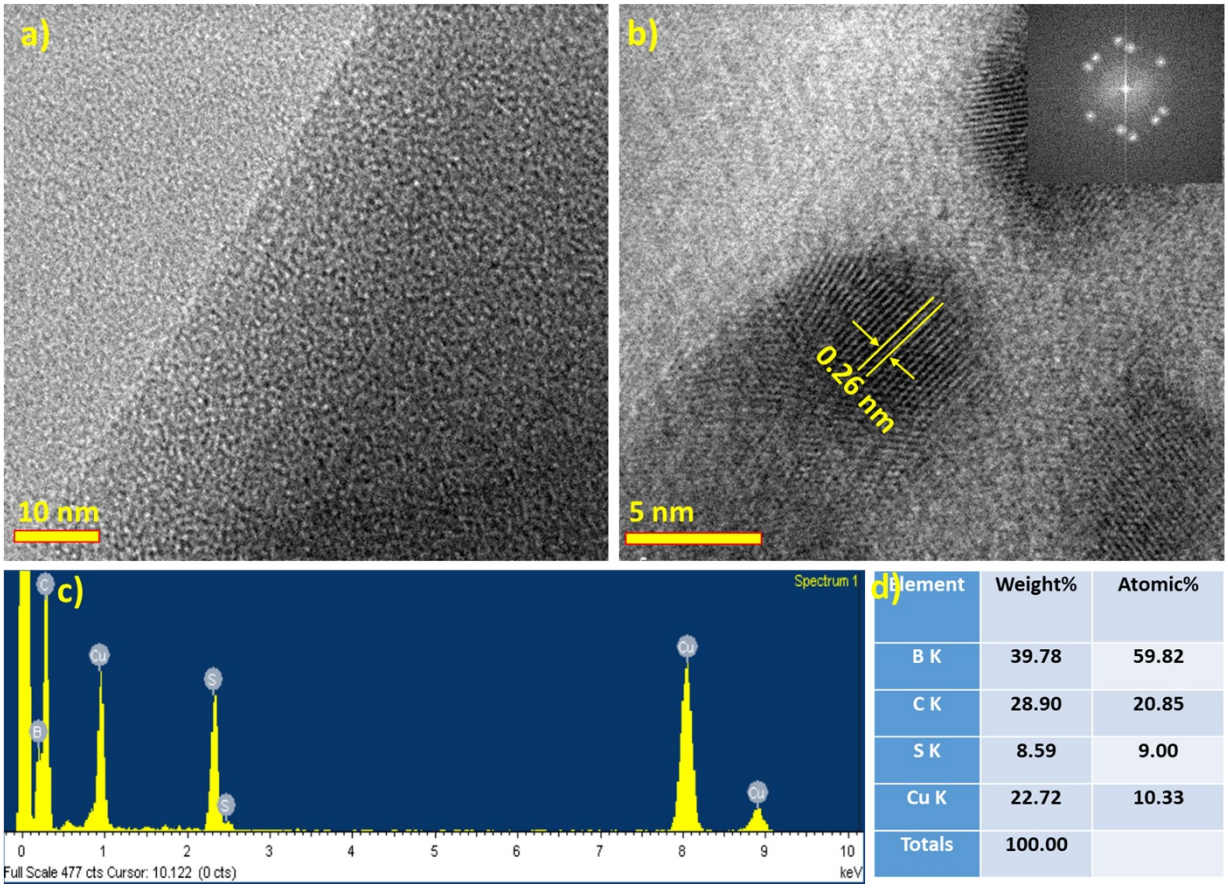

Element	Weight%	Atomic%
B K	39.78	59.82
C K	28.90	20.85
S K	8.59	9.00
Cu K	22.72	10.33
Totals	100.00	

Fig. S16 a) Large area TEM micrograph of the Cu_4@mCBT after 2 min beam exposure. b) HRTEM image of the NC after 15 min beam exposure shows the formation of lattice with lattice spacing 0.26 nm ((inset shows the diffraction spots), c) EDS spectral profile of the cluster, d) elemental assignments of the cluster.

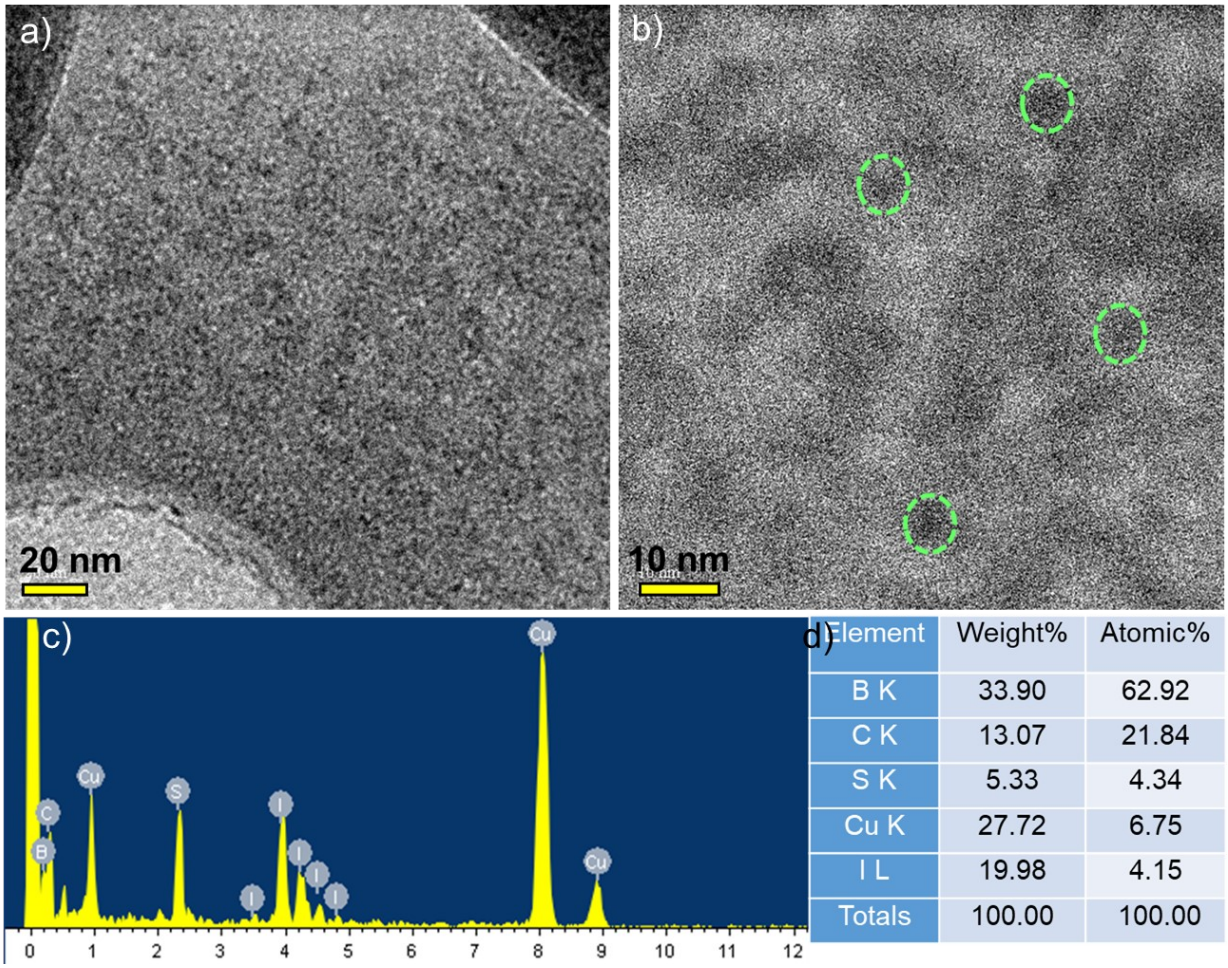

Element	Weight%	Atomic%
B K	33.90	62.92
C K	13.07	21.84
S K	5.33	4.34
Cu K	27.72	6.75
I L	19.98	4.15
Totals	100.00	100.00

Fig. S17 a) Large area TEM micrograph of the Cu_4@ICBT after 2 min beam exposure. b) HRTEM image of the NC after 5 min beam exposure shows the formation of larger particles, c) EDS spectral profile of the cluster, d) elemental assignments of the cluster.

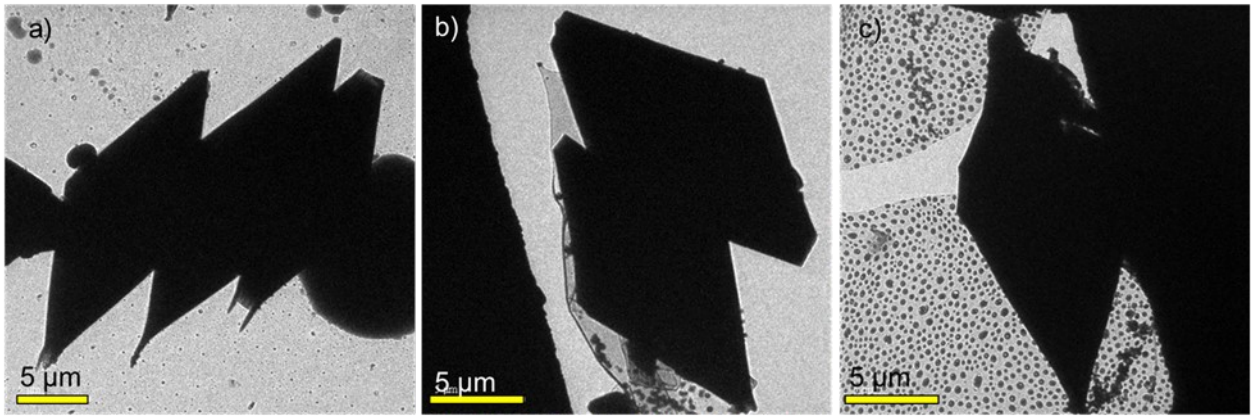

Fig. S18 TEM micrographs of Cu_4@ICBT microcrystals indicate their rhombohedral nature. Diluted cluster leads to the fast formation of microcrystalline materials.

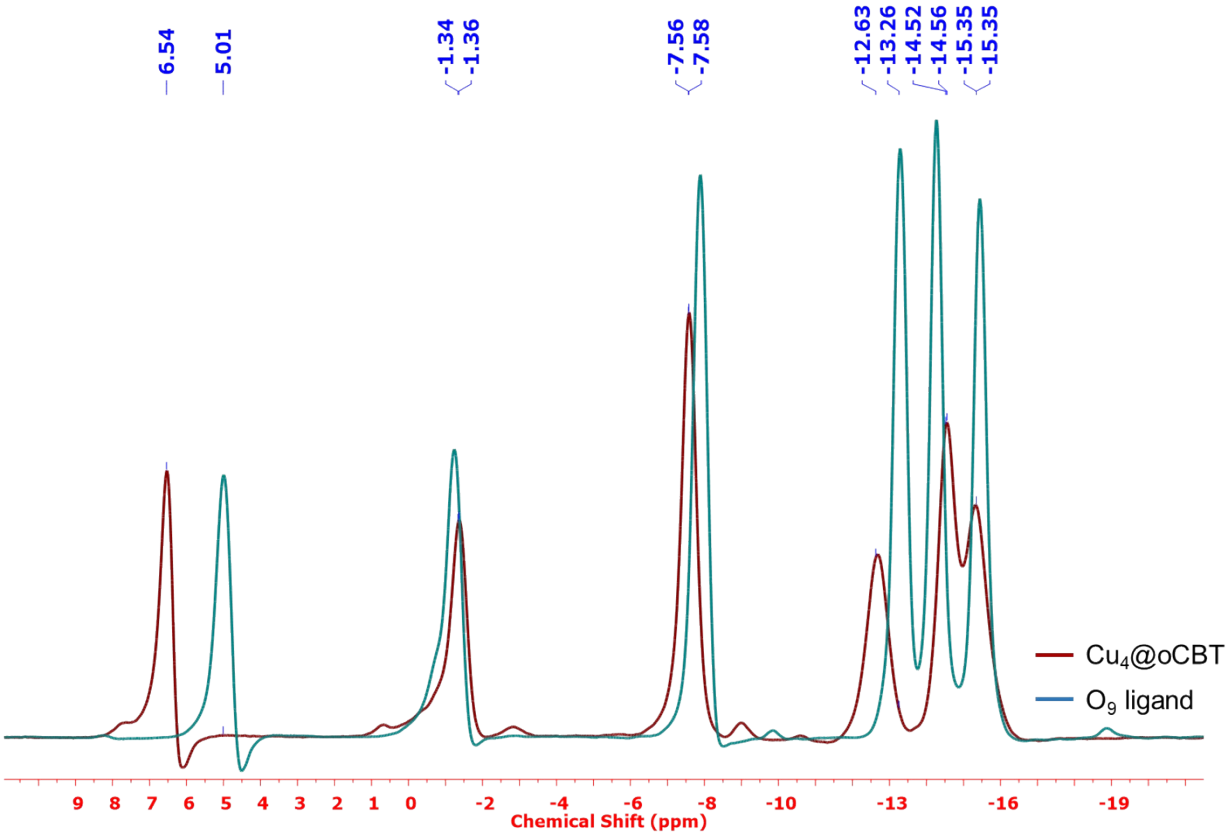

Fig. S19 Combined $^{11}B\{^{1}H\}$ NMR spectra of Cu_4@oCBT and O_9 ligand.

Table S9. $^{11}B\{^{1}H\}$ NMR chemical shift data for Cu_4@oCBT and O_9 ligand.

Chemical shift (ppm) of Cu_4@oCBT	Intensity ratio
6.54, -1.36, -7.56, -12.63, -14.56, -15.35	(1:1:2:1:3:2)
Chemical shift (ppm) of O_9 ligand	
5.01, -1.34, -7.58, -13.26, -14.52, -15.35	(1:1:2:2:2:2)

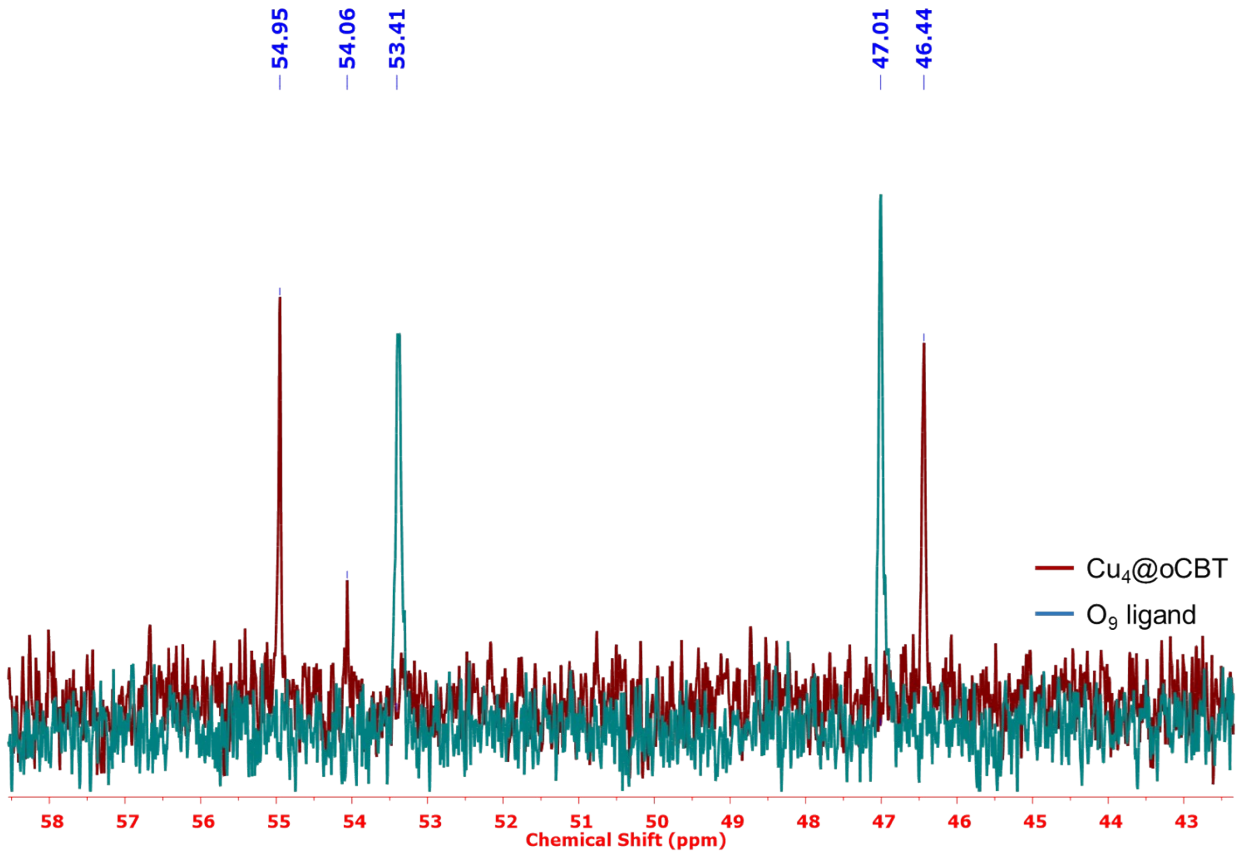

Fig. S20 Combined $^{13}C\{^{1}H\}$ NMR spectra of Cu_4@oCBT and O_9 ligand. δ = 54.06 ppm is due to solvent impurity.

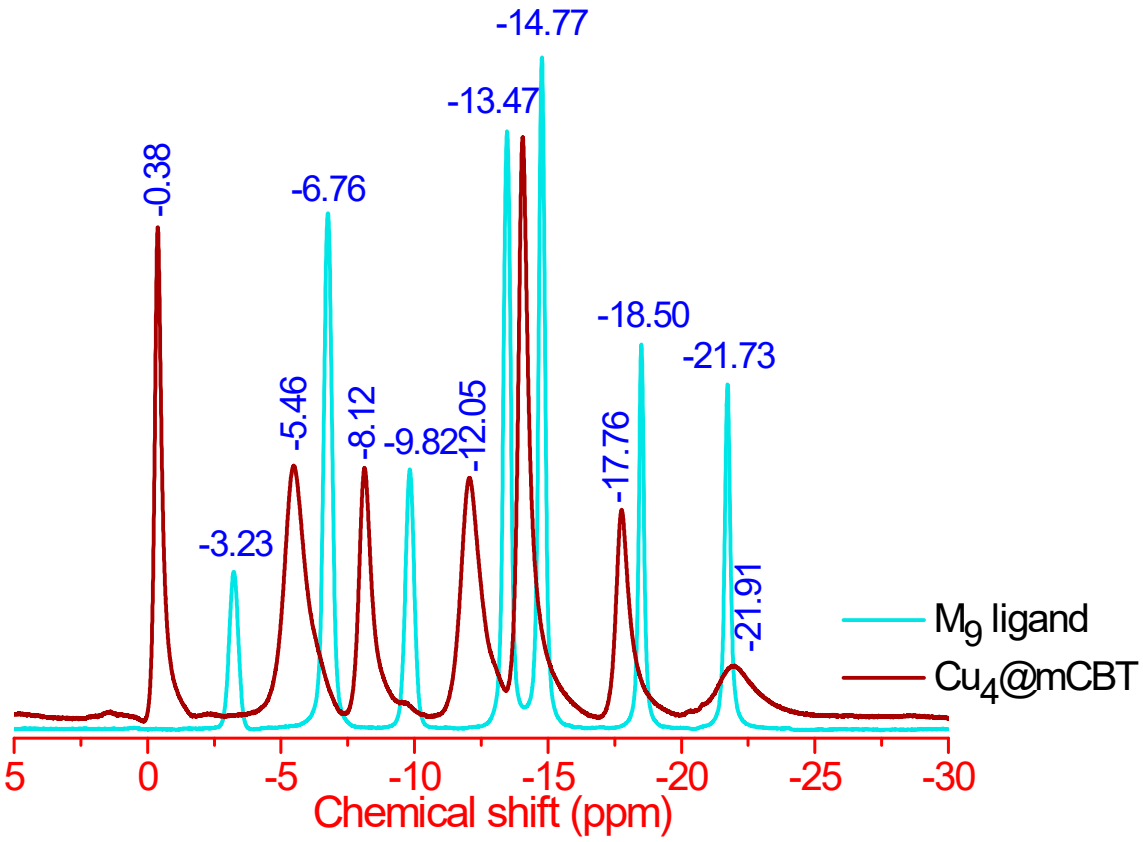

Fig. S21 Combined $^{11}B\{^{1}H\}$ NMR spectra of Cu_4@mCBT and M_9 ligand.

Table S10. $^{11}B\{^{1}H\}$ NMR chemical shift data for Cu_4@mCBT and M_9 ligand.

Chemical shift (ppm) of Cu_4@mCBT	Intensity ratio
-0.38, -5.46, -8.12, -12.05, -14.05, -17.76, -21.91	(1:2:1:2:2:1:1)
Chemical shift (ppm) of M_9 ligand	
-3.23, -6.76, -9.82, -13.47, -14.77, -18.50, -21.73	(1:2:1:2:2:1:1)

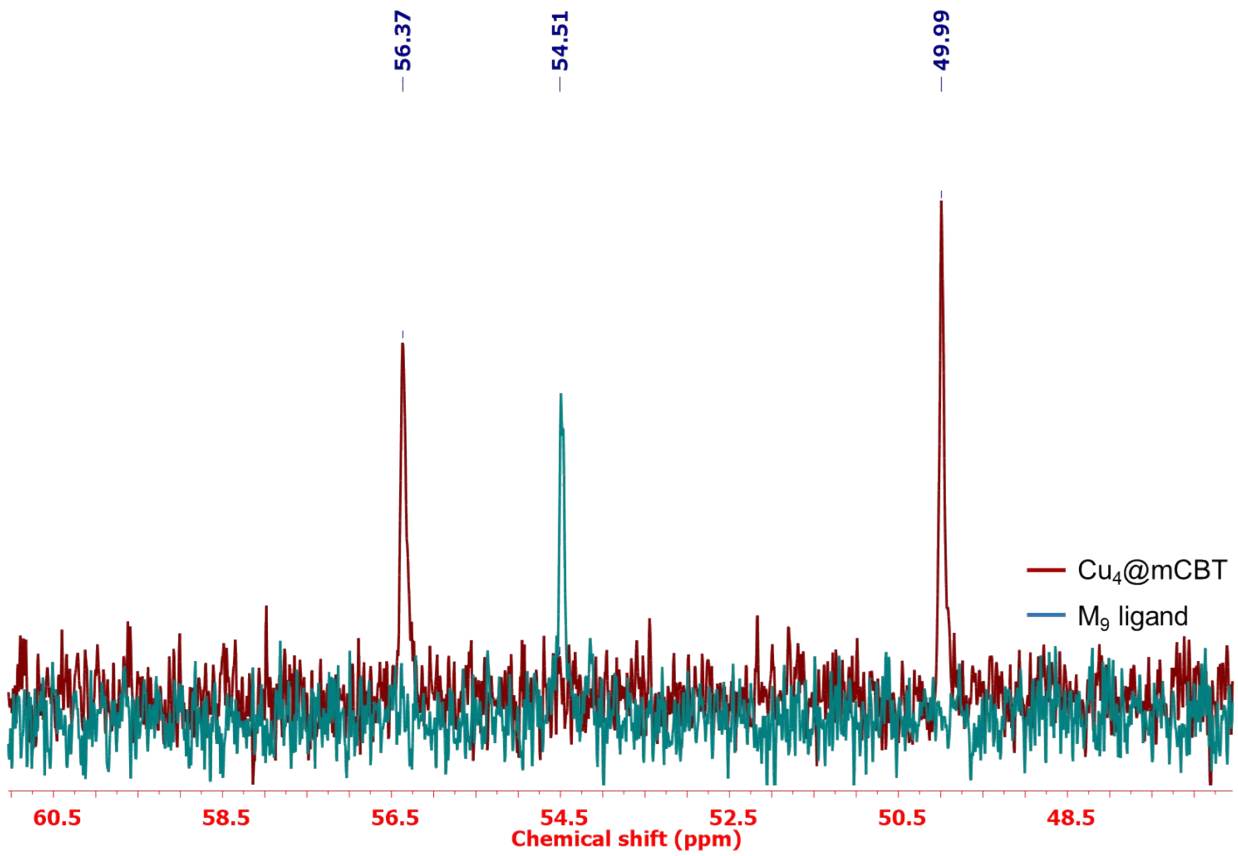

Fig. S22 Combined $^{13}C\{^{1}H\}$ NMR spectra of Cu_4@mCBT and M_9 ligand.

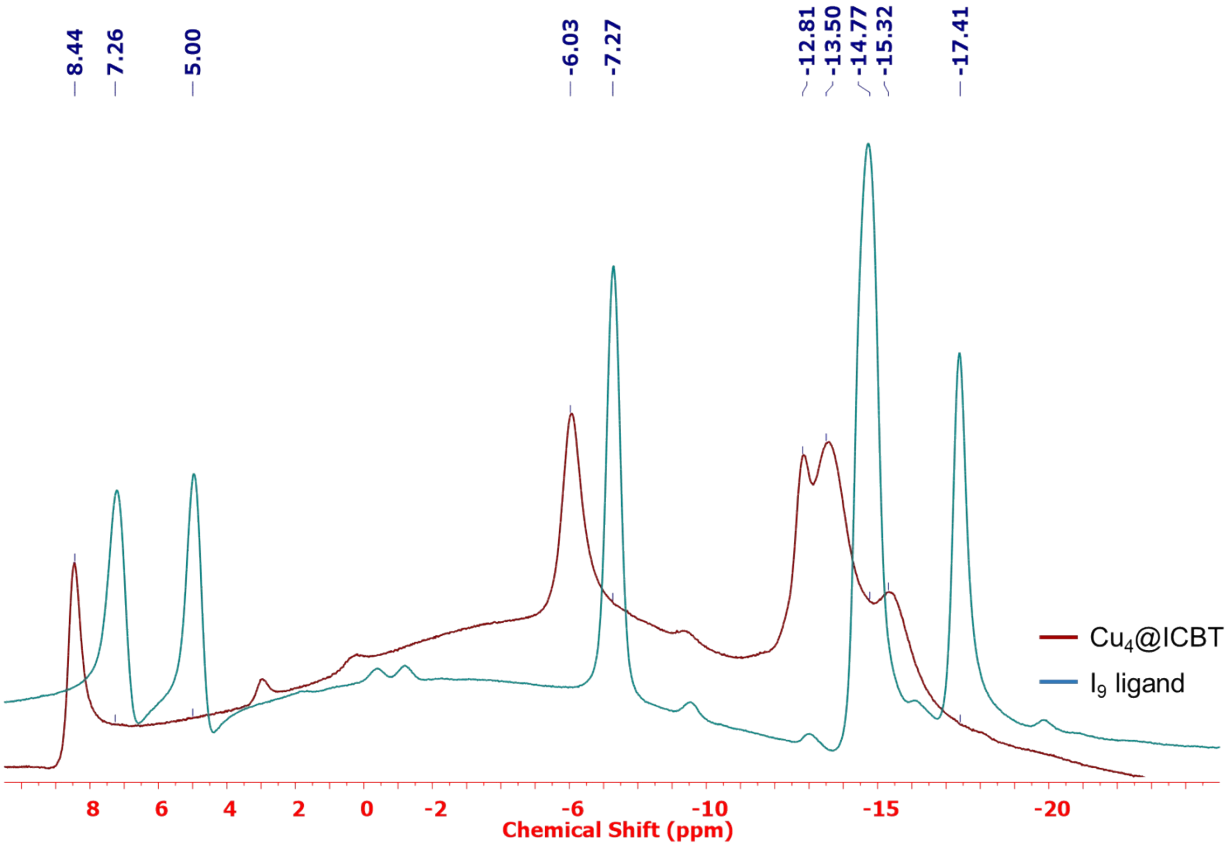

Fig. S23 Combined $^{11}B\{^{1}H\}$ NMR spectra of Cu_4@ICBT and I_9 ligand.

Table S11. $^{11}B\{^{1}H\}$ NMR chemical shift data for Cu_4@ICBT and I_9 ligand.

Chemical shift (ppm) of Cu_4@ICBT	Intensity ratio
8.44, -6.03, -12.81, -13.50, -15.32	(1:3:2:3:1)
Chemical shift (ppm) of I_9 ligand	
7.26, 5.00, -7.27, -14.77, -17.41	(1:1:2:4:2)

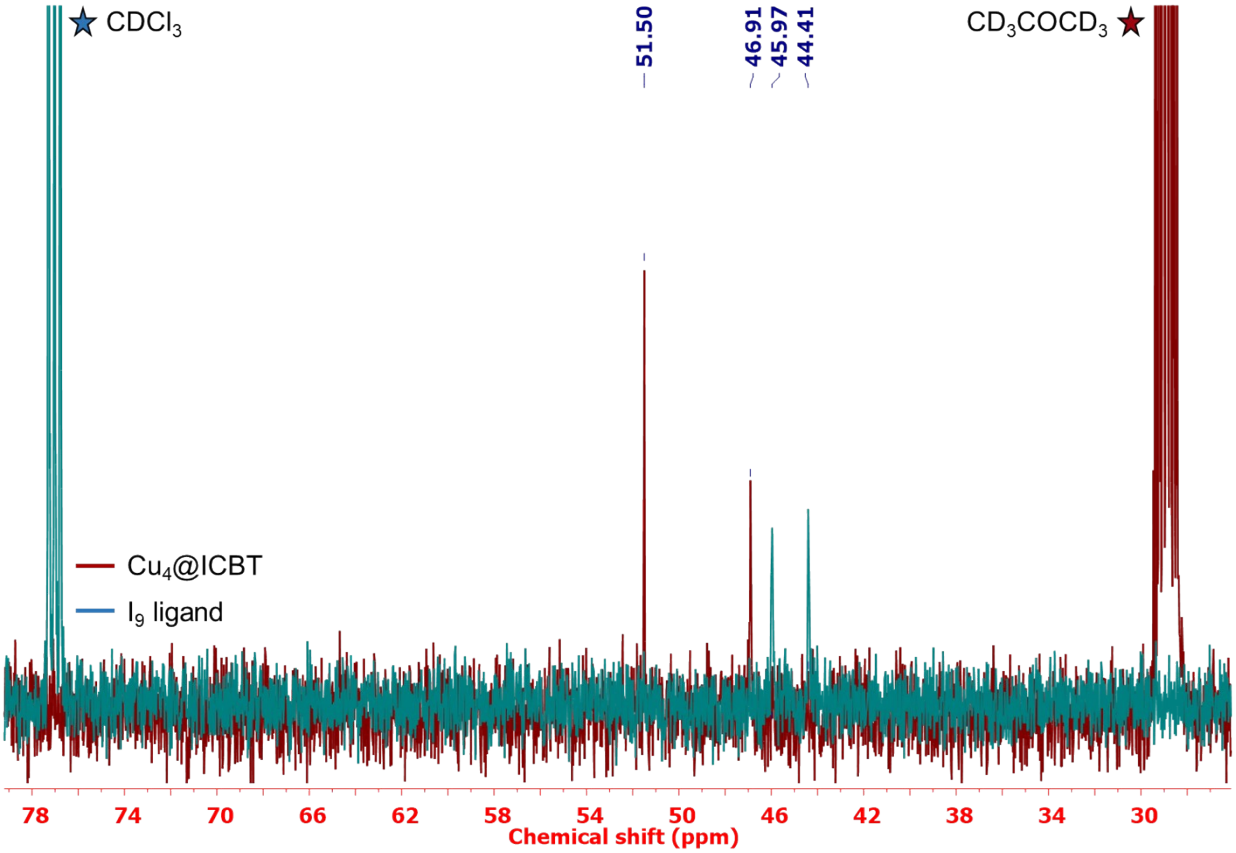

Fig. S24 Combined ^{13}C {^{1}H} NMR spectra of Cu_4@ICBT and I_9 ligand. Solvents peaks are marked in the respective spectrum.

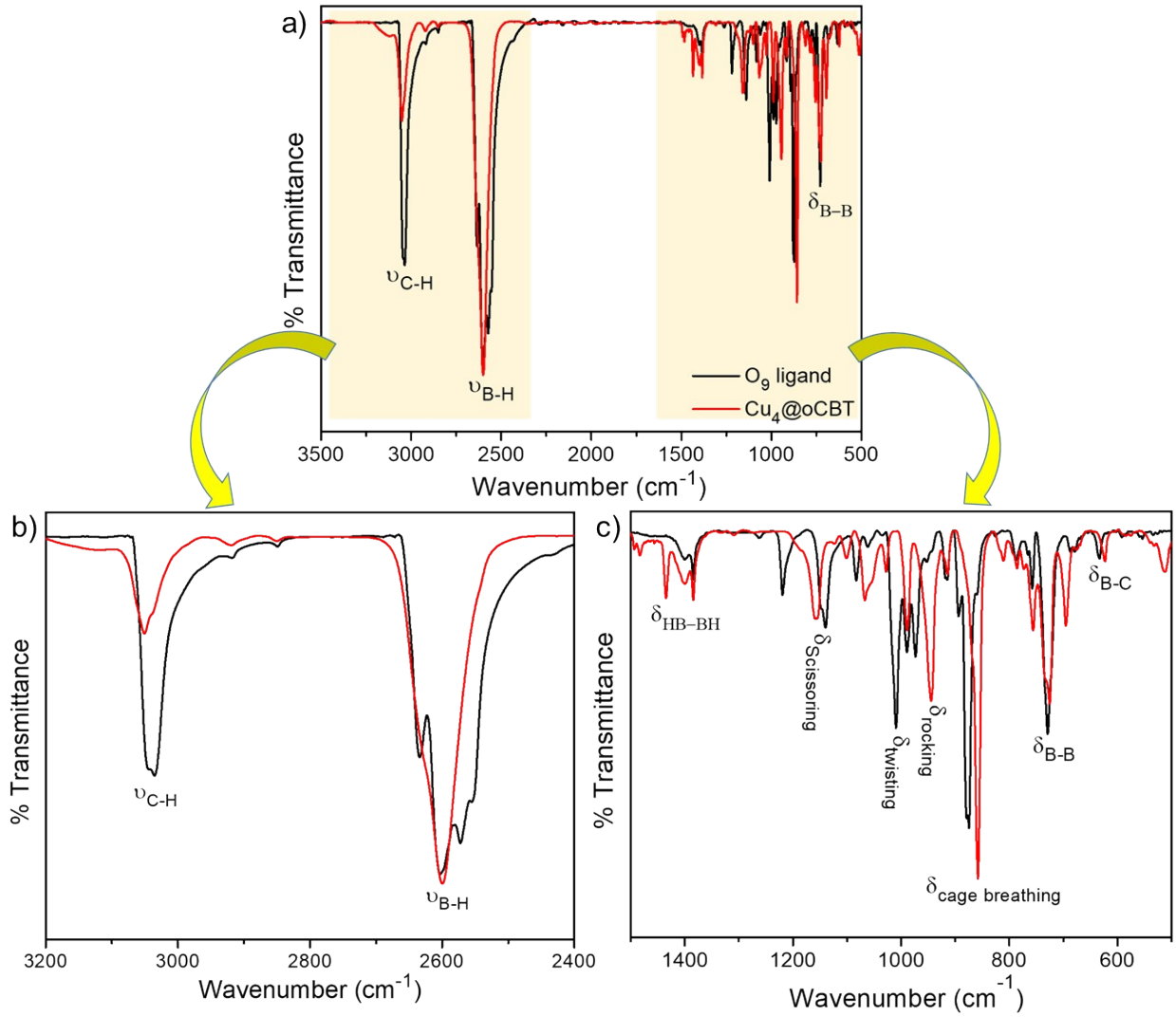

Fig. S25 a) The full range FT-IR spectra of Cu_4@oCBT along with the O_9 ligand. b, c) Enlarged view of the spectral regions. Spectral assignments are performed based on the theoretical calculations shown in Fig. S28.

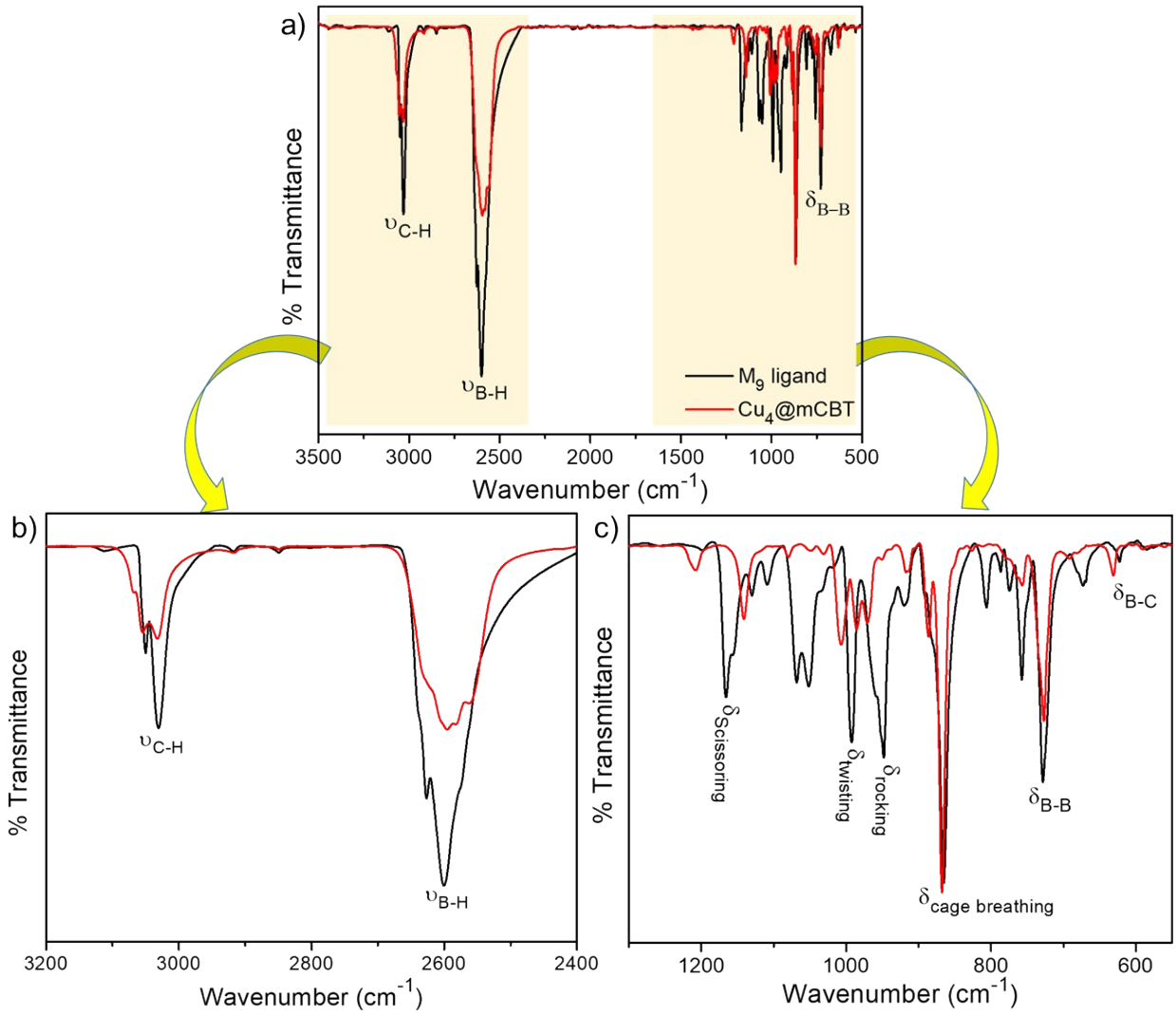

Fig. S26 a) The full range FT-IR spectra of Cu_4@mCBT along with the M_9 ligand. b, c) Enlarged view of the spectral regions.

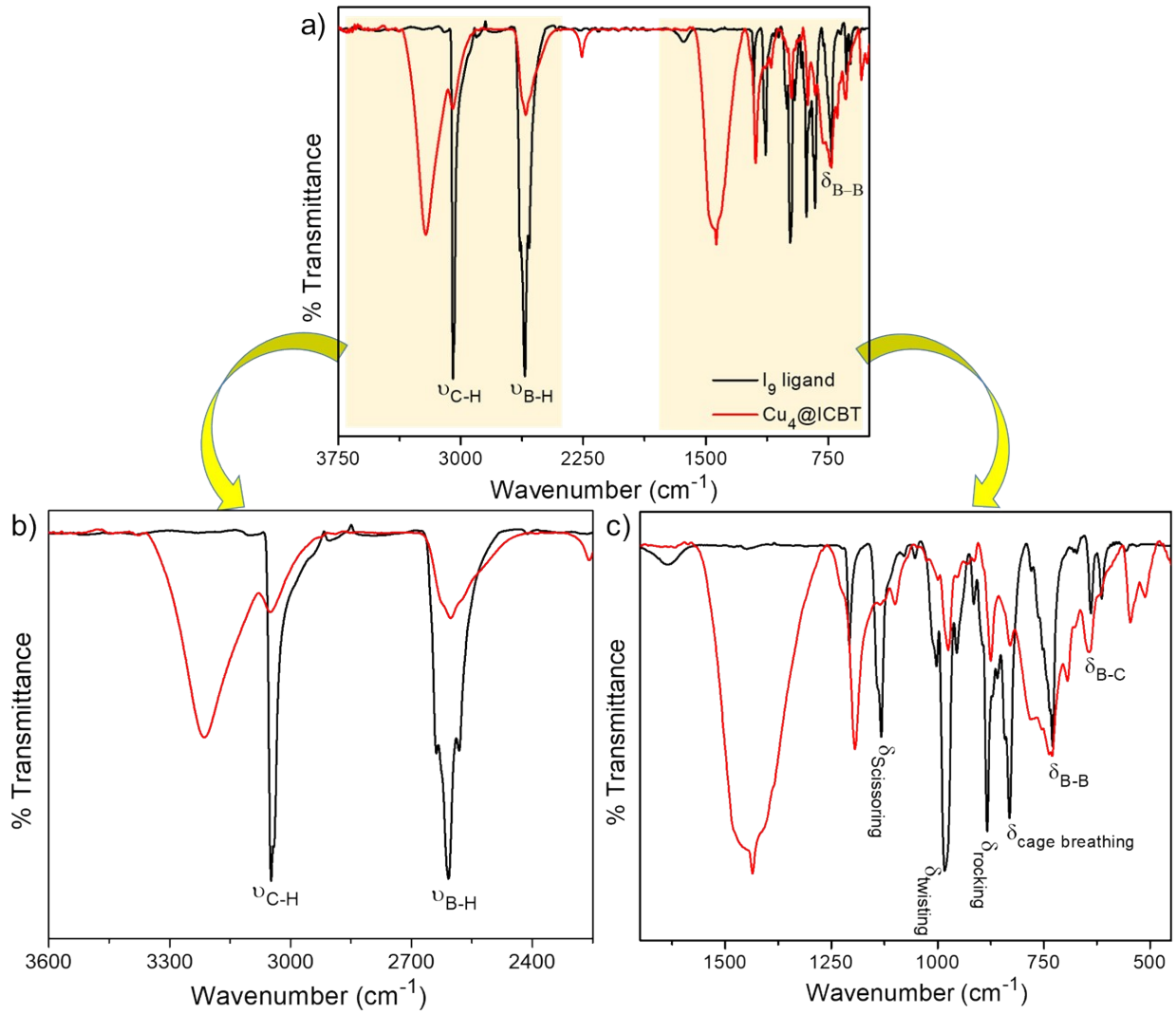

Fig. S27 a) The full range FT-IR spectra of Cu_4@ICBT along with the I_9 ligand. b, c) Enlarged view of the spectral regions. Peaks of interest are marked here.

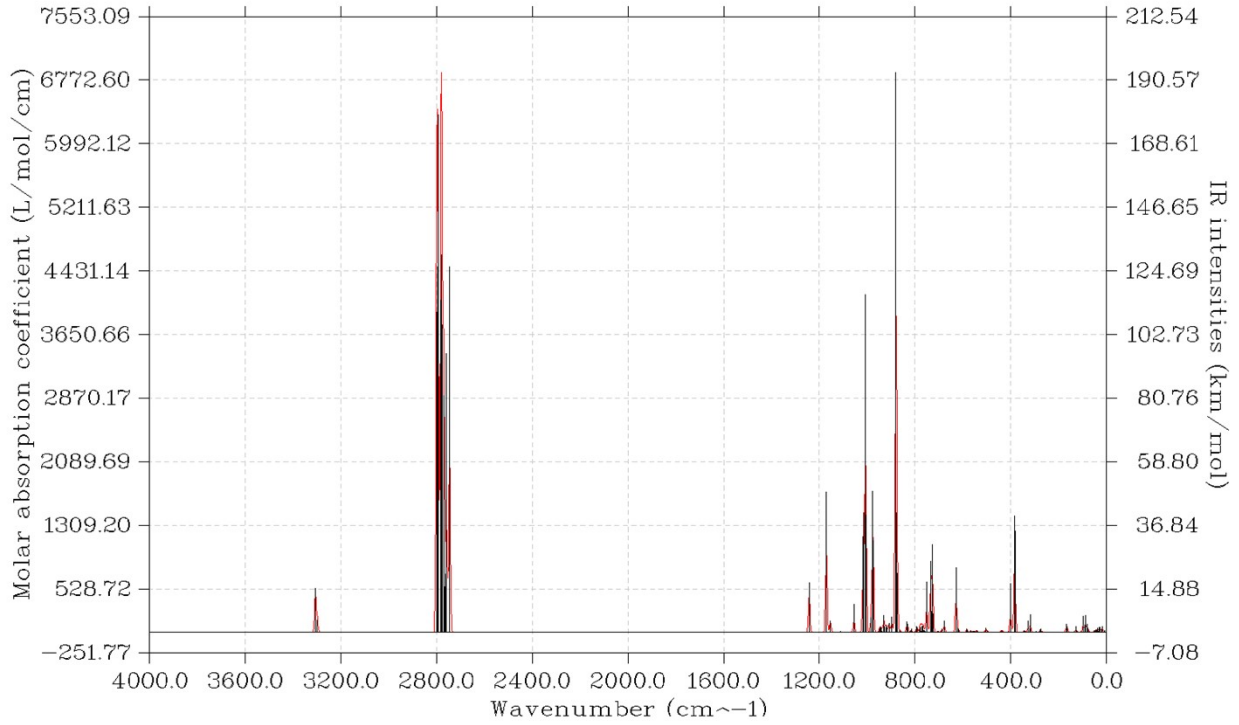

Fig. S28 The calculated IR spectra of Cu_4@oCBT in the gas phase.

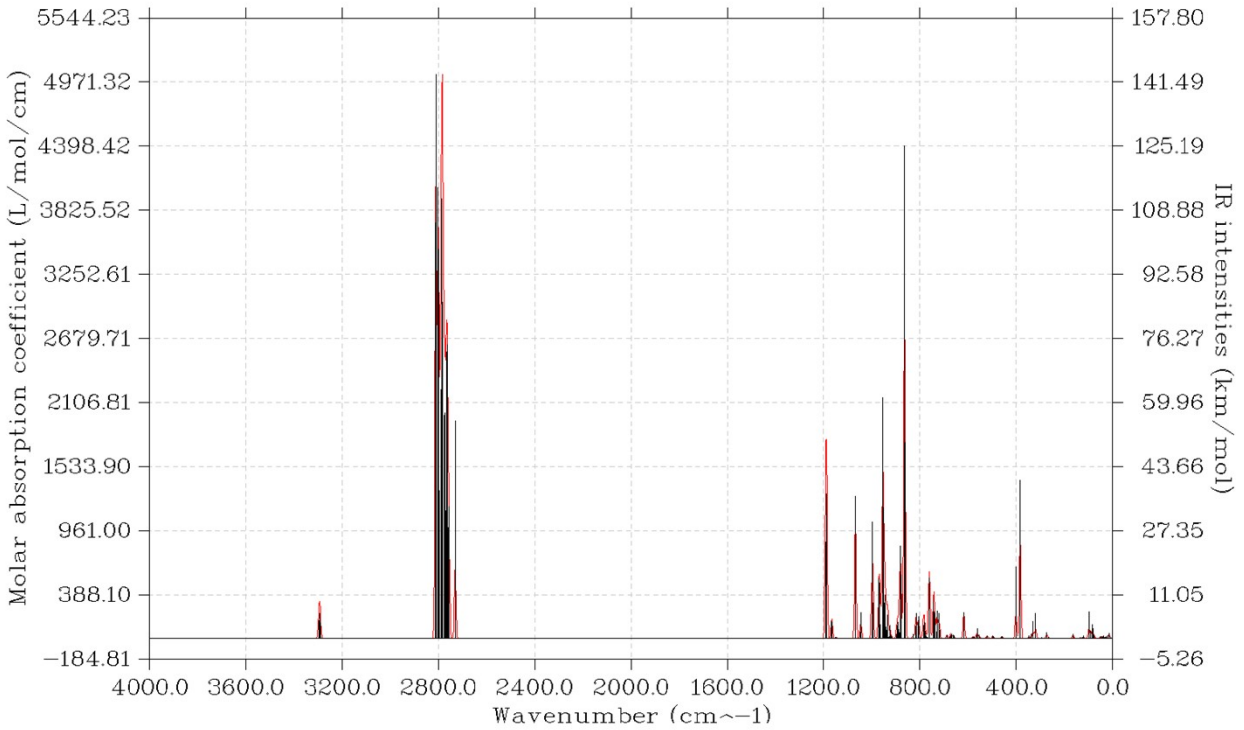

Fig. S29 The calculated IR spectra of Cu_4@mCBT in the gas phase.

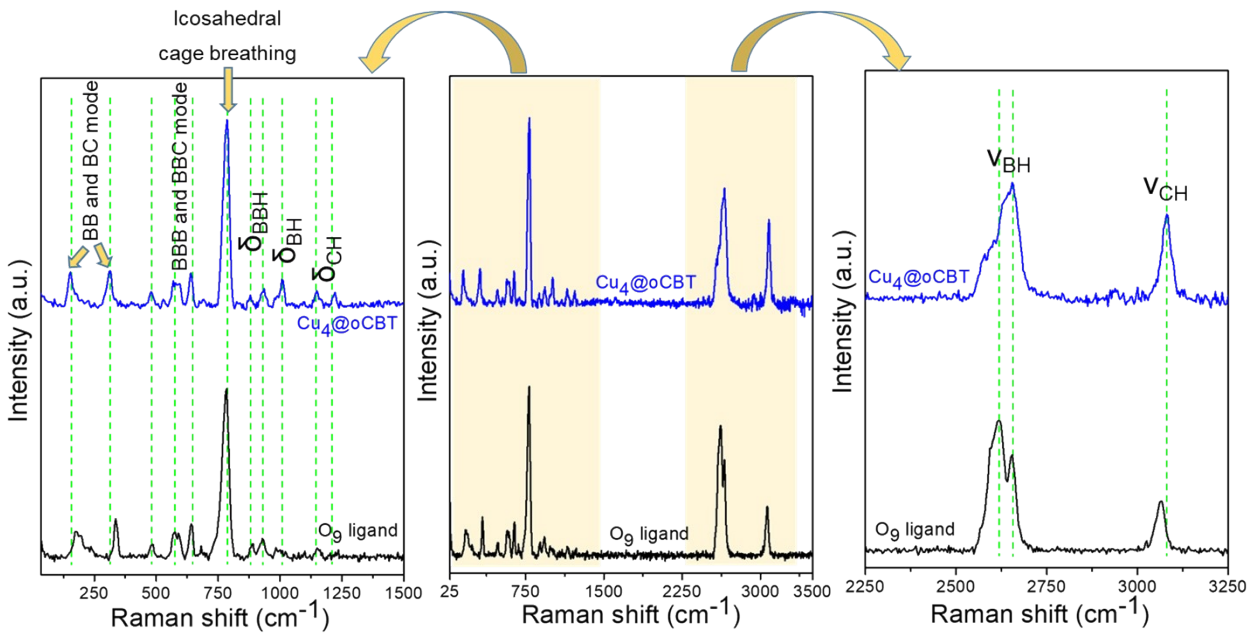

Fig. S30 Raman spectra of Cu_4@oCBT crystals in comparison with O_9 ligand. An expanded view with marked peaks shows the variation of carboranes vibrational modes in the cluster. The 532 nm laser was used for these measurements. Spectral assignments are performed following the literature.[14]

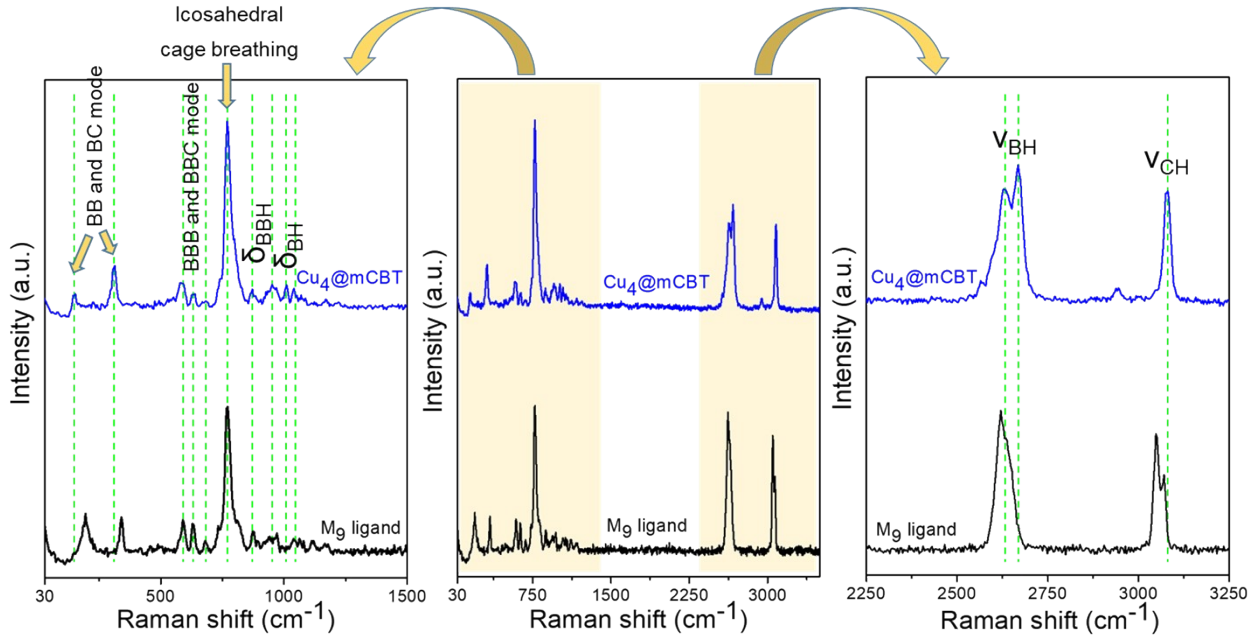

Fig. S31 Raman spectra of Cu_4@mCBT crystals in comparison with M_9 ligand. An expanded view with marked peaks shows the variation of carboranes vibrational modes in the cluster. The 532 nm laser was used for these measurements. Spectral assignments are performed following the literature.[14]

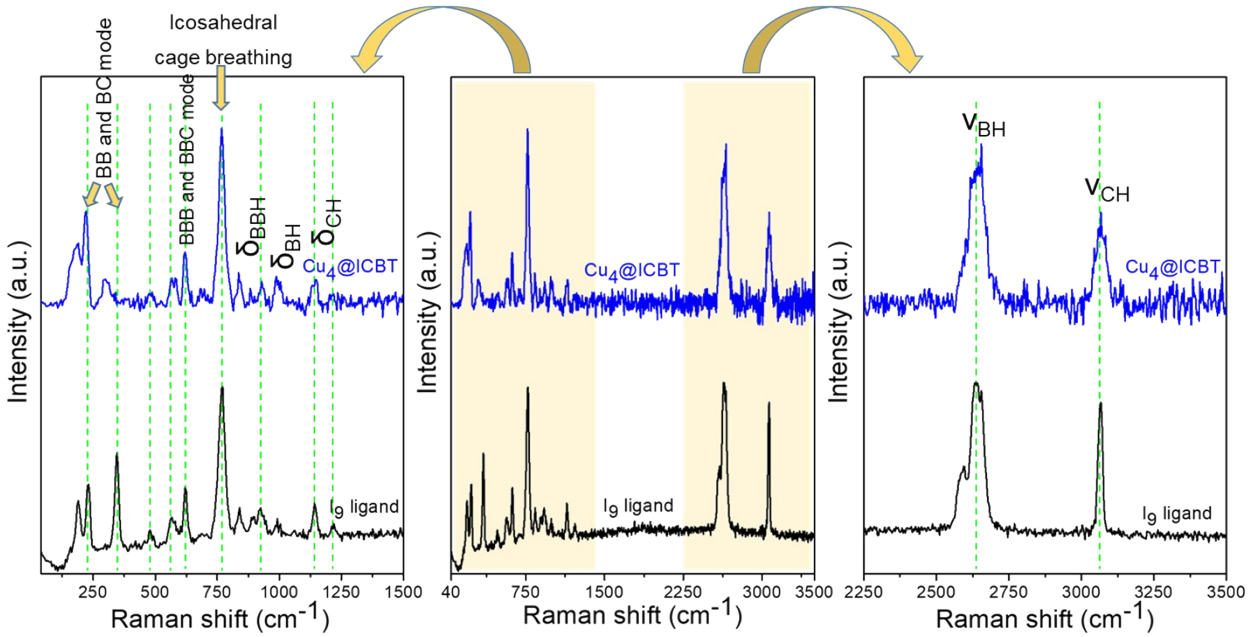

Fig. S32 Raman spectra of Cu_4@ICBT crystals in comparison with the I_9 ligand. An expanded view with marked peaks shows the variation of carboranes vibrational features in the cluster. The 532 nm laser was used for these measurements. Spectral assignments are performed following earlier literature.[14]

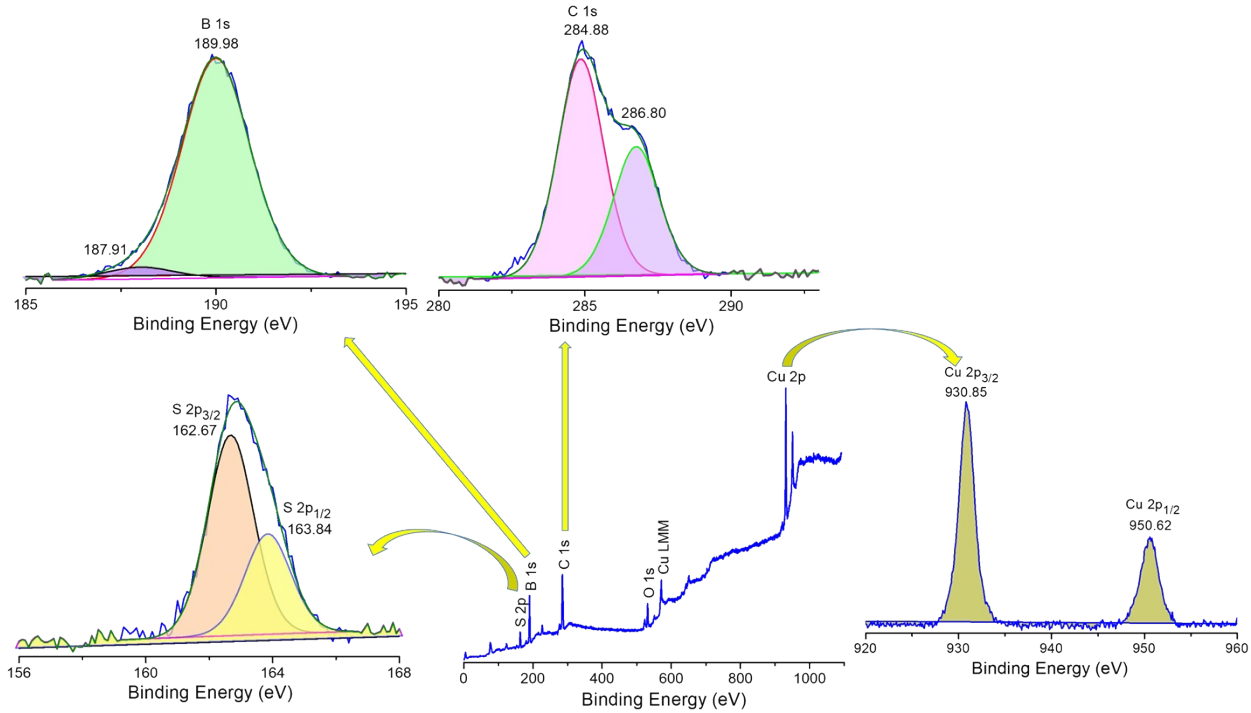

Fig. S33 XPS spectrum of Cu_4@oCBT. The survey spectrum shows the existence of respective elements. Expanded peak fitting of Cu 2p, S 2p, C 1s and B 1s spectral regions.

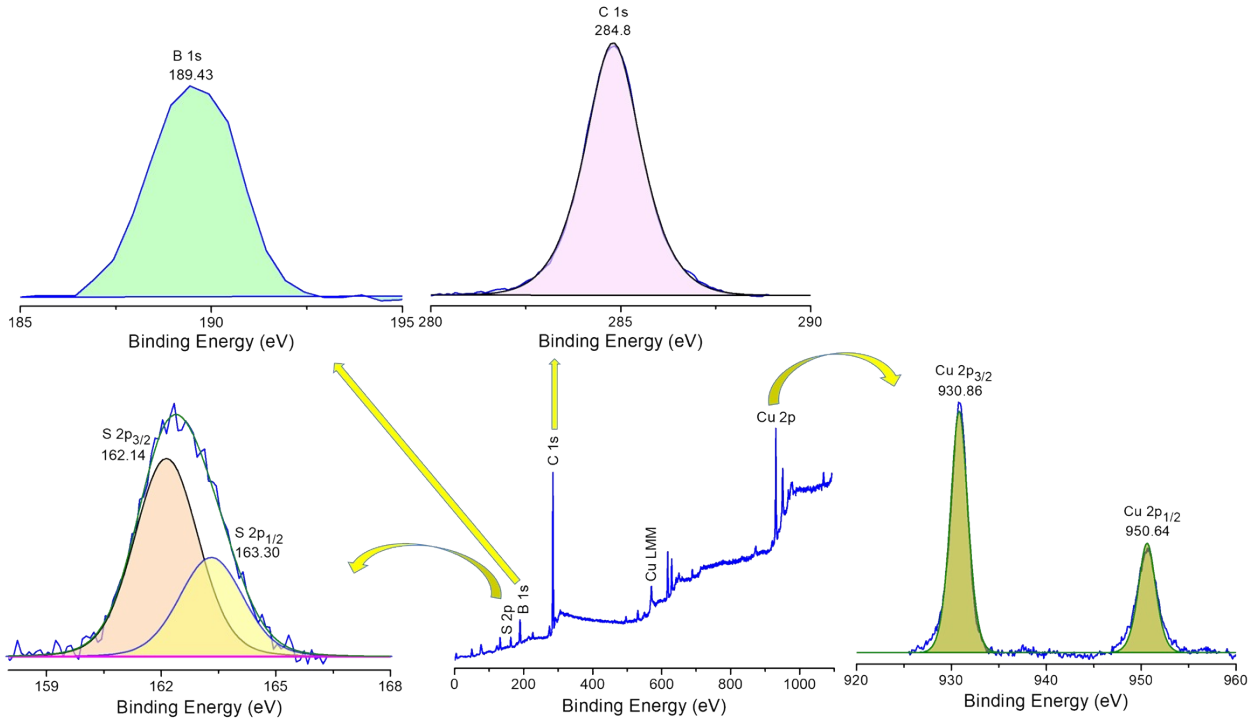

Fig. S34 XPS spectrum of Cu_4@mCBT. The survey spectrum shows the presence of respective elements. Expanded peak fitting of Cu 2p, S 2p, C 1s and B 1s spectral regions.

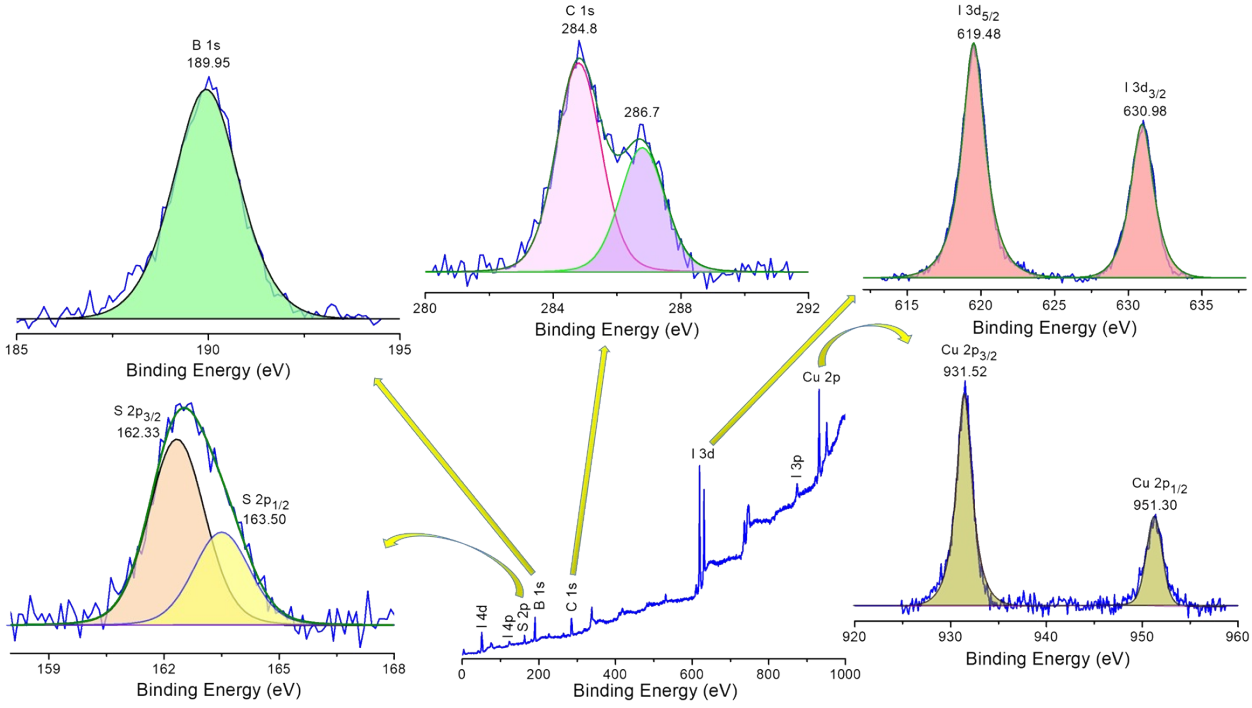

Fig. S35 XPS spectrum of Cu_4@ICBT. The survey XPS spectrum shows the presence of respective elements. Expanded peak fitting of Cu 2p, S 2p, I 3d, C 1s and B 1s spectral regions.

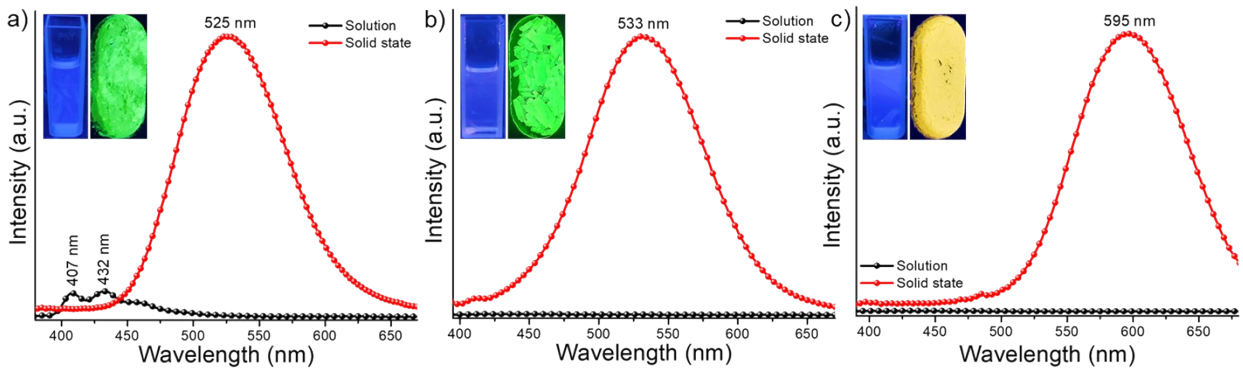

Fig. S36 Photoluminescence spectra of a) Cu_4@oCBT, b) Cu_4@mCBT and c) Cu_4@ICBT in the solid state as well as their respective solution (inset shows the photographic images of the respective clusters under UV lamp both in solution and in solid state).

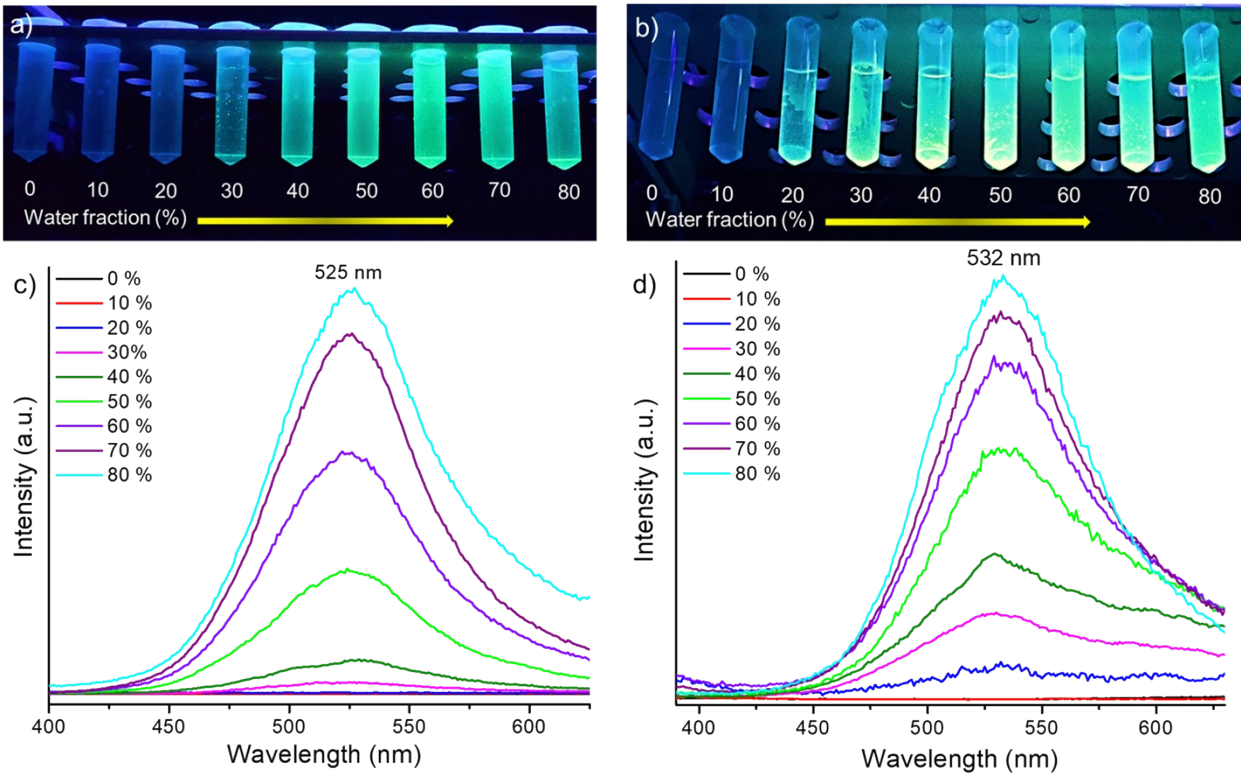

Fig. S37 Photographs of a) Cu_4@oCBT and b) Cu_4@mCBT with varying fraction of water (volume %) indicating AIE behavior of these materials. The respective PL spectra of c) Cu_4@oCBT and d) Cu_4@mCBT with varying fraction of water.

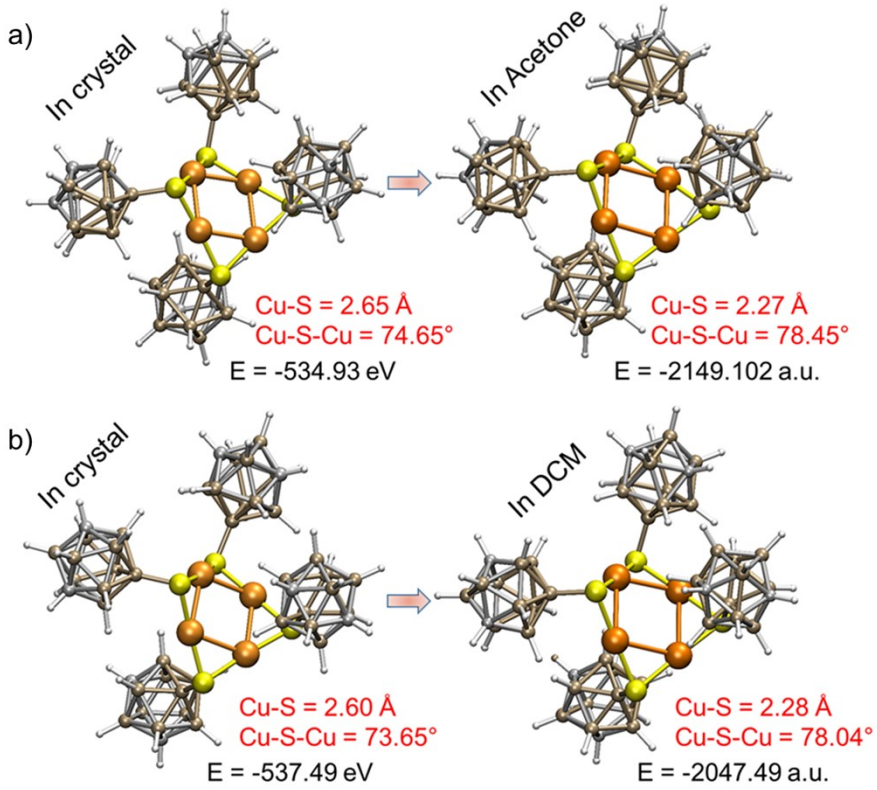

Fig. S38 Structural variation through DFT studies of d) Cu_4@oCBT and e) Cu_4@mCBT in different states. Shortening of the distance of Cu-S bond and expansion of Cu-S-Cu bond angles were observed of these NCs.

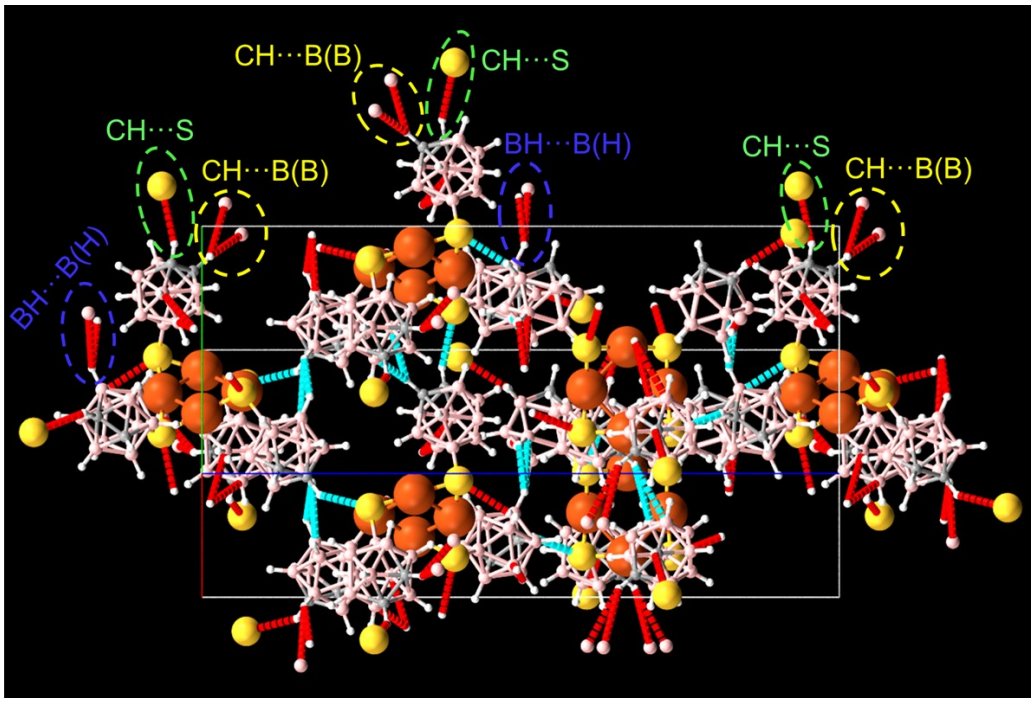

Fig. S39 Different types of intermolecular interactions *i.e.*, CH-S, BH-BH and CH-BB present in Cu_4@oCBT.

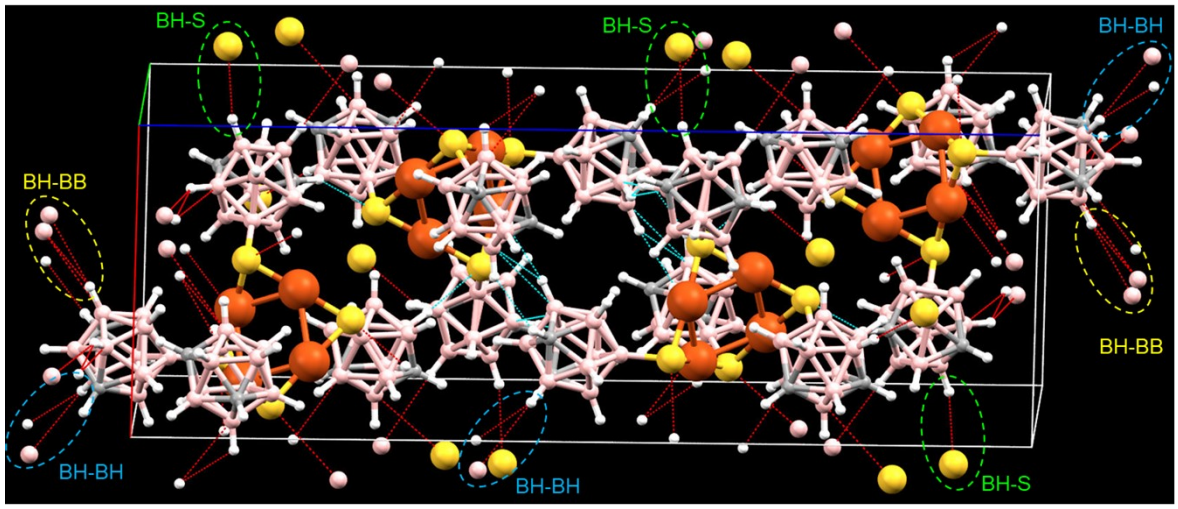

Fig. S40 Different types of intermolecular interactions *i.e.*, BH-S, BH-BH and BH-BB present in Cu_4@mCBT.

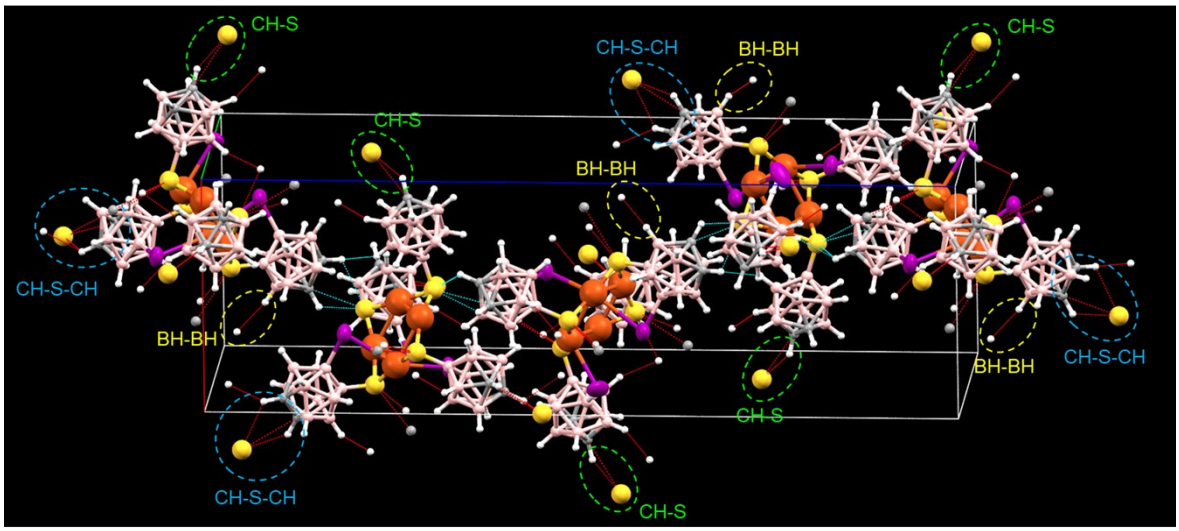

Fig. S41 Different types of intermolecular interactions *i.e.*, CH-S-CH, BH-BH and CH-S present in Cu_4@ICBT.

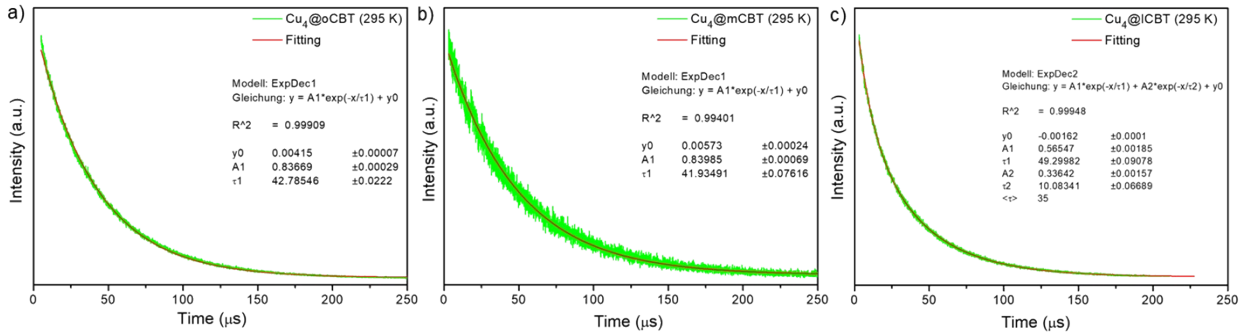

Fig. S42 Lifetime decay profile of a) Cu_4@oCBT, b) Cu_4@mCBT and c) Cu_4@ICBT at 295 K with respective fittings.

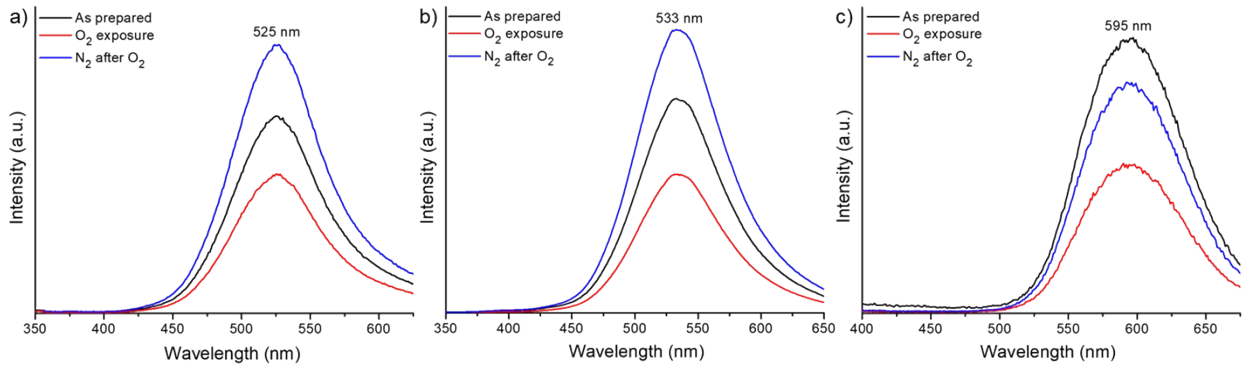

Fig. S43 PL emission spectra of a) Cu_4@oCBT, b) Cu_4@mCBT and c) Cu_4@ICBT clusters before and after oxygen exposure. Reducing of the intensity upon O_2 exposure (exposure time 12 h) suggest emission originating from the triplet state. Subsequent emission enhancement upon N_2 exposure.

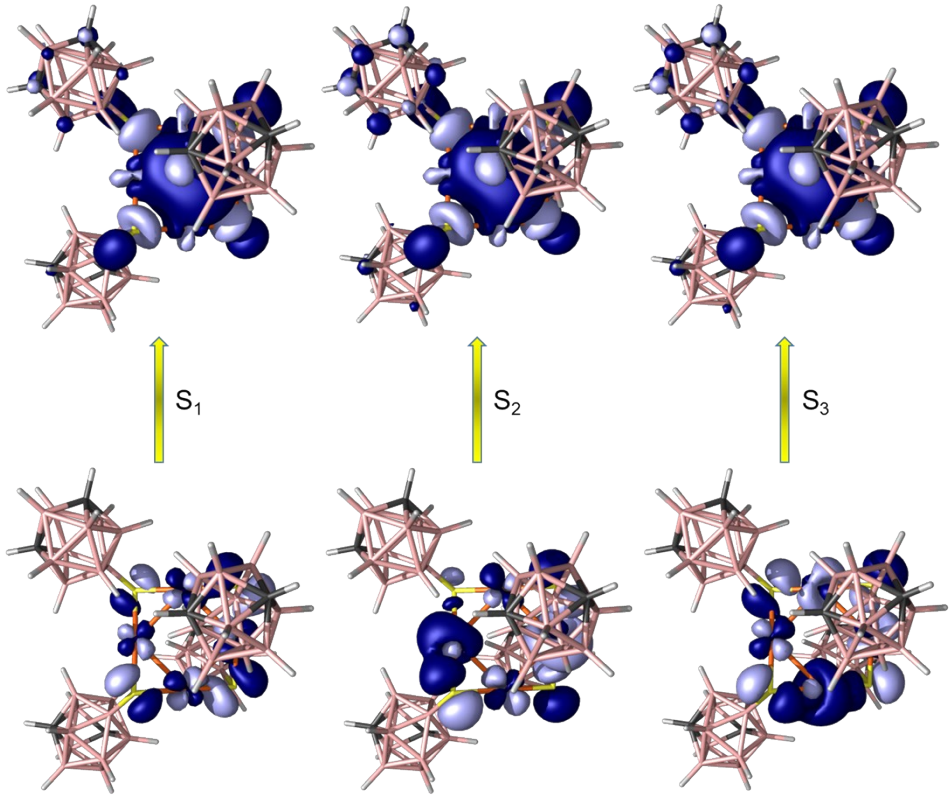

Fig. S44 Natural transition orbitals for first 3 singlet excitations of Cu_4@mCBT.

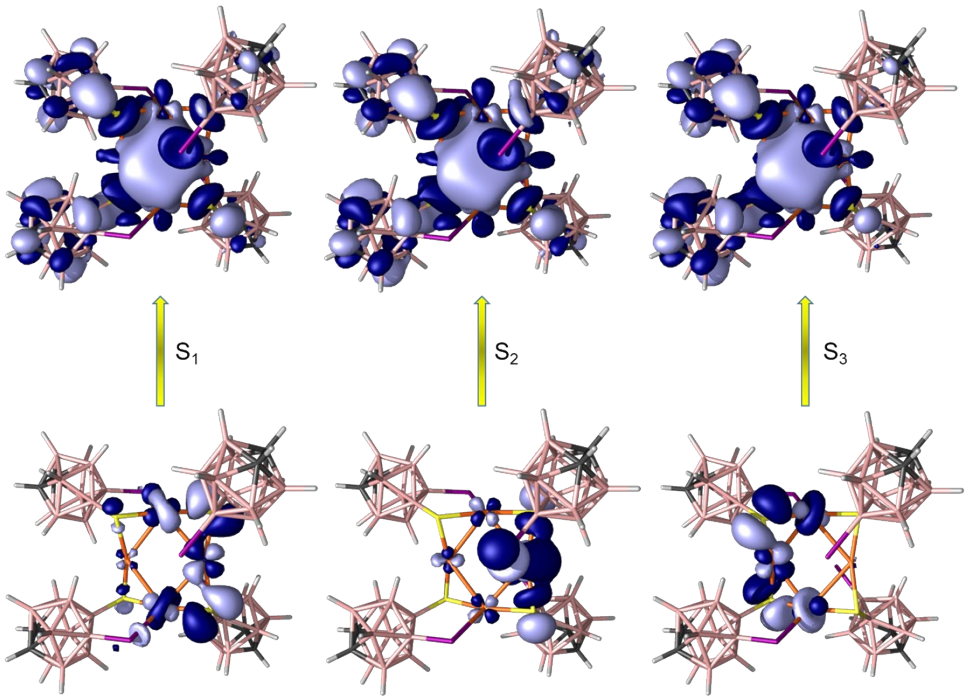

Fig. S45 Natural transition orbitals for first 3 singlet excitations of Cu_4@ICBT.

Table S12. Calculated excited triplet state energies of Cu_4 clusters, in eV.

Cluster	In vacuum (T_1)	In solution (T_1)	X-ray geometry (T_1)	Relaxed triplet (T_1')
Cu_4@oCBT	3.89	3.89	4.09	2.35
Cu_4@mCBT	3.90	3.89	4.19	-
Cu_4@ICBT	3.56	3.62	3.82	1.83

Table S13. Calculated excited triplet state energies of Cu_4 clusters, in nm.

Cluster	In vacuum (T_1)	In solution (T_1)	X-ray geometry (T_1)	Relaxed triplet (T_1')
Cu_4@oCBT	318.45	318.50	303.19	526.95
Cu_4@mCBT	318.18	318.61	296.08	-
Cu_4@ICBT	361.23	343.88	324.36	679.34

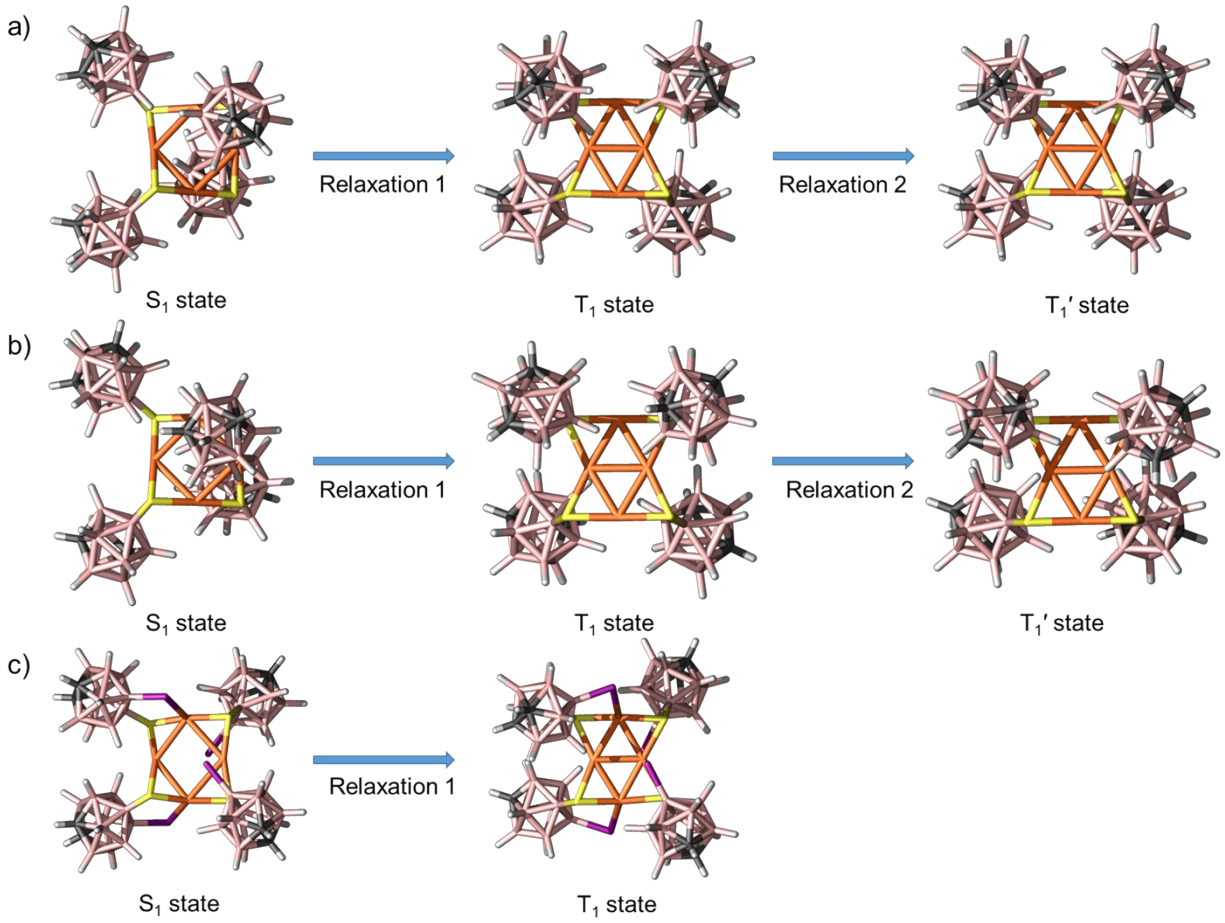

Fig. S46 Singlet to triplet (S_1 to T_1) followed by triplet states (T_1 to T_1') structural relaxations of a) Cu_4@oCBT, b) Cu_4@mCBT and c) Cu_4@ICBT clusters.

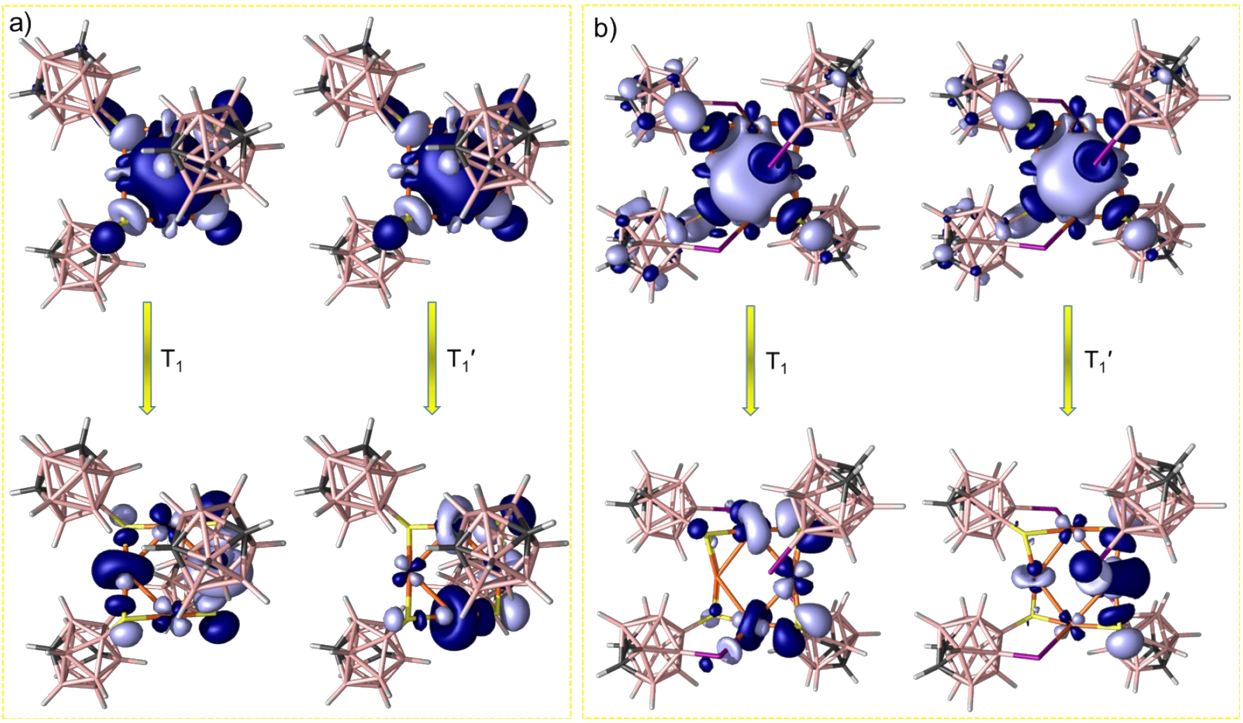

Fig. S47 NTOs of T1 and T1′ radiative relaxation of a) Cu_4@mCBT and b) Cu_4@ICBT clusters.

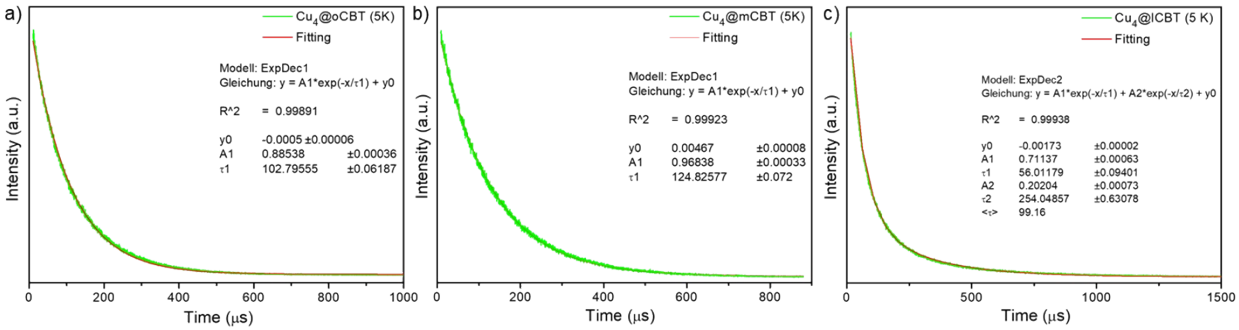

Fig. S48 Lifetime decay profile of a) Cu_4@oCBT, b) Cu_4@mCBT and c) Cu_4@ICBT at 5 K with respective fittings.

Table S14. Assignments of different lattice planes (h k l) of Cu_4@oCBT through simulated PXRD.

Sl. no	Peak position 2θ (degree)	Lattice plane (h k l)
1	9.001	(0 0 3)
2	9.418	(1 0 1)
3	10.76	(1 0 2)
4	12.687	(1 0 3)
5	14.982	(1 0 4)
6	15.484	(2 -1 0)
7	15.777	(2 -1 1)
8	16.621	(2 -1 2)
9	17.515	(1 0 5)
10	17.912	(2 0 0)

11	18.157	(2 0 1)
12	18.896	(2 0 2)
13	19.65	(2 -1 4)
14	20.075	(2 0 3)
15	22.961	(1 0 7)
16	23.46	(2 0 5)
17	23.758	(3 -1 0)
18	23.89	(2 -1 6)
19	24.523	(3 -1 -2)
20	25.453	(3 -1 -3)
21	25.807	(1 0 8)
22	26.699	(3 -1 -4)
23	27.161	(3 0 1)
24	27.673	(3 0 2)
25	28.230	(3 -1 5)
26	29.638	(3 0 -4)
27	30.001	(3 -1 6)
28	30.234	(2 0 8)
29	31.04	(3 0 5)
30	31.266	(4 -2 0)
31	31.482	(2 -1 9)
32	31.976	(3 -1 7)
33	32.69	(3 0 -6)
34	33.15	(4 -1 2)
35	33.61	(4 -2 4)
36	33.865	(4 -1 3)
37	34.143	(3 -1 8)
38	34.512	(3 0 7)
39	34.846	(4 -1 -4)

Table S15. Assignments of different lattice planes (h k l) of Cu_4@mCBT through simulated PXRD.

Sl. no	**Peak position 2θ (degree)**	**Lattice plane (h k l)**
1	5.46	(0 0 2)
2	7.765	(1 0 0)
3	7.881	(0 1 1)
4	9.197	(0 1 2)
5	9.395	(1 0 -2)
6	9.582	(1 0 2)
7	10.723	(1 1 0)
8	11.037	(0 1 3)
9	11.963	(1 1 -2)
10	12.115	(1 1 2)
11	13.413	(1 1 -3)
12	13.611	(1 1 3)
13	15.220	(1 1 -4)
14	15.539	(2 0 0)
15	15.805	(0 2 2)
16	16.986	(1 2 1)

17	17.559	(1 1 5)
18	17.674	(1 2 2)
19	18.059	(1 0 -6)
20	18.353	(1 0 6)
21	18.597	(1 2 -3)
22	18.962	(2 1 -3)
23	19.251	(2 1 3)
24	20.141	(1 2 4)
25	20.633	(2 1 4)
26	21.788	(1 2 5)
27	22.29	(2 1 5)
28	22.982	(0 3 2)
29	23.206	(2 2 3)
30	23.410	(3 0 0)
31	23.816	(1 3 1)
32	24.339	(0 2 7)
33	24.672	(3 1 -1)
34	25.114	(1 3 3)
35	25.779	(3 1 -3)
36	26.104	(3 1 3)
37	26.259	(0 3 5)
38	27.013	(2 2 -6)
39	27.421	(2 2 6)
40	27.801	(2 1 -8)
41	28.64	(2 3 3)
42	29.361	(2 3 -4)
43	30.156	(3 2 4)
44	30.803	(2 3 5)
45	31.05	(0 4 3)
46	31.698	(3 1 7)
47	31.991	(4 0 2)
48	32.183	(1 1 -11)
49	32.706	(3 3 1)
50	32.945	(3 3 -2)
51	33.401	(2 3 -7)
52	33.525	(4 1 3)
53	33.96	(3 0 -9)
54	34.384	(1 3 -9)

Table S16. Assignments of different lattice planes (h k l) of Cu_4@ICBT through simulated PXRD.

Sl. no	**Peak position 2θ (degree)**	**Lattice plane (h k l)**
1	7.3	(1 0 1)
2	8.247	(1 0 2)
3	8.879	(0 0 4)
4	9.62	(1 0 3)
5	10.07	(1 1 1)
6	10.79	(1 1 2)

7	11.28	(1 0 4)
8	11.878	(1 1 3)
9	13.11	(1 0 5)
10	13.256	(1 1 4)
11	13.91	(2 0 0)
12	14.85	(1 1 5)
13	15.045	(1 0 6)
14	15.44	(2 0 3)
15	15.56	(2 1 0)
16	16.2	(2 1 2)
17	16.55	(2 0 4)
18	16.95	(2 1 3)
19	17.83	(2 0 5)
20	19.15	(1 0 8)
21	19.32	(2 0 6)
22	20.55	(2 1 6)
23	21.06	(3 0 1)
24	22.089	(3 1 0)
25	22.19	(3 1 1)
26	22.38	(1 1 9)
27	22.53	(3 1 2)
28	22.67	(2 0 8)
29	22.77	(3 0 4)
30	23.09	(3 1 3)
31	23.86	(3 1 4)
32	24.49	(2 0 9)
33	25.23	(3 2 0)
34	25.31	(3 2 1)
35	25.49	(2 1 9)
36	27.321	(2 1 10)
37	28.516	(3 1 8)
38	29.772	(3 2 7)
39	29.958	(2 2 10)
40	31.179	(2 1 12)
41	31.754	(4 2 2)
42	32.436	(3 2 9)
43	32.737	(4 2 4)
44	33.276	(3 1 11)
45	34.294	(3 0 12)

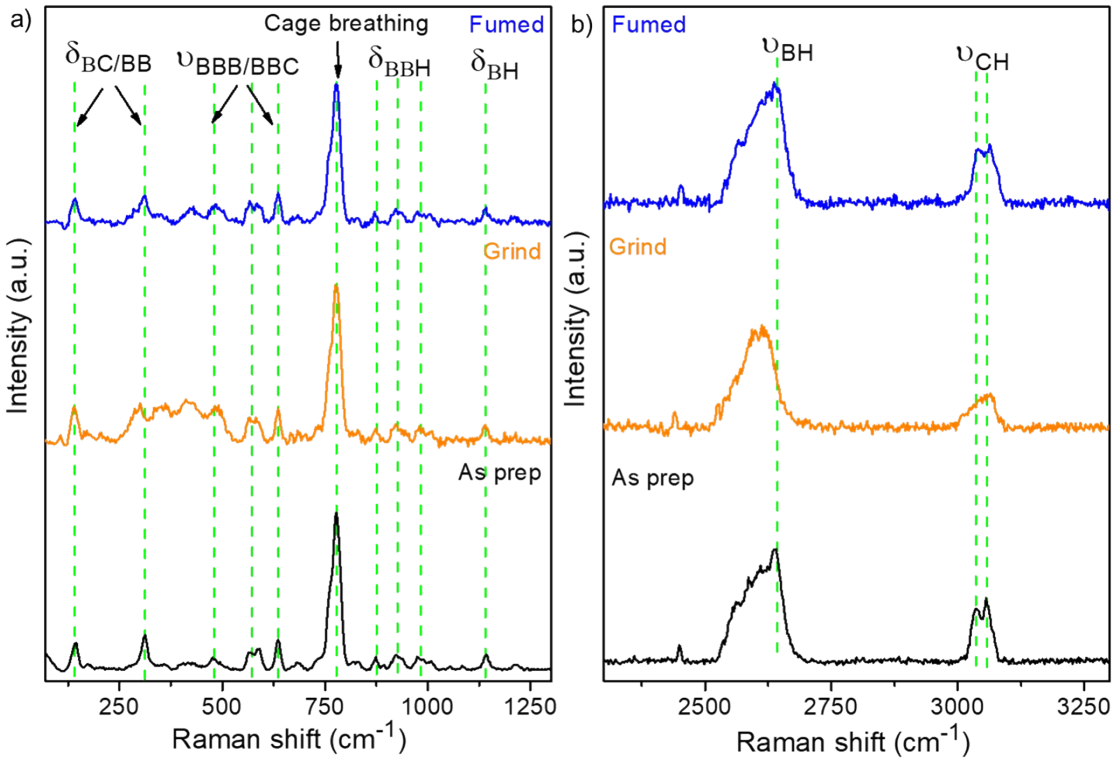

Fig. S49 Comparative Raman spectra of Cu_4@oCBT during mechanical grinding and solvent fuming experiment.

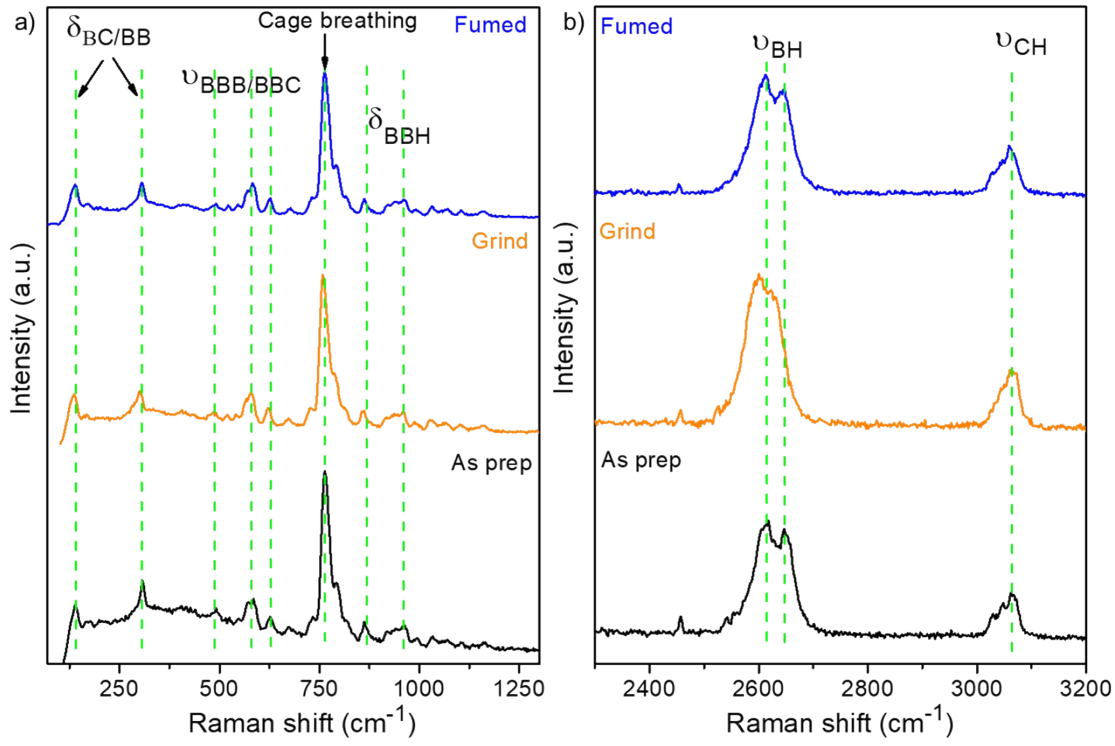

Fig. S50 Comparative Raman spectra of Cu_4@mCBT during mechanical grinding and solvent fuming experiment.

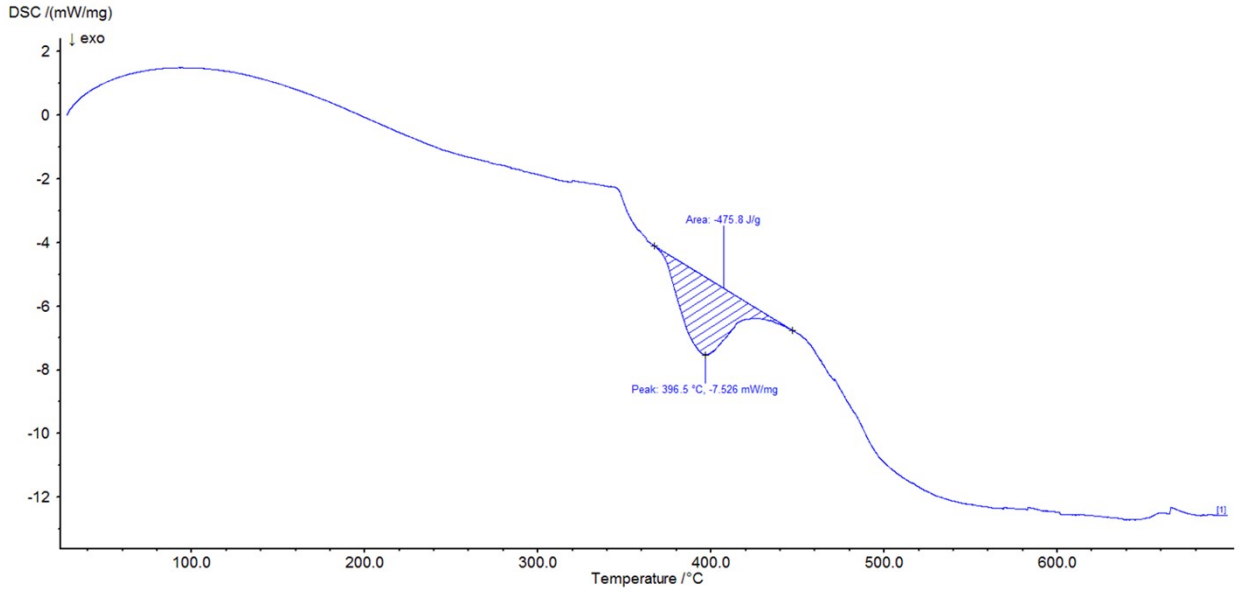

Fig. S51 Differential scanning calorimetry (DSC) data of Cu_4@oCBT microcrystals. Data was collected upon heating the sample from 25 to 750 °C. The first exothermic peak at 396.5 °C indicates superior thermal stability of the cluster.

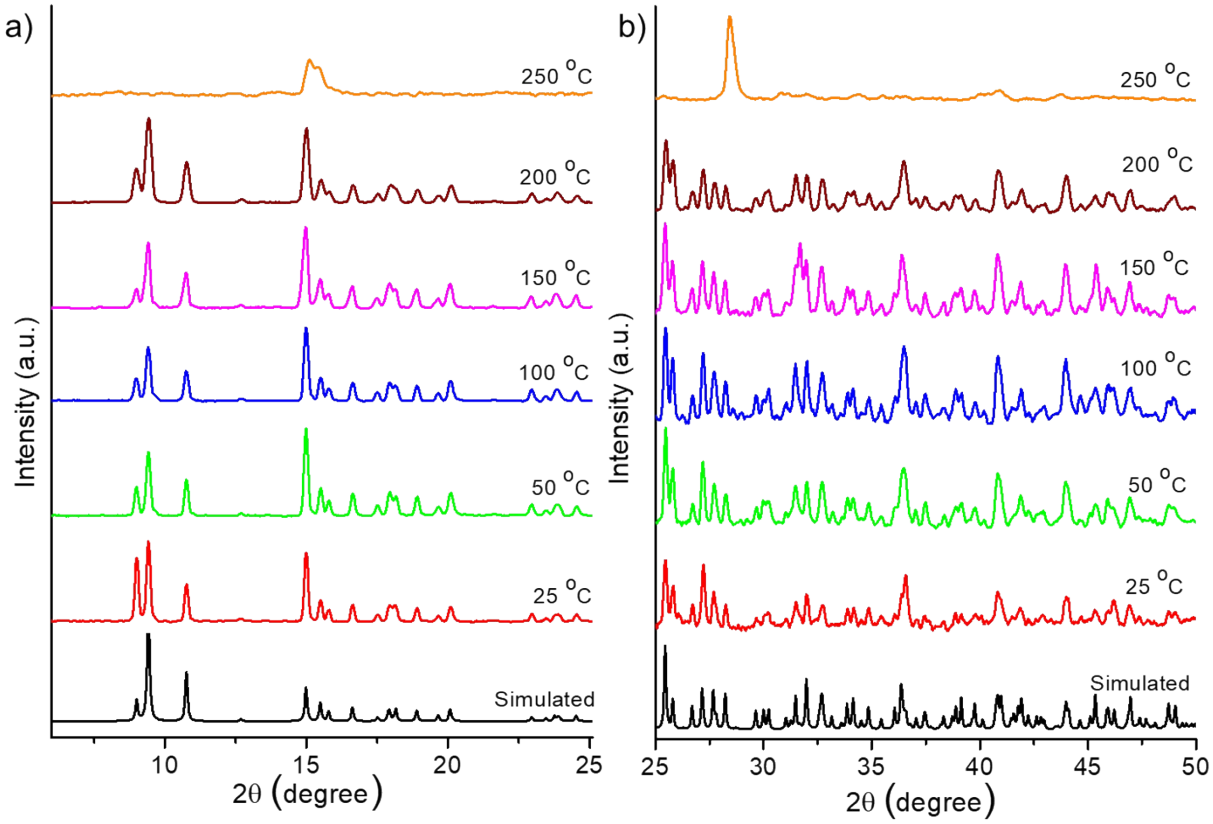

Fig. S52 Magnified PXRD pattern of Cu_4@oCBT microcrystalline powder after heating different temperatures at a) 5-25° region and b) 25° to 50° region (3 x magnification). There is no significant change of peak patterns indicating phase stability of the NC upon heating.

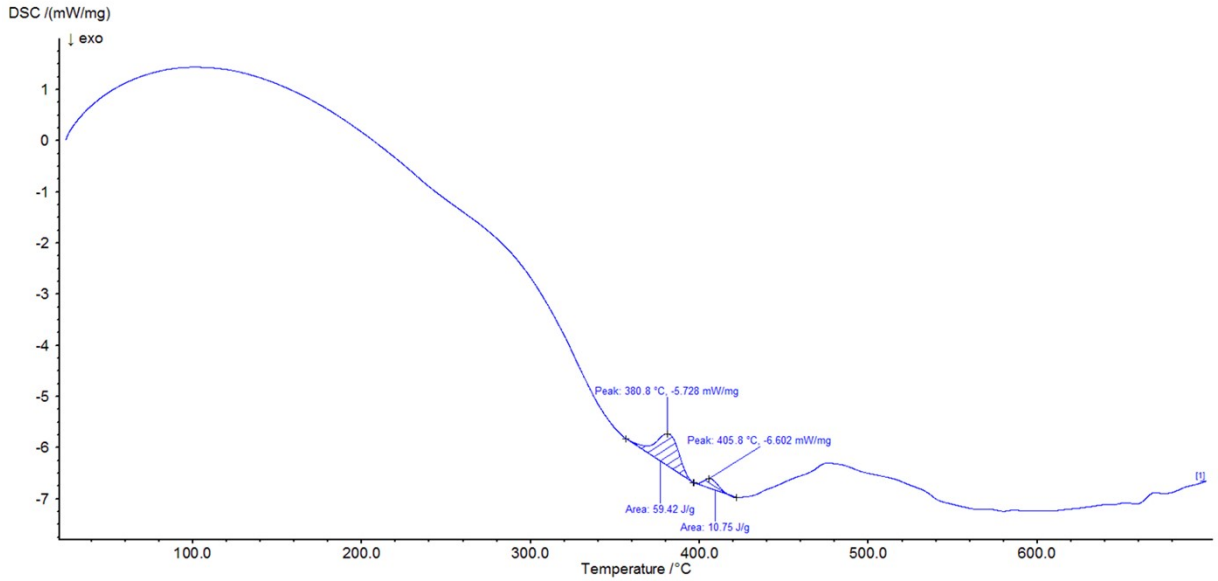

Fig. S53 Differential scanning calorimetry (DSC) data of Cu_4@mCBT microcrystals. Data was collected upon heating the sample from 25 to 750 °C.

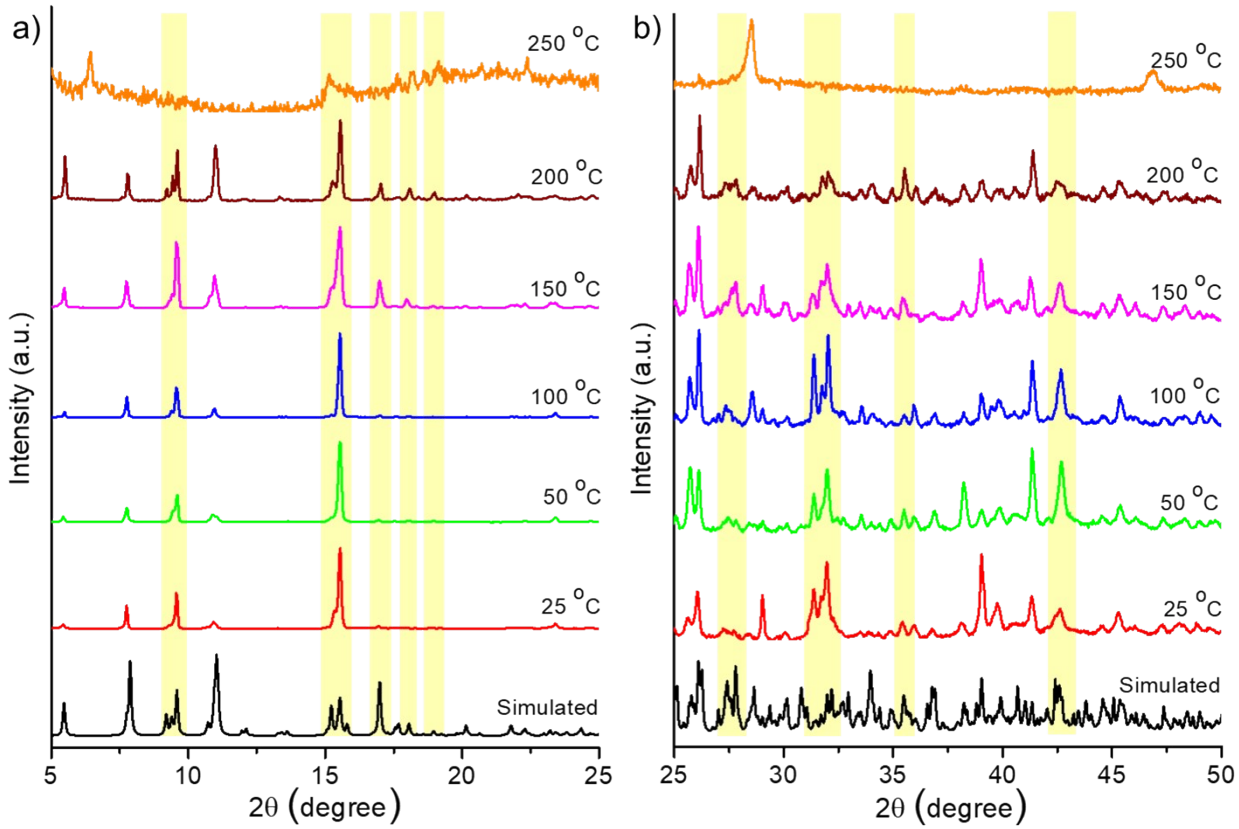

Fig. S54 Magnified PXRD pattern of microcrystalline Cu_4@mCBT after heating different temperatures at a) 5-25° region and b) 25-50° region (5x magnification). Highlighted peaks indicated the change of the diffraction patterns after 150 °C heating, which indicates temperature-induced structural distortion, which leads to the yellow emission from the sample.

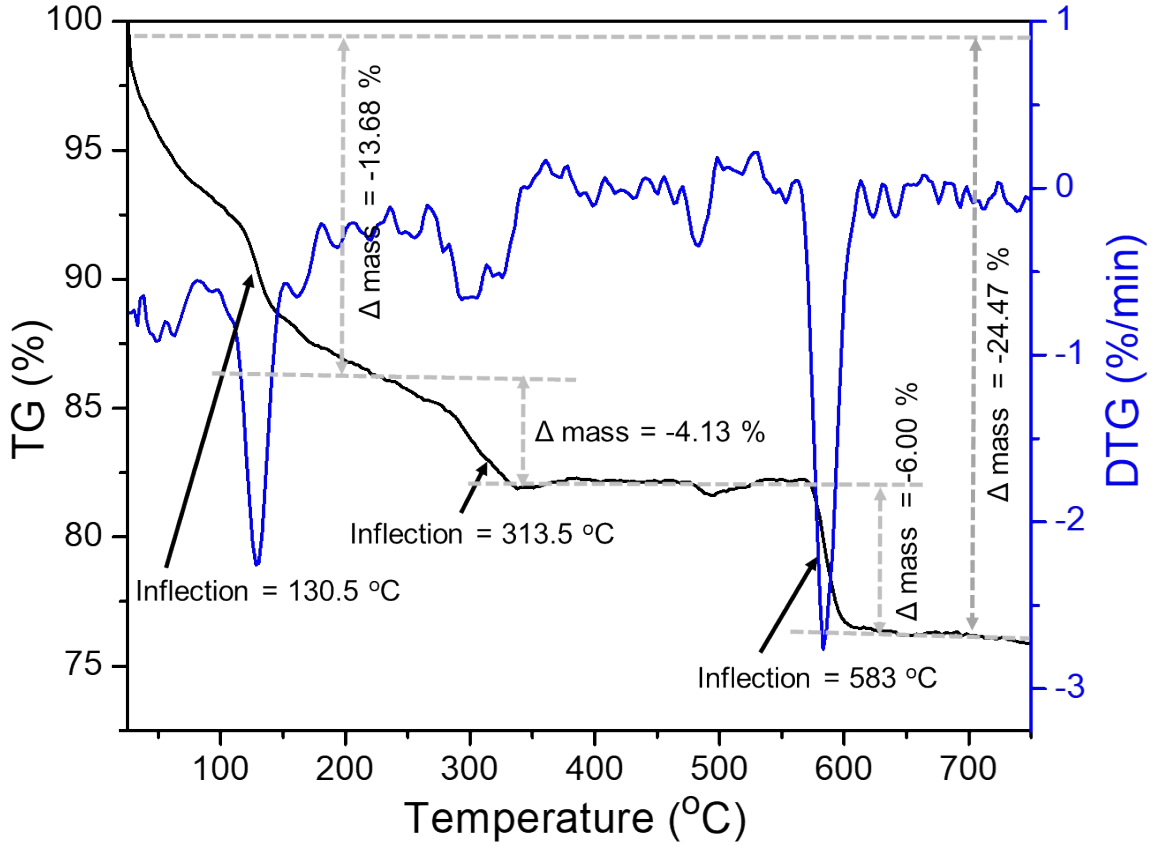

Fig. S55 TGA DTG spectra showed less thermal stability of Cu_4@ICBT compared to Cu_4@oCBT and Cu_4@mCBT derivatives.

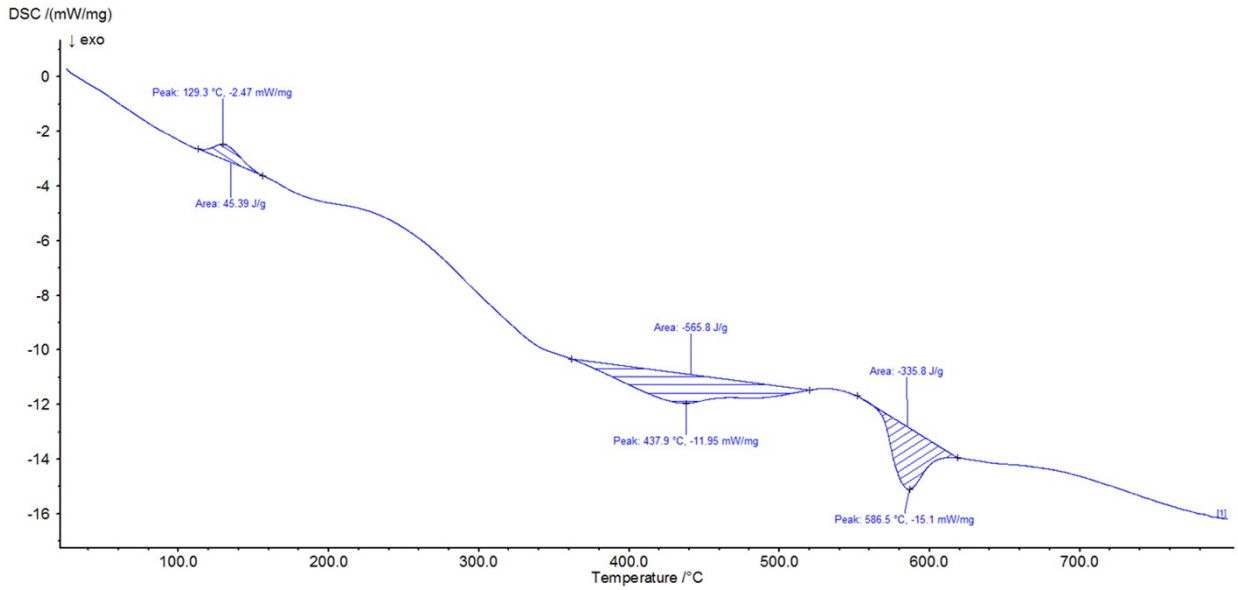

Fig. S56 Differential scanning calorimetry (DSC) data of Cu_4@ICBT microcrystals. Spectrum was collected upon heating the sample from 25 to 750 °C. The first endothermic peak at 129 °C indicates lower thermal stability than Cu_4@oCBT and Cu_4@mCBT.

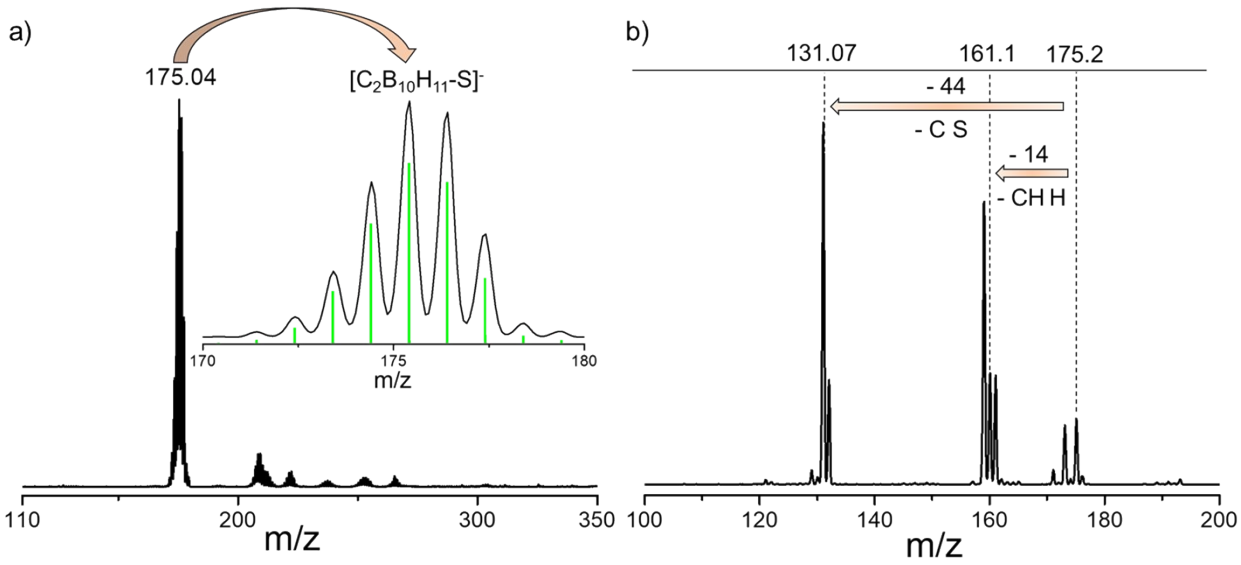

Fig. S57 a) Negative ion-mode ESI-MS spectrum of *ortho*-carborane 9-thiol ligand. Inset shows isotopic distribution of the experimental spectrum (black), centered at m/z 175.04 matches well with theoretical spectrum (green). b) The MS/MS fragmentation of the molecular ion peak shows the losses of different fragments.

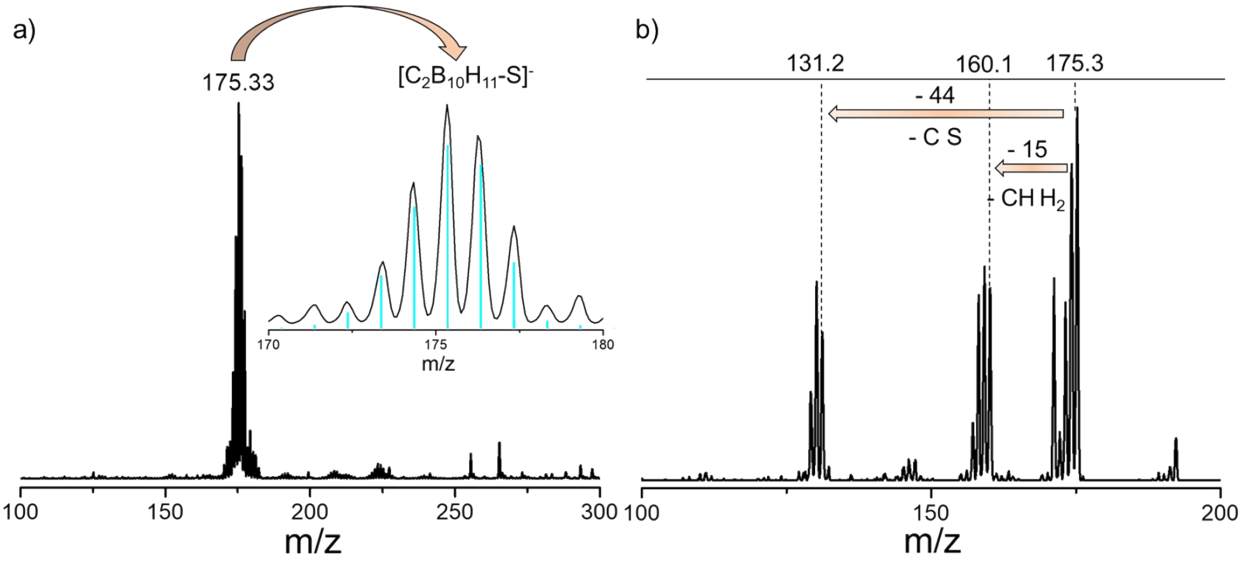

Fig. S58 a) Negative ion-mode ESI-MS spectrum of *meta*-carborane 9-thiol ligand. Inset shows isotopic distribution of the experimental spectrum (black), centered at m/z 175.33 matches well with theoretical spectrum (cyan). b) The MS/MS fragmentation of the molecular ion peak shows the losses of different fragments from the carborane framework.

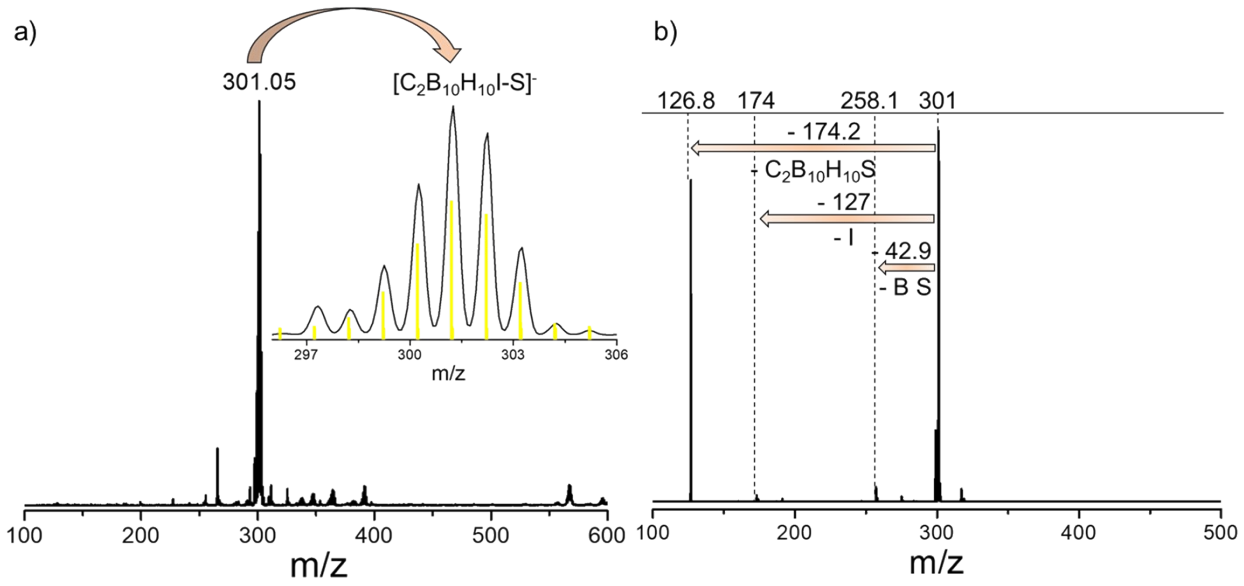

Fig. S59 a) Negative ion-mode ESI-MS spectrum of *ortho*-carborane 12-iodo 9-thiol ligand. Inset shows isotopic distribution of the experimental spectrum (black), centered at m/z 301.5 with theoretical spectrum (yellow). b) The MS/MS fragmentation of the molecular ion peak shows the losses of different fragments.

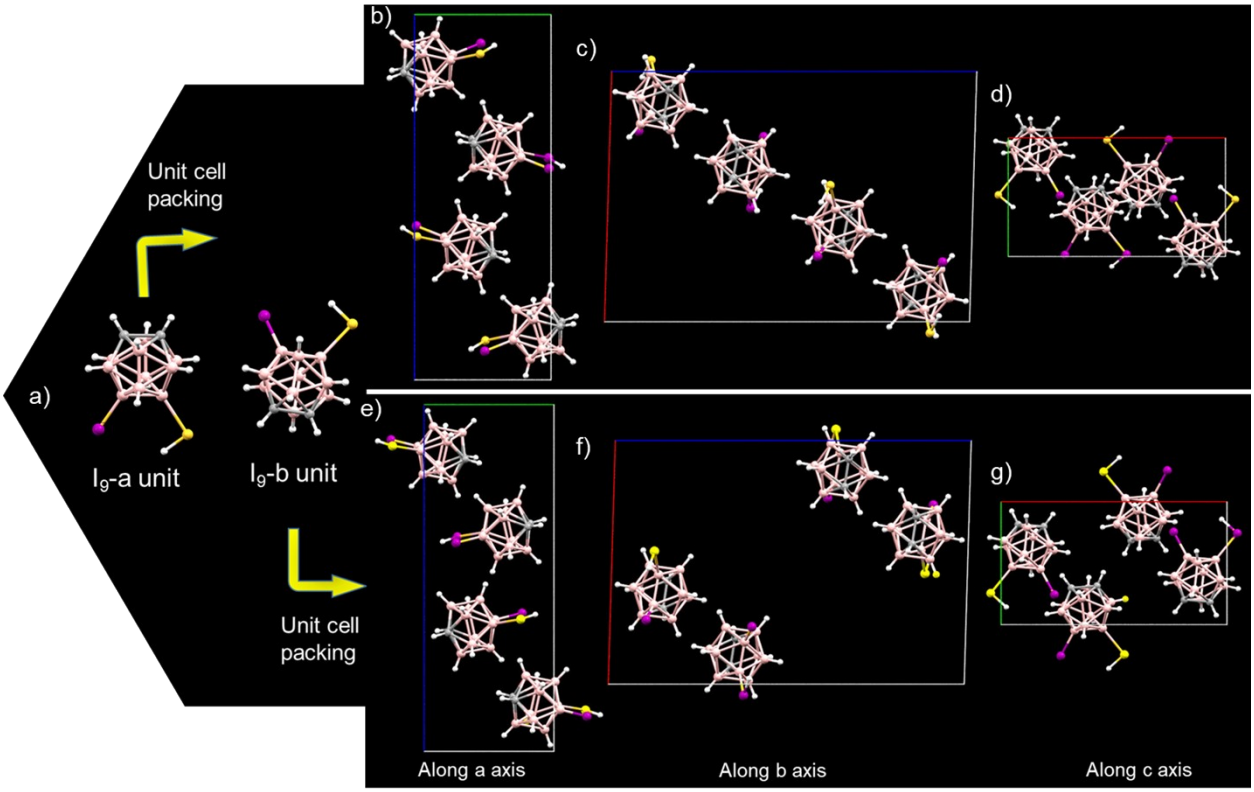

Fig. S60 a) Molecular structure of I_9 ligand with two different units. Independent unit cell molecular packing of I_9-a unit viewed from b) a, c) b and d) c crystallographic axis and I_9-b unit viewed from e) a, f) b and g) c crystallographic axis.

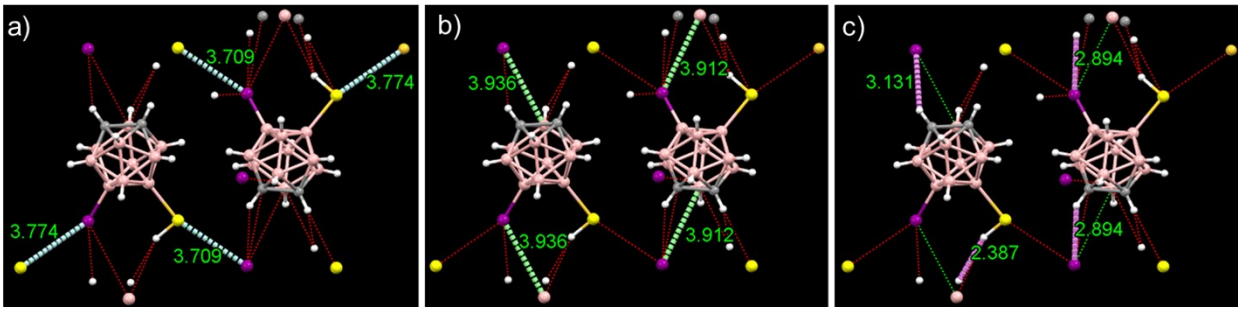

Fig. S61 Intermolecular interactions between I_9-a and I_9-b units. Three short contact interactions *i.e.*, a) S···I, b) I···B, c) CH···I or CH···S are present between these two units. Interatomic distances are marked here.

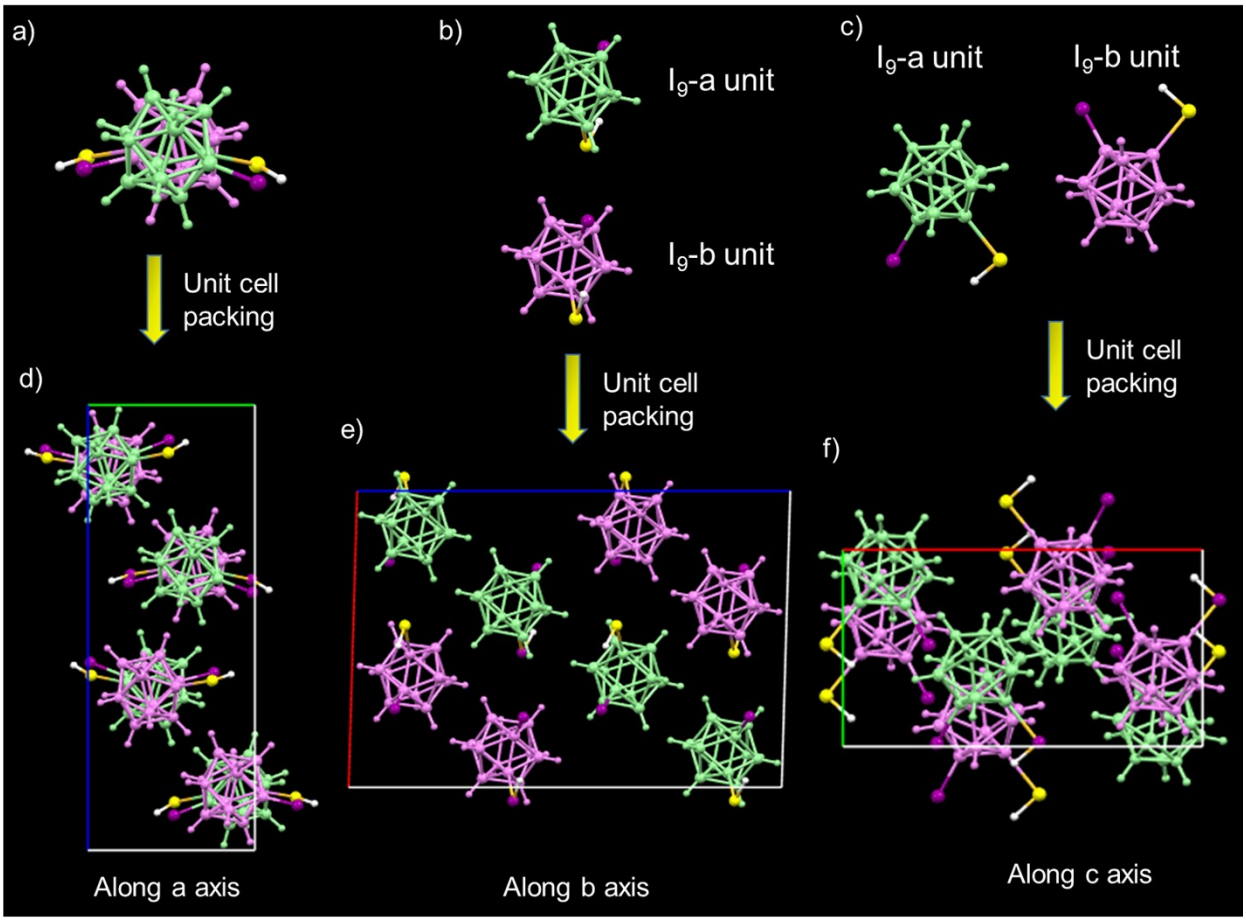

Fig. S62 Molecular structure of I_9 ligand having two different units viewed from a) a, b) b and c) c crystallographic axis. Combined unit cell molecular packing viewed from d) a, e) b and f) c crystallographic axis.

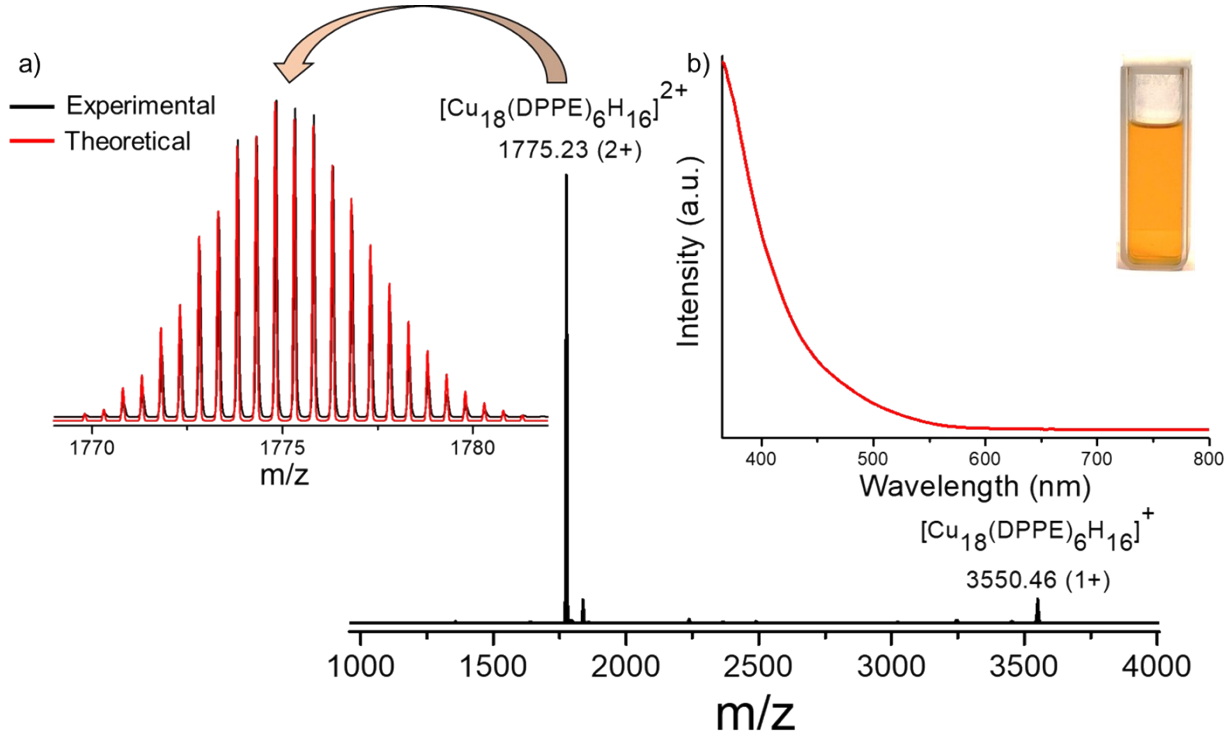

Fig. S63 Characterizations of the $[Cu_{18}(DPPE)_6H_{16}]^{2+}$. a) The full range mass spectrum of the NC in positive ion-mode indicates presence of mono and di-cationic species (inset shows exact matching of isotopic distribution of theoretical and experimental spectrum of the di-cationic species), b) UV-vis absorption spectrum of Cu_{18} (inset shows the photographic image of the orange colored cluster in DCM).

References:

(1) C. C. D. CrysAlis, Xcalibur PX Software, Oxford Diffr. Ltd., Abingdon, Engl. 2008**.**

(2) Palatinus, L.; Chapuis, G. SUPERFLIP - a computer program for the solution of crystal structures by charge flipping in arbitrary dimensions. *J. Appl. Cryst.* 2007. **40**, 786-790.

(3) Petříček, Václav; Dušek, Michal; Palatinus, Lukáš. Crystallographic Computing System JANA2006: General features. *Zeitschrift Für Krist. Mater.* 2014. **229**, 345.

(4) Mortensen, J. J.; Hansen, L. B.; Jacobsen, K. W. Real-Space Grid Implementation of the Projector Augmented Wave Method. *Phys. Rev. B - Condens. Matter Mater. Phys.* 2005, **71** (035109), 1–11.

(5) Enkovaara, J.; Rostgaard, C.; Mortensen, J. J.; Chen, J.; Dułak, M.; Ferrighi, L.; Gavnholt, J.; Glinsvad, C.; Haikola, V.; Hansen, H. A.; Kristoffersen, H. H.; Kuisma, M.; Larsen, A. H.; Lehtovaara, L.; Ljungberg, M.; Lopez-Acevedo, O.; Moses, P. G.; Ojanen, J.; Olsen, T.; Petzold, V.; Romero, N. A.; Stausholm-Møller, J.; Strange, M.; Tritsaris, G. A.; Vanin, M.; Walter, M.; Hammer, B.; Häkkinen, H.; Madsen, G. K. H.; Nieminen, R. M.; Nørskov, J. K.; Puska, M.; Rantala, T. T.; Schiøtz, J.; Thygesen, K. S.; Jacobsen, K. W. Electronic Structure Calculations with GPAW: A Real-Space Implementation of the Projector Augmented-Wave Method. *J. Phys. Condens. Matter* 2010, **22** (253202), 1–24.

(6) Adamo, C.; Barone, V. Physically Motivated Density Functionals with Improved Performances: The Modified Perdew-Burke-Ernzerhof Model. *J. Chem. Phys.* 2002, **116** (14), 5933–5940.

(7) Adamo, C.; Barone, V. Toward Reliable Density Functional Methods without Adjustable Parameters: The PBE0 Model. *J. Chem. Phys.* 1999, **110**, 6158–6170.

(8) Mennucci, B.; Tomasi, J.; Cammi, R.; Cheeseman, J. R.; Frisch, M. J.; Devlin, F. J.; Gabriel, S.; Stephens, P. J. Polarizable Continuum Model (PCM) Calculations of Solvent Effects on Optical Rotations of Chiral Molecules. *J. Phys. Chem. A* 2002, **106**, 6102–6113.

(9) Cossi, M.; Rega, N.; Scalmani, G.; Barone, V. Energies, Structures and Electronic Properties of Molecules in Solution with the C-PCM Solvation Model. *J. Comput. Chem.* 2003, **24**, 669–681.

(0) Tomasi, J.; Mennucci, B.; Cammi, R. Quantum mechanical continuum solvation models, *Chem. Rev.*, 2005, **105**, 2999-3093.

(1) Frisch, M. J.; Trucks, G. W.; Schlegel, H. B.; Scuseria, G. E.; Robb, M. A.; Cheeseman, J. R.; Scalmani, G.; Barone, V.; Petersson, G. A.; Nakatsuji, H.; Li, X.; Caricato, M.; Marenich, A. V.; Bloino, J.; Janesko, B. G.; Gomperts, R.; Mennucci, B.; Hratchian, H. P.; Ortiz, J. V.; Izmaylov, A. F.; Sonnenberg, J. L.; Williams-Young, D.; Ding, F.; Lipparini, F.; Egidi, F.; Goings, J.; Peng, B.; Petrone, A.; Henderson, T.; Ranasinghe, D.; Zakrzewski, V. G.; Gao, J.; Rega, N.; Zheng, G.; Liang, W.; Hada, M.; Ehara, M.; Toyota, K.; Fukuda, R.; Hasegawa, J.; Ishida, M.; Nakajima, T.; Honda, Y.; Kitao, O.; Nakai, H.; Vreven, T.; Throssell, K.; Montgomery, J. A. Jr.; Peralta, J. E.; Ogliaro, F.; Bearpark, M. J.; Heyd, J. J.; Brothers, E. N.; Kudin, K. N.; Staroverov, V. N.; Keith, T. A.; Kobayashi, R.; Normand, J.; Raghavachari, K.; Rendell, A. P.; Burant, J. C.; Iyengar, S. S.; Tomasi, J.; Cossi, M.; Millam, J. M.; Klene, M.; Adamo, C.; Cammi, R.; Ochterski, J. W.; Martin, R. L.; Morokuma, K.; Farkas, O.; Foresman, J. B.; Fox, D. J. Gaussian 16, Revision C.01, *Gaussian, Inc.,* Wallingford CT, 2019.

(2) Adamo, C.; Barone, V. Toward reliable density functional methods without adjustable parameters: The PBE0 model. *J. Chem. Phys.*, 1999, **110**, 6158-6169.

(3) a) Dunning,T. H. Jr.; Hay P. J. in *Modern Theoretical Chemistry*, Ed. H. F. Schaefer III, Vol. 3

(Plenum, New York, 1977), 1-28.
b) Wadt, W. R.; Hay P. J. Ab initio effective core potentials for molecular calculations – potentials for main group elements Na to Bi, *J. Chem. Phys.*, 1985, **82**, 284-298.

(14) Leites, L. A. Vibrational Spectroscopy of Carboranes and Parent Boranes and Its Capabilities in Carborane Chemistry. *Chem. Rev.* 1992, **92** (2), 279–323.